DYNAMICAL INTERACTION OF SUPERMASSIVE BLACK HOLES

WITH THE SURROUNDING STELLAR SYSTEM

Taras PANAMAREV

Printed in August 2019

Cover picture: The centre of our Milky Way Galaxy by Spitzer.

Credit: Susan Stolovy (SSC/Caltech) et al., JPL–Caltech, NASA; APOD: 10 Feb. 2007

Dissertation

submitted to the

Combined Faculties of the Natural Sciences and Mathematics

of the Ruperto-Carola-University of Heidelberg, Germany

for the degree of

Doctor of Natural Sciences

Put forward by

Taras PANAMAREV

born in: Taraz, Kazakhstan

Oral examination: 6 November 2019

DYNAMICAL INTERACTION OF SUPERMASSIVE BLACK HOLES

WITH THE SURROUNDING STELLAR SYSTEM

Referees: Prof. Dr. Andreas Quirrenbach

Prof. Dr. Björn Malte Schäfer

Abstract

We use high resolution direct N-body simulation methods to study the stellar dynamics in the Galactic centre (GC) and in active galactic nuclei (AGN). We follow the evolution of the GC from the assumed in-situ formation of the nuclear star cluster (NSC) up to 5 Gyr using one million particles taking into account single and binary stellar evolution. We investigate 3D stellar density distributions, obtain rate of tidal disruption events, rate of hypervelocity star ejections and estimate the number of extreme mass-ratio inspirals. We examine the survivability of binary stars in the NSC and discuss the contribution of binaries with compact objects in presence of pulsars and Supernovae Ia rates in the GC. We use more simplified model to study the stellar dynamics in AGN. The analysis of two simulations with 128000 particles (with and without the accretion disk (AD)) shows that the interaction of the NSC with the AD leads to formation of a stellar disc in the central part of the NSC. We derive the mass and size of the formed stellar disc and discuss possible existence of such discs in some nearby galaxies.

Zusammenfassung

Wir verwenden hochauflösende direkte N-Teilchensimulationsmethoden, um die Stellardynamik des galaktischen Zentrums (GZ) und von aktiven Galaxienkernen (AGK) zu untersuchen. Wir verfolgen die Evolution des GZ von einer angenommenen in-situ Entstehung des Kernsternhaufens (KSH) über 5 Gyr mit einer Millionen Teilchen und Einbeziehung der Einzelsternnenentwicklung und der Doppelsternenentwicklung. Wir untersuchen die dreidimensionale stellare Dichteverteilung, bestimmen die Rate der Gezeitenzerreisereignisse, die Rate der Hyperschnellläufer und schätzen die Anzahl der spiralförmingen Annäherungbahnen mit extremen Massenverhältnissen ab. Wir betrachten die Überlebensfähigkeit der Doppelsterne im KSH und diskutieren den Beitrag der Doppelsternsysteme mit kompakten Objekten in Anwesenheit von Pulsaren sowie die Rate von Supernovae des Typs Ia im GZ. Wir verwenden ein vereinfachtes Modell für die Untersuchung der Stellardynamik in AGK. Die Analyse von zwei Simulationen mit 128000 Teilchen (mit und ohne Akkretionsscheibe (AS)) zeigt, dass die Wechselwirkung des KSH mit der AS zur Entstehung einer stellaren Scheibe im Kern des KSH fährt. Wir bestimmen die Masse und die Größe der entstandenen stellaren Scheibe und diskutieren die mögliche Existenz einer solchen Scheibe in Galaxien in der Nähe der Milchstraße.

Acknowledgements

I would like to thank my supervisors, Andreas Just and Rainer Spurzem, for their guidance, advices, support and very positive supervision style. Also for giving me freedom to work and most of the time being available for answering scientific and formal questions. I want to express my gratitude to Andreas Quirrenbach, Börn Malte Schäfer for refereeing this thesis, to Tilman Plehn and Selim Jochim for being a part of my examination committee. Also, I wish to thank Matthias Bartelmann and Norbert Christlieb. I would like to express my gratitude to for joining my examination committee. I thank Peter Berczik for writing the code ϕGPU and his help with using and modifying this software. Also, thanks to Long Wang for improving the NBODY6++GPU, after that it became possible to simulate a nuclear star cluster around a massive black hole with million particles using a direct summation approach. I want to thank Fabian Klein for taking care of our computer cluster at ARI. I express my gratitude to Christian Fendt for coordinating the International Max-Planck Research School (IMPRS), providing funds for visiting conferences and helping with solving bureaucratic issues.

I want to say special thanks to my wife Kristina for her support and encouragement. I want to thank my friends and colleagues for their help and support. Thanks to Fabian Klein for helping with translations to German, thanks to Bekdaulet Shukirgaliyev, my collegue from Kazakhstan, to my office mates Reza Moetazedian, Matteo Mazzarini, Thomas Noel and Branislav Avramov.

This work was funded by IMPRS as a stipend for 3 years and extended for another 6 months by Max-Planck Institute for Astrophysics (MPIA). I would also like to acknowledge financial support from the Heidelberg Graduate School of Fundamental Physics and the IMPRS which allowed me to participate in several interesting summer schools and useful workshops. I gratefully acknowledge the computing time granted by the John von Neumann Institute for Computing (NIC) on the supercomputers JURECA and JUWELS at Jülich Supercomputing Centre (JSC) through grants HHD28 and HHD32.

Contents

List of Figures

List of Tables

To Kristina

Part I

INTRODUCTION

Chapter 1

Supermassive black holes

1.1 Quasars

In early sixties of the 20th century astronomers detected high-luminosity compact quasi-stellar objects (QSOs; also called quasars) that located in the centres of their host galaxies and had been found to outshine them (Schmidt, 1963). Yakov Zeldovich and Edwin Salpeter proposed that the accretion of matter onto the central supermassive black holes (SMBHs) can generate the required high luminosities (Salpeter, 1964; Zel'dovich, 1964). At that time black holes were too exotic objects and existed only in theory. But since then evidence for existence of SMBHs in centres of galaxies has been accumulated (Ferrarese et al., 2006; Nayakshin, Power, and King, 2012). Now, we know that most if not all galaxies harbour SMBHs in their centres.

Quasars are mostly found in the early universe and their activity peaks at a redshift $z = 2$ meaning that the SMBHs were already as massive as $\geq 10^8 M_\odot$. It is still debated in the literature how exactly the central black holes reach such extreme masses. While quasars are the most luminous objects known in the universe, there are other types of active galactic nuclei (AGN) such as Seyfert galaxies, blazars and radio galaxies. All these objects are unified under the assumption of being the same type of astrophysical object observed from different angles (Antonucci, 1993; Urry and Padovani, 1995) however this simple unification scheme is criticised (e.g. Netzer, 2015, for a review). As it was already mentioned, each type of AGN features very high luminosity. For example, the total bolometric luminosity of some bright quasars may reach $L = 10^{48}$ erg s^{-1} exceeding that of the host galaxy by 3–4 orders of magnitude.

As gas in AGN infalls from large scales it settles into a disc-like structure initially losing energy, that is converted to the radiation, and transporting angular momentum outwards. At some point, the outward radiation pressure balances the inward gravitational pull and limits the luminosity. This is the so-called Eddington limit and it can be written as:

$$L_{\rm Edd} = \frac{4\pi G M m_p c}{\sigma_T} = 1.25 \times 10^{38} \frac{M}{M_\odot} {\rm erg\,s^{-1}}, \tag{1.1}$$

where M is the mass of the object, $M_\odot$ is the solar mass, m_p is the mass of the proton, σ_T is the Thompson cross-section for electron scattering, G and c are the gravitational constant and speed of light respectively. In other words, in order to produce the luminosity $L = 10^{48}$ erg s^{-1} by the accretion of gas, one needs the SMBH of mass $\simeq 10^{10} M_\odot$. But a large mass by itself does not proof the object is a black hole, one also needs to know the size. For a black hole the region in space associated with it should not be much larger than the hole's gravitational radius $R_g = GM/c^2$. The first indication of a quasar size comes from the short-time variations of their **brightness**. Since the large-amplitude variability occurs on a time scale of days and the size of the object can not be larger than its light crossing time, one can conclude that the quasars are no more than a light-day across. In other words, the size of a quasar must be $< 100R_g$, but now there are much tighter constrains on sizes of quasars (e.g. Narayan and McClintock, 2013).

In some cases, interferometric methods allow to measure the line of sight velocities of the orbiting gas in the accretion disc. This is the case, for example, in the nucleus of galaxy M106 where the measured velocities follow a Keplerian profile and require a central mass of $4.0 \times 10^7 M_\odot$ (Miyoshi et al., 1995; Greenhill et al., 1995; Humphreys et al., 2013). The Hubble Space Telescope and some ground based telescopes equipped by the adaptive optic technique can spatially resolve central regions of nearby quiescent galaxies. This allows to measure the stellar velocity dispersion in the galactic core, deduce presence of a SMBH in the centre and determine its mass (see for a detailed review Kormendy and Richstone, 1995; Kormendy and Bender, 2009).

1.2 Supermassive black hole in the Galactic centre

The centre of our own galaxy Milky Way (MW) is ~ 100 times closer than that of the Andromeda (the nearest to us spiral galaxy). Due to its proximity, we can monitor individual stars in the Galactic centre (GC). These observations that are being carried out for more than 25 years (Ghez et al., 2005; Gillessen et al., 2009; Gillessen et al., 2017) revealed the presence of a SMBH with mass $M_{\mathrm{SMBH}} = 4.3 \times 10^6$ $\mathrm{M}_\odot$. The features of stellar orbital motion represent the strongest evidence for the presence of the SMBH in the Galaxy centre so far (see for instance Ghez et al. 2000; Eckart et al. 2017 for a review). The central black hole coexists with dense nuclear star cluster (NSC) mostly comprised of old stars (see Genzel, Eisenhauer, and Gillessen, 2010, for a review). Therefore, the Galactic Centre can be schematised as a multi-facet system, comprised of a central SMBH with mass $M_{\mathrm{SMBH}} = 4.3 \times 10^6$ $\mathrm{M}_\odot$ and a young population of massive stars (the S-stars and the nuclear disc) surrounded by an old NSC with mass $M_{\mathrm{NSC}} \simeq 2.5 \times 10^7 M_\odot$ (Schödel et al., 2014). The inner part of the NSC features distinct dynamical components such as the S-star cluster and the disc of young massive stars.

1.3 Introduction to stellar dynamics in galactic nuclei

The SMBH dominates stellar dynamics within a typical radius, called influence radius r_{inf}, which encompasses the region where the SMBH potential equals the overall gravitational field of NSC stars (see reviews by Alexander 2005; Alexander 2017). As a result of orbital evolution, spatial distribution of stars within r_{inf} is expected to evolve toward a cusp distribution, being described by a power-law $\rho(r) \propto r^{-\gamma}$. In the case of a single mass component, Bahcall and Wolf, 1976 showed that over the nucleus relaxation time, the γ value approaches a limiting value $\gamma_{\mathrm{BW}} \simeq -1.75$. Early observations of the GC did not find good matching with the theory, as the spatial distribution of old stars seem to be flat, or even decreasing, in the inner 0.1 pc (e.g. Buchholz, Schödel, and Eckart, 2009). However, recent studies supported by both observations and numerical modelling alleviated the discrepancy (Gallego-Cano et al., 2018; Schödel et al., 2018; Baumgardt, Amaro-Seoane, and Schödel, 2018).

If a star reaches a region where the SMBH tidal forces exceed its self gravity, it can undergo tidal disruption (Hills, 1975; Frank and Rees, 1976). Such process, called tidal disruption event, can be observed via emission of the stellar debris, which gets heated while falling toward the event horizon. The classical solution of the mass fallback rate follows a power-law decay $\dot{M} \sim t^{-5/3}$ (Rees, 1988; Phinney, 1989). More than 20 tidal disruption events (TDEs) have been observed in other galaxies (Komossa, 2015) implying a rate of $\sim 10^{-5}\mathrm{yr}^{-1}\mathrm{gal}^{-1}$ (Stone and Metzger, 2016). The proximity of the TDEs to the event horizon of the SMBHs allows to test general relativity in the strong gravity regime.

In the case of compact stellar remnants, such as white dwarfs (WDs), neutron stars (NSs) and black holes (BHs), the accretion onto the SMBH will radiate the binding energy in form of low-frequency gravitational waves. As the compact stellar object approaches the last stable orbit, the emission of gravitational radiation becomes more efficient and it can be detected by space-borne interferometers like LISA (Babak et al., 2017). The inspiraling objects can make $\sim 10^3 - 10^5$ orbital revolutions before being swallowed by the SMBH. The analysis of such a signal will allow to obtain information on the space-time geometry and to measure the redshifted mass and spin of the SMBH with high accuracy (Amaro-Seoane et al., 2007; Amaro-Seoane et al., 2015).

The SMBH plays an important role also in shaping the evolution of binary stars affecting the mechanisms that regulate their formation and disruption. When a binary star approaches the SMBH it can be disrupted (Hills, 1988). A possible consequence of such interaction is that one component is captured by the SMBH and the second one is kicked out with a high velocity, up to several thousand $\mathrm{km\,s^{-1}}$. Therefore, unveiling the origin of hypervelocity stars can provide useful information on the existence of the Galactic SMBH. We refer to the review provided recently by Brown, 2015 for further details. In general, binaries do not dominate the energy budget of the NSC because single stars bound to the SMBH can become very energetic (Trenti et al., 2007). The diverging velocity dispersion profile with decreasing radius from the SMBH implies that a *hard* binary at outskirts of the NSC can become *soft* near the centre and be disrupted by interactions with high-velocity single stars (Hopman, 2009). Compact objects with a 'normal' companion can form X-ray binaries. Recently, a growing number of observations revealed an overabundant presence of X-ray binaries at the GC (Muno et al., 2005b; Perez et al., 2015; Mori et al., 2015; Hailey et al., 2018; Zhu, Li, and Morris, 2018), which might be connected with the GC formation history (Arca-Sedda, Kocsis, and Brandt, 2017). Binary dynamics can lead to the formation of millisecond pulsars, comprised of rapidly rotating pulsars spun up by its companion. These sources are expected to be the main reason responsible for the Gamma-ray excess observed at the GC, although other possibilities have been invoked (Daylan et al., 2016; Fermi-LAT Collaboration, 2017), possibly related to the NSC formation history (Brandt and Kocsis, 2015; Arca-Sedda, Kocsis, and Brandt, 2017; Fragione and Loeb, 2017; Abbate et al., 2018). Moreover, the possible detection of a pulsars population in the SMBH close vicinity can be crucial to probe general relativity in the strong field regime (Psaltis, Wex, and Kramer, 2016).

1.4 Introduction to the numerical simulations of galactic nuclei

As discussed above, the NSC represents a highly complex stellar system, thus a reliable modelling of such environment requires highly precise and detailed numerical simulations, which are on the other hand, extremely time-consuming. In the case of AGN, the situation is even more difficult since the NSC also interacts with the gaseous accretion disc. The fastest way of modelling star clusters with a central massive BH is to use Monte Carlo or Fokker-Planck approaches, but these methods are approximate (e.g. Spurzem, 1999). In order to achieve high accuracy, direct N-body simulations are required. Pioneering work of modelling multi-mass stellar dynamics around a massive BH (intermediate mass BH in a globular cluster) via direct N-body simulations was done by Baumgardt, Makino, and Ebisuzaki, 2004b and (for the case of galactic nuclei) by Freitag, Amaro-Seoane, and Kalogera (2006). Just et al., 2012 did one of the first studies of AGN using direct N-body, but the authors were restricted to low-particle number and a simplistic approach to model the AD. One of the latest direct N-body models of the GC was performed by Baumgardt, Amaro-Seoane, and Schödel (2018). The possibility to use more than 1 million bodies to model a galaxy centre becomes possible only in recent times (Arca-Sedda et al., 2015; Arca-Sedda and Capuzzo-Dolcetta, 2017b; Arca-Sedda and Capuzzo-Dolcetta, 2017a). However, most of the existing models in the literature did not include all the relevant features at the same time, like a sufficiently large number of bodies, stellar evolution or a proper treatment for close encounters. Recently, the first realistic star-by-star simulations were performed for globular clusters, the DRAGON simulations (Wang et al., 2016), where the authors were able to track the stellar evolution for single and binary stars. The growing number of observations of galactic centres throughout the entire electromagnetic spectrum (e.g. Fermi-LAT Collaboration, 2017; Abuter et al., 2018; Castelvecchi, 2017) and rapidly evolving computer hardware capabilities give us a great opportunity to develop a high-accuracy numerical model of a galaxy centre which will be supported by observations.

1.5 Motivation and goal of this work

The growing number of the observational campaigns designed to study the Galactic centre shows great interest of world-wide scientific community to understand physics behind the vast variety of phenomena occurring in the central parsec of our Galaxy. Space telescopes such as Fermi with its LAT (Large Area Telescope) instrument, Chandra, SWIFT and others regularly monitor the Galactic centre in the gamma and X-ray spectral bands (Degenaar et al., 2015; Ackermann et al., 2017; Corrales et al., 2017). The famous Hubble telescope makes fantastic images of the centre of the Galaxy in the optical range, the Spitzer in infrared, Planck and COBE in the microwave. The centre of the Galaxy is also the target of some ground-based observations with use of adaptive optics (Gillessen et al., 2009; Genzel, Eisenhauer, and Gillessen, 2010), for example, the Keck Observatory, located in Hawaii, the Very Large Telescope (VLT), consisting of four 8-meter telescopes on Mount Paranal in Chile. The VLT is equipped with the specialized GRAVITY instrument, that developed, mostly, for observations of galactic centres in the infrared range (Gravity Collaboration et al., 2017; Gravity Collaboration et al., 2019). While all mentioned telescopes, in addition to observing the galactic centre, also perform other observations, the Event Horizon Telescope (ETH) project is intended solely for monitoring massive black holes in the centres of Milky Way and M87. It represents an array of radio telescopes around the globe (including the South Pole telescope in Antarctica), combined into a single facility with the length of the baseline as large as the Earth's diameter. The EHT was used to produce the first-ever picture of the black hole's shadow in M87 (Event Horizon Telescope Collaboration et al., 2019a; Event Horizon Telescope Collaboration et al., 2019b).

Goal of this work is threefold. First is to examine the interaction of stars with the accretion disc in a close vicinity of a SMBH. The second is to develop modules for the state-of-the-art numerical software NBODY6++GPU (Wang et al., 2015) which will allow to simulate stellar dynamics in both quiescent and active galactic centres. And finally, use the modified NBODY6++GPU to perform modelling of the MW NSC, which will expand our understanding of the GC. This work serves as an important and necessary step in our understanding of physical and dynamical processes in galactic nuclei.

Part II

METHODS AND THEORY

Chapter 2

Stellar dynamics in galactic nuclei

Influence radius of a SMBH (r_{inf}) determines a region in space where the SMBH dominates the dynamics. We can define this quantity as the distance where the black hole's gravitational potential equals to that of the surrounding stellar system. If we approximate the stellar potential as a singular isothermal sphere, the radius of influence then equals $r_{\text{inf}} = GM_{\text{SMBH}}/\sigma^2$. Note that by isothermal we mean constant velocity dispersion[1]. In this case the total stellar mass inside r_{inf} is similar to the SMBH mass. We refer to a review by Tal Alexander (Alexander, 2017) for further details.

2.1 The Bahcall-Wolf cusp

Gravitational interactions between individual single mass stars around a SMBH drive the stellar density distribution to evolve toward a power-law cusp $\rho \propto r^{-7/4}$ (and distribution function to $f(E) \propto E^{1/4}$; Bahcall and Wolf 1976). This is the Bahcall-Wolf solution of the time-dependent Bolzmann equation, that can be derived from a qualitative argument that stars transfer orbital energy outwards (e.g. Binney and Tremaine, 2008a).

But single mass stellar populations is a rough approximation since in reality star systems feature a broad mass spectrum. Two body interactions in the SMBH potential well drive the system towards equipartition: massive stars slow down and sink inward while the light ones gain speed and migrate outward. This phenomenon, called mass segregation, modifies the Bahcall-Wolf solution. In this realistic situation each stellar type (associated with its own mass range) has its own power-law density slope. The most massive stars (usually stellar mass black holes) approach a limiting value for the power-law index of 7/4 (Bahcall and Wolf, 1977). In Chapter 5 we obtain the power-law index for stellar black holes from a direct million-body simulation which is in a very good agreement with the Bahcall-Wolf solution.

2.2 The loss-cone theory

As we already discussed in the previous section, stars in a dense stellar system often experience encounters with each other leading to exchange of energy and angular momenta. Pericentre distance for a star with semimajor axis a on a radial orbit, $e \sim 1$, with energy $E = GM_{\text{SMBH}}/2a \sim 0$ equals

$$r_p \simeq \frac{J^2}{2GM_{\text{SMBH}}}, \tag{2.1}$$

[1]In stellar dynamics we often use analogous terms from thermodynamics. For example the term "heating" means increase in velocity.

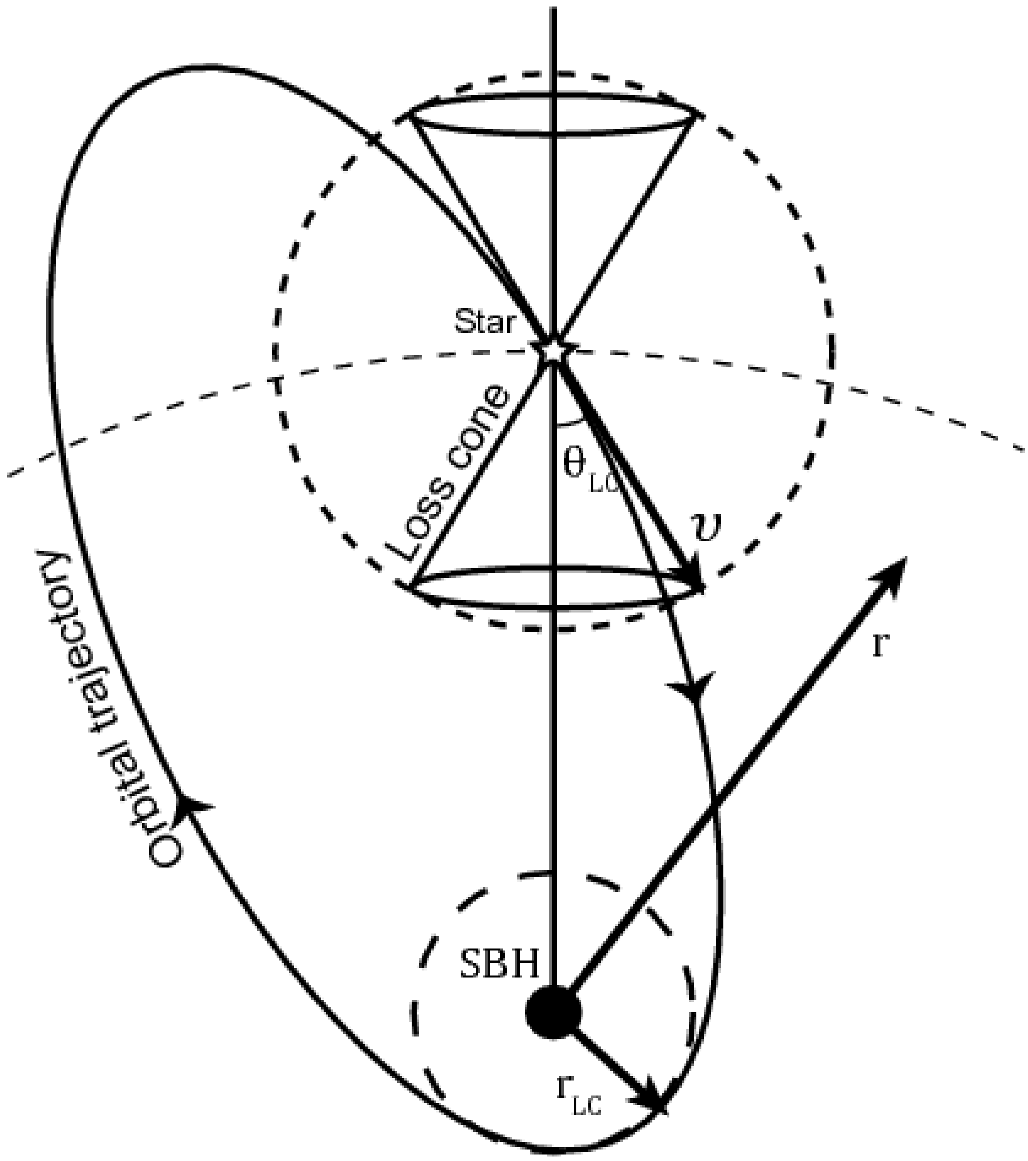

FIGURE 2.1: Visualization of the loss-cone. Source: Merritt, 2013.

where $J = \sqrt{GM_{\text{SMBH}}a(1-e^2)} = rv \sin\theta$ is the specific angular momentum. If J is small enough so that r_p locates inside stellar tidal disruption radius, we say that the star is on the loss-cone orbit. Quantitatively we can describe the loss-cone as a cone centred on star's velocity vector $\boldsymbol{v}$ and negative radius vector $-\boldsymbol{r}$ with an opening angle

$$\sin\theta \simeq \sqrt{r_p/r}. \tag{2.2}$$

This approximation follows from the angular momentum conservation: $rv\sin\theta = r_p v_p$, leading to $\sin\theta = \frac{r_p}{r}\frac{v_p}{v}$, where v_p is velocity at pericentre. Fig. 2.1 illustrates the loss-cone: here r_{lc} the loss-cone radius. The opening angle θ is usually small and points out to the small phase space volume of the loss-cone. For example, in the Galactic centre a solar type star at distance of 1 pc from the SMBH has $\theta \simeq 1.9 \times 10^{-3}$ radians. Here we assumed that the star's pericentre distance equals to the tidal disruption radius (see next section and Eq. 2.3).

By definition, the loss-cone stars are destroyed (or captured) by the SMBH during the next pericentre passage. In spherical galactic nuclei the gravitational stellar encounters are considered to be the main mechanism for the loss-cone re-population, while axisymmetric or triaxial potential produces torques which alter angular momenta and enhance the re-population rate. We refer to Merritt, 2013 for more details on the loss-cone dynamics and to (Alexander, 2017) for a discussion about the diffusion in energy and angular momenta.

2.3 Tidal disruption of stars

In the previous section we discussed the loss-cone theory: a mechanism that drives stars to be disrupted or captured by the black hole. But how to determine the disruption radius?

Let us consider a star with radius r_* and mass m_*, then we can compare the tidal force from the SMBH (difference between the gravitational force acting on the stellar surface with that on the star's centre) and the self-gravity of the star. Distance from the SMBH where the tidal force equals to the star's self-gravity is defined as the tidal disruption radius:

$$r_t = \left(\frac{M_{\mathrm{SMBH}}}{m_*}\right)^{1/3} r_* \tag{2.3}$$

The Eq. 2.3 shows that the tidal disruption radius is proportional to the stellar radius and to cubic root of the black hole mass. Thus, for SMBHs with masses $M_{\mathrm{SMBH}} > 10^8 M_\odot$ tidal disruption happens inside the hole's gravitational radius, R_g, and cannot be observed. But smaller supermassive black holes - like the one at the centre of our galaxy - disrupt stars far outside the gravitational radius. For example the tidal disruption radius of a solar type star around a SMBH of $10^6 M_\odot$ approximately equals to $r_t \sim 2.3 \times 10^{-6}$pc $\simeq 24 R_g$. The critical mass above which the star is disrupted inside the event horizon is called the Hills mass and can be expressed as:

$$M_{\mathrm{Hills}} = 1.1 \times 10^8 M_\odot \left(\frac{r_*}{R_\odot}\right)^{3/2} \left(\frac{m_*}{M_\odot}\right)^{-1/2} \tag{2.4}$$

We can measure the strength of the tidal disruption events by the value of ratio between tidal radius and pericentre distance that is called the penetration factor:

$$\beta = \frac{r_t}{r_p}. \tag{2.5}$$

The value of the penetration factor determines what part of the specific binding energy of the stellar debris $\Delta\epsilon \approx G M_{\mathrm{SMBH}} r_* / r_t^2$ is bound to the SMBH. Hayasaki et al., 2018 use orbital eccentricity and semimajor axis to distinguish between eccentric, parabolic and hyperbolic tidal disruption events. For example in the eccentric case all the material is bound to the SMBH and eventually comes back leading to possible formation of an accretion disc - thus, the classification determines the mass fallback rate of the stellar debris onto the SMBH. Note that here we restricted our discussion to the case of supermassive black holes and used basic Newtonian physics for the above calculations. Alexander (2005) gives more general classification of tidal disruption events, but also with use of the penetration factor β.

A parabolic tidal disruption flare features the mass fallback rate that decays in time as $t^{-5/3}$ (Rees, 1988; Phinney, 1989) and produces a lightcurve that is used as a template to observe the tidal disruption events. So far, more than 20 of them have been observed implying a rate of $\sim 10^{-5}\mathrm{yr}^{-1}\mathrm{gal}^{-1}$ (Komossa, 2015; Stone and Metzger, 2016). In theory, the loss-cone re-population mechanism determines the tidal disruption events rate, but the theoretical estimates are one order of magnitude higher (Magorrian et al., 1998; Wang and Merritt, 2004). This discrepancy may arise from the fact that a major contribution to the TDE rates comes from low-mass main sequence stars (see e.g. Panamarev et al. 2019) and may be difficult to observe. The disruption of red giants is also hard to observe: due to the large sizes, the mass fall-back time is longer and eventually the luminosity is lower (MacLeod, Guillochon, and Ramirez-Ruiz, 2012). We refer to Chapter 5 for a detailed analysis of the contribution from different stellar types to the tidal disruption in the Galactic centre.

As we have seen in the previous section, stars "enter" the loss-cone from radial orbits giving rise to very high eccentricities of the disrupted stars. One of the possibilities for a tidal disruption of a star on nearly circular orbit is the interaction of the star with the accretion disc. The star–disc interactions are natural for active galactic nuclei and we show in Chapter 4 (see also Just et al. 2012; Kennedy et al. 2016; Panamarev et al. 2018) that this mechanism leads to a wide range of eccentricities of disrupted stars and may even lead to formation of a central steady-state stellar disc (Panamarev et al., 2018).

2.4 Extreme mass ratio inspirals

As we have seen, accretion of stars onto SMBHs with masses $M_{\mathrm{SMBH}} < 10^8 M_\odot$ leads to the tidal disruption. But the picture changes when a compact object such as white dwarf, neutron star or stellar mass black hole approaches the SMBH (note that white dwarf may be still disrupted by an intermediate mass black hole). During the pericentre passage, these objects would radiate their binding energy producing gravitational waves (GW) and eventually merge with the SMBH in a process called extreme mass ratio inspiral (EMRI). The emission of GWs leads to orbital decay of a relatively light object around a much heavier object with the mass ratio of $\geq 10^4$. In order to detect GWs, we measure the relative change in distance (the strain $h = \Delta R/R$): as the wave propagates through space, distance between objects stretches and squeezes rhythmically at the wave's frequency. For an EMRI the strain is given by (Thorne, 1987):

$$h \simeq 9 \times 10^{-23} \frac{m_*}{10\, M_\odot} \left(\frac{M_{\mathrm{SMBH}}}{10^6\, M_\odot} \frac{f}{10^{-3}\,\mathrm{Hz}} \right)^{2/3} \left(\frac{D}{1\,\mathrm{Gpc}} \right)^{-1} \tag{2.6}$$

where D is the distance to the source, f is the GW frequency. Since EMRIs originate from the nearest vicinity of a SMBH they can be used to probe the strong gravitational field and test the general relativity.

The time left to merge estimates as (Peters 1964; we assume that EMRIs originate from parabolic orbits):

$$t_{\mathrm{GW}} \approx \frac{768}{425} \frac{5}{256} \frac{c^5}{G^3} \frac{a^4}{m_1 m_2 (m_1 + m_2)} \left(1 - e^2\right)^{7/2}, \tag{2.7}$$

where m_1 and m_2 are masses of the merging bodies, e and a are eccentricity and semimajor axis, c is the speed of light. In Ch. 5 we compare the merging time with the relaxation time and estimate the number of EMRIs originating from the Galactic centre.

A detection of an EMRI would allow to measure mass of the SMBH (at the moment of merging), its spin parameter, orbital properties of an in-spiralling body (inclination angle and eccentricity), luminosity distance (Barack and Cutler, 2004).

Planned space-borne GW interferometers like LISA and TianQuin (Luo et al., 2016b) highlight the importance of EMRI detections to get better understanding of gravitation.

2.5 Formation of Hypervelocity stars

Three body exchange of a binary star and SMBH may produce a hypervelocity star (Hills, 1988). When the binary penetrates deep into the tidal field of the SMBH, at some moment, the force exerted by the SMBH exceeds the mutual gravitational interaction of the binary components. This tidal separation results in ejection of one of the components while the second binary member becomes bound to the SMBH. The tidal separation distance is given by (Hills, 1988):

$$r_{\rm bt} = a\left(\frac{3M_{\rm SMBH}}{m_b}\right)^{1/3}, \tag{2.8}$$

where a is the binary semimajor axis, m_b is the total mass of the binary. For a system of two solar-type stars with semimajor axis of 0.1 AU and the SMBH in the Galactic centre the distance equals to about 18.5 AU. It is quite small radius, but is still larger than the tidal disruption distance for a single star.

The ejected star gains the velocity that may significantly exceed the Galactic escape speed and is given by (Brown, 2015):

$$V_{\rm ej} \simeq 1370\,{\rm km\,s^{-1}}\left(\frac{a}{0.1{\rm AU}}\right)^{-1/2}(m_b/M_\odot)^{1/3}\left(\frac{M_{\rm SMBH}}{4\times10^6 M_\odot}\right)^{1/6} \tag{2.9}$$

Fig. 2.2 helps to visualize the velocities obtained by ejected stars as function of binary separation.

Eq. 2.9 can be derived from energy conservation arguments. The orbital velocity of the centre of mass of the binary at the separation radius is $v = \sqrt{GM_{\rm SMBH}/r_{\rm bt}}$, while the relative velocity of a binary component equals to $v_b = \sqrt{Gm_b/a}$. At the moment of disruption, stars undergo change in the specific energy: $\Delta\epsilon = 1/2(v + v_b)^2 - 1/2v^2 \simeq vv_b$ (Hills, 1975; Yu and Tremaine, 2003). Then, the ejected star gets the velocity at infinity of $v = \sqrt{2vv_b}$.

2.6 Stellar and gas dynamics in AGN

An important contribution to the modern understanding of dynamic processes in AGN was made by Kazakh researchers from Fesenkov Astrophysical Institute. For example, semi-analytical models of the interaction of stars with the accretion disc were developed in Vilkoviskij and Czerny, 2002, where the authors analysed the influence of the friction forces of gas disc on the dynamics of stars near the SMBH. Further, using numerical modelling by direct integration of the N–body problem, it was shown that interaction with the gaseous disc leads to an increase in the accretion rate of stars onto the SMBH (Just et al., 2012). After that, according to the results of 39 simulations of various AGNs, the orbital parameters of accreted stars were investigated and an important result was obtained that approximately one third of the objects fall into the MBH with almost circular orbits, while being in the plane of

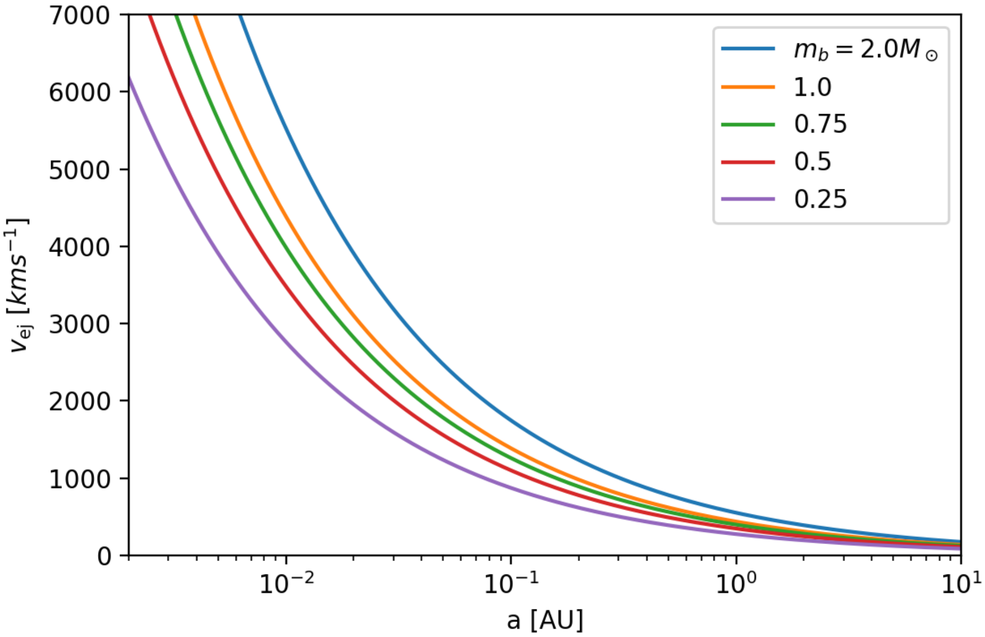

FIGURE 2.2: Ejection velocity of HVS as function of semimajor distance. Different curves represent various total masses of binaries.

the gas disc (Kennedy et al., 2016). In this study we show that interaction with the accretion disc leads to the formation of a stellar disc in the very central part of an active galactic nucleus (Ch. 4, Panamarev et al. 2018).

Chapter 3

Direct summation methods

3.1 The N-body problem

We encounter the N-body problem in many areas of astrophysics: from simulations of planetary systems and asteroids to galaxies and galaxy clusters; from systems of artificial satellites to active galactic nuclei and so on. For each of the cases there is a relative approach. Nevertheless, the equations of motion are nearly the same meaning that we can generalize the basic principles and methods of the N-body problem. In this chapter we focus mostly on collisional systems and describe methods relative to this specific case.

The stellar system is called collisional if gravitational interactions between individual stars play significant role in the overall dynamics on a time scale smaller than the age of the system. In other words, in collisional systems the relaxation time (Chandrasekhar, 1942; Spitzer, 1987) is smaller or comparable to the system's age. For instance, open and globular clusters, nuclear star clusters are collisional systems, while galaxies, galactic bulges and discs are collisionless. The motion of a test particle in a collisionless systems may be well described by the motion in a smooth potential generated by all other stars. On the other hand, in collisional systems the pairwise interactions mainly determine the trajectory or at least can not be neglected. The more frequently gravitational collisions[1] occur the denser the system is considered to be. Typical relaxation times for open and globular clusters are in order of $10 - 100$ Myr and ≤ 1 Gyr respectively.

The equation of motion determines gravitational interactions between stars:

$$\ddot{\mathbf{r}}_i = -G \sum_{i \neq j}^{N} \frac{m_j(\mathbf{r}_i - \mathbf{r}_j)}{|\mathbf{r}_i - \mathbf{r}_j|^3}, \tag{3.1}$$

where m_j is the mass of j-th particle, $\mathbf{r_i}$ and $\mathbf{r_j}$ are the radius vectors of particles i and j. We can also express this equation as a system of $6N$ first order differential equations in terms of positions and velocities of the particles i and j. The Eq. 3.1 describes behaviour of isolated system of N particles, but we can add external potential as an additional term to account for interaction with a massive black hole, tidal field of a galaxy (in case of globular clusters) and so on.

In general case, the N-body problem has no analytic solution, but if we know initial conditions, then Eq. 3.1 becomes a Cauchy problem and is subject to numerical integration. The *direct* N-body methods rely on the numerical integration of the equation of motion: they are the most accurate, but at the same time, the most time-consuming. In this chapter we summarize techniques to reduce the computational costs while preserving the high accuracy.

[1] By collisions we mean close gravitational encounters, NOT physical collisions

Sebastian von Hörner obtained the first numerical solutions for stellar systems with $N = 4, 8, 12$ and 16 (von Hoerner, 1960) and later with 25 components (von Hoerner, 1963) on a computer at Astronomisches Rechen-Institut (Institute for Computational Astronomy) in Heidelberg, Germany. Later on, Sverre Aarseth made major contribution to advance the direct N-body methods: he developed a family of computer codes starting from NBODY1 in 1961 (Aarseth, 1963) to NBODY6 (Aarseth, 2003) nowadays. When NBODY6 was widely used, R. Spurzem (Spurzem et al., 2008) developed a parallel version NBODY6++ to use on parallel supercomputers. Later on, when scientists realized the advantage of graphic processing units (GPUs) to deal with the N-body problem, Nitadori and Aarseth (2012) extended NBODY6 to NBODY6-GPU to accelerate the gravitational force calculations using GPUs. As a result, Sippel and Hurley (2013) performed globular clusters simulations with more than 250 000 particles. The main limitation of NBODY6-GPU was that it could be operated only on a single-node workstation, but few years later it was extended to a massively parallel code NBODY6++GPU (Wang et al., 2015). This development resulted in four realistic star-by-star simulations of globular clusters using one million particles (Wang et al., 2016). As one of the goals of this work, Panamarev et al. (2019) added interaction with supermassive black hole to NBODY6++GPU and performed a million-body simulation of the Milky Way nuclear star cluster (see Chapters 5 and 6).

3.2 The Hermite integration method

Numerical integration requires initial conditions. In our case these are position $\mathbf{r}_0$ and velocity $\mathbf{v}_0$ at an initial value of time t_0. We are solving the Eq.3.1 and thus the motion of a particle i is determined by its acceleration $\mathbf{a}_{0,i}$ caused by total gravitational pull by all other particles:

$$\mathbf{a}_{0,i} = -\sum_{i \neq j} G m_j \frac{\mathbf{R}}{R^3}, \tag{3.2}$$

and its time derivative:

$$\dot{\mathbf{a}}_{0,i} = -\sum_{i \neq j} G m_j \left[\frac{\mathbf{V}}{R^3} + \frac{3\mathbf{R}(\mathbf{V} \cdot \mathbf{R})}{R^5} \right], \tag{3.3}$$

where G is the gravitational constant; $\mathbf{R} = \mathbf{r}_{0,i} - \mathbf{r}_{0,j}$ is the relative coordinate to the particle j; $R = |\mathbf{r}_{0,i} - \mathbf{r}_{0,j}|$ the distance; and $\mathbf{V} = \mathbf{v}_{0,i} - \mathbf{v}_{0,j}$ the relative velocity.

Now, as the first step, we perform Taylor expansion for $\mathbf{r}$ and $\mathbf{v}$ in order to find the solution in form of a polynomial approximation:

$$\mathbf{r}_{p,i}(t) = \mathbf{r}_0 + \mathbf{v}_0(t - t_0) + \mathbf{a}_{0,i}\frac{(t-t_0)^2}{2} + \dot{\mathbf{a}}_{0,i}\frac{(t-t_0)^3}{6}, \tag{3.4}$$

$$\mathbf{v}_{p,i}(t) = \mathbf{v}_0 + \mathbf{a}_{0,i}(t - t_0) + \dot{\mathbf{a}}_{0,i}\frac{(t-t_0)^2}{2}. \tag{3.5}$$

In the Hermite scheme this first step is called prediction: we predict values for position and velocity (the subscript p means prediction). But these approximations do not satisfy our requirements of the desired error tolerance. To improve the predicted values we perform another Taylor expansion, but now for the acceleration and its time derivative:

$$\mathbf{a}_i(t) = \mathbf{a}_{0,i} + \dot{\mathbf{a}}_{0,i} \cdot (t - t_0) + \frac{1}{2}\mathbf{a}^{(2)}_{0,i} \cdot (t - t_0)^2 + \frac{1}{6}\mathbf{a}^{(3)}_{0,i} \cdot (t - t_0)^3, \tag{3.6}$$

$$\dot{\mathbf{a}}_i(t) = \dot{\mathbf{a}}_{0,i} + \mathbf{a}^{(2)}_{0,i} \cdot (t - t_0) + \frac{1}{2}\mathbf{a}^{(3)}_{0,i} \cdot (t - t_0)^2. \tag{3.7}$$

The values of $\mathbf{a}_{0,i}$ and $\dot{\mathbf{a}}_{0,i}$ are given by Eq. 3.2 and Eq. 3.3. The straightforward way to find $\mathbf{a}^{(2)}_{0,i}$ and $\mathbf{a}^{(3)}_{0,i}$ is to differentiate the Eq. 3.3 two times, but this procedure is computationally 'expensive'. Here comes the idea behind the Hermite method.

We calculate acceleration $\mathbf{a}_{p,i}$ and its first derivative $\dot{\mathbf{a}}_{p,i}$ for the predicted values of position and velocity using Eq. 3.2 and Eq. 3.3, and plug-in them as $\mathbf{a}_i(t)$ and $\dot{\mathbf{a}}_i(t)$ in equations 3.6 and 3.7 respectively. Now we have a system of two algebraic equations with two unknowns $\mathbf{a}^{(2)}_{0,i}$ and $\mathbf{a}^{(3)}_{0,i}$. A straightforward solution yields:

$$\mathbf{a}^{(3)}_{0,i} = 12\frac{\mathbf{a}_{0,i} - \mathbf{a}_{p,i}}{(t - t_0)^3} + 6\frac{\dot{\mathbf{a}}_{0,i} + \dot{\mathbf{a}}_{p,i}}{(t - t_0)^2}. \tag{3.8}$$

and

$$\mathbf{a}^{(2)}_{0,i} = -6\frac{\mathbf{a}_{0,i} - \mathbf{a}_{p,i}}{(t - t_0)^2} - 2\frac{2\dot{\mathbf{a}}_{0,i} + \dot{\mathbf{a}}_{p,i}}{t - t_0}. \tag{3.9}$$

The trick here was to avoid direct computation of higher order terms by expressing them as a function of lower-order terms. Now, we can extend the Taylor expansion for $\mathbf{r}_i$ and $\mathbf{v}_i$ to higher orders:

$$\mathbf{r}_{1,i}(t) = \mathbf{r}_{p,i}(t) + \mathbf{a}^{(2)}_{0,i}\frac{(t - t_0)^4}{24} + \mathbf{a}^{(3)}_{0,i}\frac{(t - t_0)^5}{120}, \tag{3.10}$$

$$\mathbf{v}_{1,i}(t) = \mathbf{v}_{p,i}(t) + \mathbf{a}^{(2)}_{0,i}\frac{(t - t_0)^3}{6} + \mathbf{a}^{(3)}_{0,i}\frac{(t - t_0)^4}{24}. \tag{3.11}$$

This is the second step of the Hermite scheme and is called 'correction' since it corrects position $\mathbf{r}_{1,i}$ and velocity $\mathbf{v}_{1,i}$ of the particle i at the computation time t_1.

We describe the fourth order Hermite method, but it can be extended to higher orders by the same principle. NBODY6++GPU and PhiGPU (the two software packages used in this thesis) feature 4-th order integrator, while some other direct N-body codes like HiGPUs use 6-th order Hermite integrator (Capuzzo-Dolcetta, Spera, and Punzo, 2013). For analysis and discussion of higher order integrators see Nitadori and Makino, 2008.

3.3 Individual and block time steps

One of the most important issues in the N-body problem is the choice of the timestep (the value $t - t_0$ from the previous subsection). This is of high importance because stellar systems feature huge range of temporal scales: hours in the case of orbiting double degenerate pairs (e.g. Parsons et al., 2011), tens of years in the case of single stars moving very close to supermassive black holes (Schödel et al., 2002), millions of years - lifetime of very massive stars, billions of years - relaxation time of globular clusters (e.g. Binney and Tremaine, 2008b). Even if we consider only dynamics of single stars the timespan of stellar motions will be tremendous. For this reason, if we choose the smallest timestep determined by the fastest particle in the centre of the system, then we have to perform unnecessary computations for every star at the outskirts using the smallest timestep.

A basic idea to overcome this problem was introduced by S. J. Aarseth (Aarseth, 1963). The essence is to introduce individual timestep $\Delta t = t_1 - t_0$ for each particle. Let us introduce two primary coordinate and position vectors $\mathbf{r}_j(t_j)$, $\mathbf{v}_j(t_j)$ and two secondary $\tilde{\mathbf{r}}_j(t)$ and $\tilde{\mathbf{v}}_j(t)$; where t_j is individual time for each particle, t - current global time for all particles. Further on, we introduce a list of M bodies that satisfy the condition:

$$t_j + \Delta t_j < t_M, \tag{3.12}$$

where t_M is a critical time and Δt_j is a current value of the individual timestep for the particle j.

Initially (at $t = 0$), we assume $t_M == \Delta t_M$, where Δt_M is chosen so that the list M would contain $\sim \sqrt{N}$ bodies. The list is updated when the global current time t exceeds t_M and the new members are selected from the all N bodies.

The main integration cycle begins with searching a particle with minimal value of $t_j + \Delta t_j$. If we assign this particle with index i, then the current value of global time is:

$$t = t_i + \Delta t_i \tag{3.13}$$

Then we can predict its position and velocity using the first step of Hermite scheme (see previous subsection). When the new value of time is determined, we initialize main coordinates of the particle i:

$$\mathbf{r}_i(t_i) = \tilde{\mathbf{r}}_i(t_i) \tag{3.14}$$

The integration cycle ends with computing new values for individual timesteps.

We determine the timestep using the formula empirically derived by S. Aarseth (Aarseth, 1985):

$$\Delta t_i = \sqrt{\eta \frac{|\mathbf{a}_{1,i}||\mathbf{a}_{1,i}^{(2)}| + |\dot{\mathbf{a}}_{1,i}|^2}{|\dot{\mathbf{a}}_{1,i}||\mathbf{a}_{1,i}^{(3)}| + |\mathbf{a}_{1,i}^{(2)}|^2}}, \tag{3.15}$$

where η is a dimensionless accuracy parameter which controls the error. In the simulations related to this thesis, we used the value of $\eta = 0.02$.

The individual timestep scheme was used in early realization of N-body codes, but starting from NBODY6 the developers improved it to hierarchical block timestep scheme.

Figure 3.1 gives a graphical illustration of the block time steps scheme. The values for the timesteps are quantized as 2^{-n} with $n = 2, 3, ...$ So, positions and velocities for particle i with the smallest time step (see Fig. 3.1) are determined at each timestep, while the timestep for particle k is two times bigger and its phase space coordinates are determined only at time intervals denoted by dots, at other time intervals the coordinates are predicted. The example of particles k and l illustrates that the step size may be changed at the end of the integration cycle. The scheme is called hierarchical because it requires the steps to be proportional (in our case it is a power of 2) to guarantee that all particles are synchronized at some timestep.

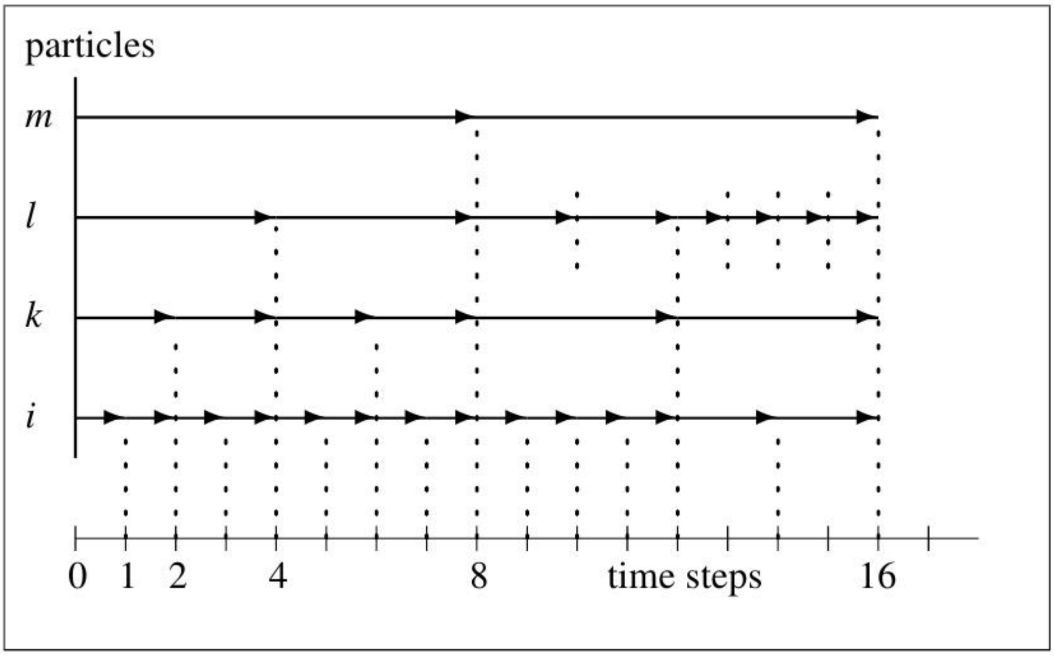

FIGURE 3.1: Block time steps example for four particles. Credit: Khalisi, Wang, and Spurzem, 2014

3.4 The Neighbour scheme

One more way to reduce the computational time is to split the total force acting on a particle (3.6) into two different components

$$\mathbf{a}_i = \mathbf{a}_{i,\mathrm{irr}} + \mathbf{a}_{i,\mathrm{reg}}, \tag{3.16}$$

where $\mathbf{a}_{i,\mathrm{irr}}$ is irregular part - the contribution from nearest particles (called neighbours) and $\mathbf{a}_{i,\mathrm{reg}}$ - is regular part - the overall contribution from remaining bodies. The idea is that we replace the full summation in Eq. 3.2 by the sum over L nearest particles ($L \ll N$) and predict the contribution from distant ones. This is the so–called Neighbour scheme suggested by Ahmad and Cohen, 1973 and often referred as Ahmad-Cohen method.

The implementation of the method is as follows. For each particle we create a list of L neighbours that are located inside the sphere of radius R_s centred at the particle. The neighbours exert the strongest contribution to the particle's motion. We also have to keep track of the buffer zone from R_s to $2^{1/3}R_s$ in order to make sure that we do not miss the particles that approach neighbour sphere with high velocities. Fig. 3.2 shows visual representation of the neighbour sphere.

In NBODY6 the size of a neighbour sphere can be computed from the local density contrast (Aarseth, 2003):

$$C = \frac{2L1}{N}\left(\frac{R_{1/2}}{R_s}\right)^3, \tag{3.17}$$

where L_1 number of particles inside R_s, $R_{1/2}$ size of the sphere containing half of the all particles centred at the centre of mass of the whole system of N bodies. In other words, C is the ratio of mean density of the neighbour sphere to the mean density of the sphere containing half of the total system.

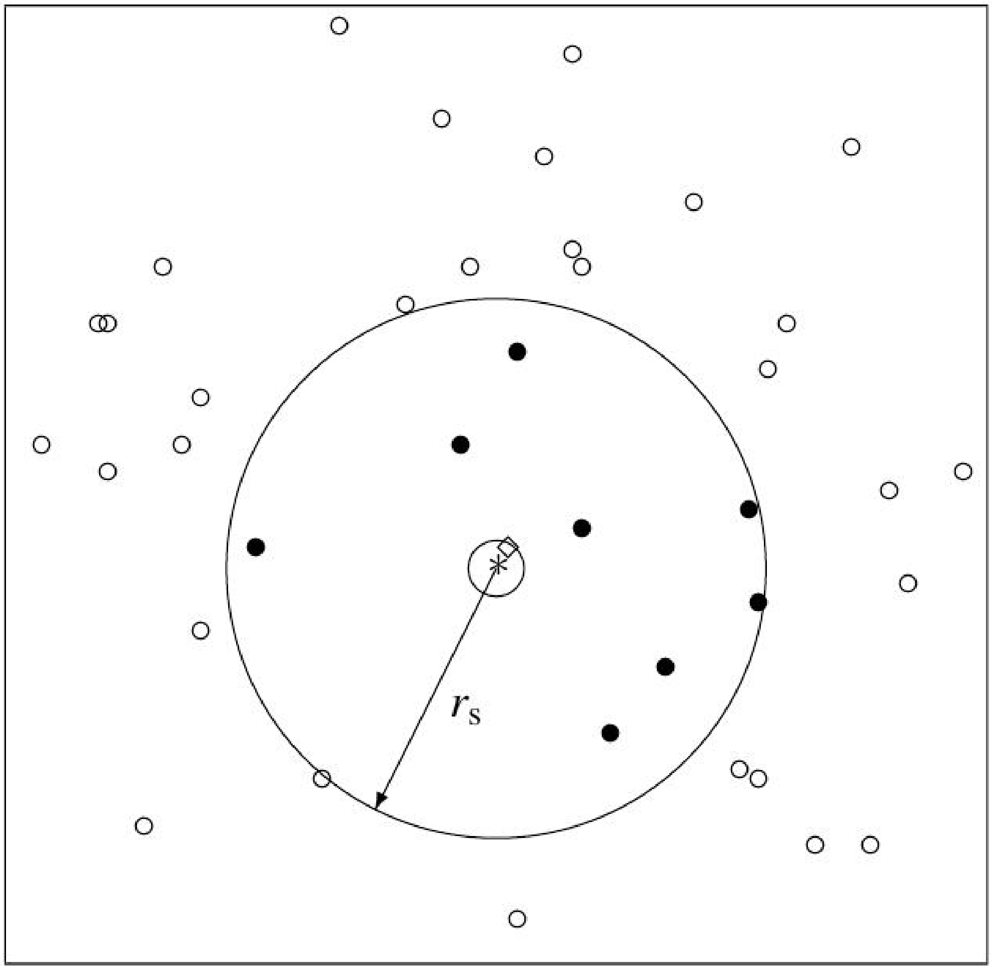

FIGURE 3.2: Illustration of a neighbour sphere. Source: (Aarseth, 1985).

On the other hand, NBODY6++ controls size of a neighbour sphere iteratively by retaining an optimal number of neighbours (Khalisi, Wang, and Spurzem, 2014). It is more convenient to scale the computational time with particle number in large-scale simulations when all particles have roughly the same number of neighbours. This parameter, called $NNBOPT$, can be changed to adjust for performance requirements.

The Ahmad-Cohen scheme can be implemented together with the hierarchical block timestep method. In this case one particle has two different timesteps: irregular for force computation exerted by neighbours and regular for prediction of contribution by distant particles.

3.5 KS–Regularization

When two particles come close to each other, the right-hand side of the equations 3.2 becomes large leading to numerical errors. One way to get around this problem is to introduce a 'softening' parameter as it is done in PhiGPU (Harfst et al., 2007):

$$\mathbf{a}_i = -\sum_{i \neq j} \frac{Gm_j}{R^2 + \epsilon^2} \frac{\mathbf{R}}{R}, \tag{3.18}$$

But there is more elegant solution. We briefly describe the idea as in (Orlov and Rubinov, 2008).

Let us consider one-dimensional case of two-body problem:

$$\ddot{x} = -\frac{G(m_1 + m_2)}{x^2}, \tag{3.19}$$

where x is the distance between particles. The right-hand side has singularity at $x = 0$, but if we multiply the equation by $\dot{x}$ and integrate, we get the energy integral:

$$\dot{x}^2 - \frac{2G(m_1 + m_2)}{x} = C, \tag{3.20}$$

where C is the integration constant and is equivalent to the double total energy of the system. But, as we see, the equation is still discontinuous at $x = 0$. And now we can apply variable transformation $d\tau = dt/x$ which gives:

$$x'' - Cx = G(m_1 + m_2), \tag{3.21}$$

where prime denotes differentiation with respect to τ. Now, the equation is *regular*. The problem was that this trick did not directly apply to 3–dimensional space.

After some time (actually, more than 60 years), Kustaanheimo and Stiefel managed to solve this problem in 4D (Kustaanheimo and Stiefel, 1965) that allowed to implement the idea of regularization in numerical codes.

Instead of dealing with 3–dimensional vectors, Kustaanheimo and Stiefel introduced a 4–vector $\mathbf{U} = (U_1, U_2, U_3, U_4)$ so that:

$$U_1^2 + U_2^2 + U_3^2 + U_4^2 = R, \tag{3.22}$$

where R is the distance between two particles m_1 and m_2.

Hence, the time transformation becomes:

$$dt = Rd\tau, \tag{3.23}$$

Then, the radius-vector of particle m_2 centred at particle m_1 is:

$$\mathbf{R} = (X, Y, Z, 0) \tag{3.24}$$

Note, that here authors use 4-th 'dummy' dimension. The coordinates are transformed by Levi-Civita matrix.

$$\mathbf{R} = L(\mathbf{u}), \tag{3.25}$$

where $L(\mathbf{u})$ is the Levi-Civita matrix:

$$\begin{pmatrix} u_1 & -u_2 & -u_3 & u_4 \\ u_2 & u_1 & -u_4 & -u_3 \\ u_3 & u_4 & u_1 & u_2 \end{pmatrix} \tag{3.26}$$

which has a useful property:

$$\frac{d}{dt}(L\mathbf{U}) = 2L\mathbf{U}' \tag{3.27}$$

After taking the time derivative of Eq. 3.25, we get the relation between velocities:

$$\dot{\mathbf{R}} = \frac{2}{R} L\mathbf{U}' \tag{3.28}$$

It is also possible to express $\mathbf{U}$ and $\mathbf{U}'$ in terms of $\mathbf{R}$ and $\dot{\mathbf{R}}$ (Aarseth, Tout, and Mardling, 2008). A system of two particles, subject to KS-regularization, is called the KS-pair or regularized binary.

In the family of codes NBODY6 and NBODY6++ , the KS-pair is substituted by its centre of mass and is treated in the whole system of N bodies as a single particle.

In order to identify the potential candidates for KS-regularization, we introduce the parameter $R_{\min}$ equivalent to the impact parameter for 90 degree deflection:

$$R_{\min} = \frac{2G(m_1 + m_2)}{v_{\inf}, (3.29)}$$

where $v_{\inf}$ is the relative velocity of 2 approaching particles at infinity. As the approach is happening, the timesteps of the particles are being reduced. Hence, another parameter to decide on regularization is the minimum timestep:

$$dt_{\min} = \kappa \frac{\eta}{0.03} \left(\frac{R_{\min}^3}{< m >} \right)^{1/2}, \tag{3.30}$$

where $< m >$ is the average mass, η is the timestep factor (see Eq. 3.15) and κ is a free numerical factor.

If the particles are approaching each other they have to satisfy the condition:

$$\mathbf{R} \cdot \mathbf{V} > 0.1\sqrt{G(m_1 + m_2)R}. \tag{3.31}$$

And the final condition for regularization is to compare their mutual force with perturbations exerted by other particles:

$$\gamma = \frac{a_p R^2}{G(m_1 + m_2)}, \tag{3.32}$$

where a_p is the absolute value of the relative perturbing force. In NBODY6++ the particles are regularized if $\gamma < 0.25$. Finally, the KS-pair represents perturbed two-body motion. The perturbation parameter γ is evaluated at every timestep of the pair and if it reaches the value $\gamma_{\min} = 10^{-6}$ the pair is considered unperturbed and instead of numerical integration the analytical solution of two-body problem is applied. The unperturbed pairs are referred in the code as 'mergers'.

Part III

RESULTS

Chapter 4

Star–disc interaction in galactic nuclei

Most of the results presented in this chapter are published in the peer-reviewed article Panamarev, Taras; Shukirgaliyev, Bekdaulet; Meiron, Yohai; Berczik, Peter; Just, Andreas; Spurzem, Rainer; Omarov, Chingis; Vilkoviskij, Emmanuil "Star-disc interaction in galactic nuclei: formation of a central stellar disc", Monthly Notices of the Royal Astronomical Society, Volume 476, Issue 3, p.4224-4233. T. Panamarev analyzed the simulations output data, wrote the text, performed all necessary calculations. The co-authors contributed by initial data analysis, early draft of the paper (B. Shukirgaliyev), comments, ideas, discussion with the referee (all co-authors).

Sec. 4.2 summaries main findings of the peer-reviewed article Kennedy, Gareth F.; Meiron, Yohai; Shukirgaliyev, Bekdaulet; Panamarev, Taras; Berczik, Peter; Just, Andreas; Spurzem, Rainer "Star-disc interaction in galactic nuclei: orbits and rates of accreted stars", Monthly Notices of the Royal Astronomical Society, Volume 460, Issue 1, p.240-255. T. Panamarev contributed by improving the accretion disc model in order to increase its realism, helped with comments and ideas.

4.1 The model

The interaction of stars with the AD was studied by Rauch (1995) and Rauch (1999). A later semi-analytic approach of star–disc interactions (Vilkoviskij and Czerny, 2002) led to conclusion that competition between stellar two-body relaxation and dissipation will cause a disc-like structure in the inner stellar component and a well-defined stationary flux of stars towards the SMBH. The effects of gas damping in dense stellar systems were studied by Leigh et al. (2014) analytically and numerically. The authors conclude that the gas drag may increase the stellar accretion rate onto the SMBH in galactic nuclei while the effect of the star-gas interactions on the mass segregation rate is relatively inefficient in case of dense galactic nuclei. Stellar migration towards the SMBH in AGN was analysed by McKernan et al., 2011 where the authors considered compact massive stellar objects migrate by analogy with protoplanetary migration. In result, the migration and accretion of compact objects can explain the X-ray soft excess in Seyfert AGN. Baruteau, Cuadra, and Lin (2011) performed hydrodynamical simulations of the gaseous disc in order to study the migration of a binary star through the disc and they found that the hardening of the binary happens on much shorter time-scales than the migration towards the SMBH. It is natural to expect the presence of stellar mass black holes (sBH) in the AD where they can accrete material and grow or even accumulate in a migration trap and merge resulting in a formation of intermediate mass black holes (Artymowicz, Lin, and Wampler, 1993; Bellovary et al., 2016). The gaseous drag would effectively reduce the semi-major axis of sBH binary resulting in a strong gravitational wave emission followed by a merger within the lifetime of the AD (Bartos et al., 2017; Stone, Metzger, and Haiman, 2017; McKernan et al., 2017).

Three main dynamical components of AGN are: a SMBH, an AD and a compact stellar cluster. In order to couple stellar dynamics and the drag force from the AD, we use an improved version of the direct N-body code $\phi GRAPE$ (Harfst et al., 2007) including the friction force of stars in the AD. The code is parallel and uses GPU accelerators for the calculations of gravitational force. The integration of the equation of motion is done using the 4th order Hermite scheme. For more details see Just et al., 2012. The $\phi GRAPE$ code was used in Just et al., 2012 as well as in many other papers on galactic nuclei and tidal disruption events (e.g. Zhong, Berczik, and Spurzem, 2014; Zhong, Berczik, and Spurzem, 2015; Kennedy et al., 2016; Li et al., 2017).

In order to estimate the stellar accretion rate onto the SMBH, the effects of stellar tidal disruptions were included in the simulation. It was done in a way that if an object crosses the accretion radius $r_{\rm acc}$ then it is considered to be tidally disrupted and 100% of the mass is added to the mass of the SMBH. We used the $r_{\rm acc}$ as a free numerical parameter which regulates the spatial resolution.

We use the data from the most realistic simulation where the number of stars was set to $N = 1.28 \times 10^5$, the accretion radius $r_{\rm acc} = 3.0 \times 10^{-4} r_{\rm inf}$ (the most realistic simulation of Kennedy et al. 2016, designated as 128k03r). The scale height of the AD was set to have linear dependence on radius in the inner region (see next subsection). We compare the data with the analogous 128k simulation without the AD (128k03ng). The number of particles in the simulations is still much smaller than the number of stars in a real galactic centre, so each particle represents a group of stars. Detailed description of the scaling procedure of star–disc interactions is given in Just et al., 2012.

We use Hénon units (also known as N-body units) throughout this chapter (Ch. 4) unless other is specified. The total mass of the NSC as well as the gravitational constant G are set to unity. We set the initial mass of the SMBH and the AD to be 10% and 1% of the total stellar mass, respectively. The SMBH grows due to the capture of stars while the AD remains stationary.

4.1.1 The accretion disc

Our model of the AD corresponds to an axisymmetric thin disc based on Shakura and Sunyaev (1973) and Novikov and Thorne (1973). The gas density is given by

$$\begin{aligned}\rho_{\rm g}(R,z) &= \frac{2-p}{2\pi\sqrt{2\pi}}\frac{M_{\rm d}}{hR_{\rm d}^3}\left(\frac{R}{R_{\rm d}}\right)^{-p} \\ &\quad \exp\left[-\beta_s\left(\frac{R}{R_{\rm d}}\right)^s\right]\exp\left(\frac{-z^2}{2h^2}\right), \end{aligned} \tag{4.1}$$

where $p = 3/4$ is the surface density power-law corresponding to the outer region of standard thin disc model, R is the radial distance from the SMBH, z is the vertical distance from the disc plane, $R_{\rm d} = 0.22$ is the radial extent of the disc (scaled with the influence radius of the SMBH). The parameters $s = 4$ and $\beta_s = 0.7$ are associated with the smoothness of the outer cutoff of the disc (introduced for numerical reasons) and h is the scale height. The gas in the disc is set to have Keplerian rotation profile. The total disc mass is fixed to be $M_{\rm d} = 0.01$ and the gravity force from the AD is neglected.

We approximate the disc scale height in the inner region with a linear relation $h = \frac{R}{R_{sg}} h_z$ up to a distance $R_{sg} \approx 0.026$ where the vertical self-gravity of the disc becomes important. It gives the opening angle of the AD a value of 0.5°. In the region of a vertically self-gravitating disc, the scale height is constant $h = h_z$. The transition between two regions is estimated by equating the vertical component of the spherically symmetric force from the SMBH at $z = h_z$ with the vertical self-gravitation of a thin disc above the AD. We examined the effects of changing the inner disc height profile on the results in Kennedy et al., 2016.

4.1.2 Stellar component and star–disc interactions

The initial conditions are generated in the following way. We place a point-mass potential into a Plummer sphere (with virial radius of one Hénon unit) and evolve the system to the stage of dynamical equilibrium $t = 0.001 t_{rel}$ (several crossing times). After that, the influence radius of the SMBH (the enclosed radius where the total stellar mass equals to that of the SMBH) is measured to be $r_{inf} = 0.22$. The NSC consists of equal mass stars. Then the interaction with the AD is 'switched on'. The total simulation time is 2 half mass relaxation times (t_{rel}).

Since we neglect the gravity of the AD, a star feels the gas as a drag force which is given by the equation

$$\mathbf{F}_{drag} = -Q_d \pi r_\star^2 \rho_g(R,z) \left|\mathbf{V}_{rel}\right| \mathbf{V}_{rel}, \tag{4.2}$$

where ρ_g is the local gas density (equation 4.1), $r_\star$ is the stellar radius and V_{rel} is the relative velocity between the star and the gas, Q_d is the drag coefficient, we use $Q_d = 5$ (Courant and Friedrichs, 1948). We assume that stars have supersonic motion while crossing the disc and therefore we treat the drag as a ram pressure effect. Contribution from the dynamical friction is neglected since it is proportional to V_{rel}^{-2} while the ram pressure drag goes with V_{rel}^2 (see Ostriker 1999 and Sec. 2.2 of Just et al. 2012).

Since a star particle represents a group of stars, we scale equation (4.2) by introducing an effective dissipative parameter,

$$Q_{tot}(N) \equiv Q_d N \left(\frac{r_\star}{R_d}\right)^2. \tag{4.3}$$

This expression describes the dimensionless total dissipative cross section of N stars, normalized to the disc area. Now, Eq. 4.2 can be rewritten as acceleration in terms of global quantities, such as R_d, M_{cl} and Q_{tot}:

$$\mathbf{a}_d = -Q_{tot} \frac{\pi R_d^2 \rho_g}{M_{cl}} \left|\mathbf{V}_{rel}\right| \mathbf{V}_{rel}, \tag{4.4}$$

where M_{cl} is the total stellar mass. To get around the fact that the relaxation time in the modelled system is shorter than the t_{rel} for a real galactic nucleus, we choose Q_{tot} in such a way that the ratio between the dissipation time-scale and the relaxation time is conserved. Thus, given a galactic centre with N_{real} stars and an effective dissipative parameter $Q_{tot}(N_{real})$, the value of $Q_{tot}(N_{sim})$ to be used in a simulation with N_{sim} superparticles is

$$Q_{tot}(N_{sim}) = \frac{t_{rel}(N_{real})}{t_{rel}(N_{sim})} Q_{tot}(N_{real}). \tag{4.5}$$

We refer to Just et al., 2012 for a detailed description.

We neglect effects from stellar feedback to the disc (including crossings and winds) and do not take into account the gravitational potential of the AD. Some of this assumptions are discussed in Sec. 4.5, but we leave the detailed analysis for future work.

4.2 Orbits and rates of accreted stars

In this section we briefly describe our results reported in Kennedy et al., 2016 as in the next chapter we aim to **extend this work**.

When a star particle crosses the gaseous disc it feels action of the drag force (equation 4.2) – its orbit gradually shrinks and tends to align with the disc plane; eventually, the SMBH captures the star.

In order to recreate the plunge history of stars captured by the black hole, we measure the orbital eccentricity at the moment of accretion. This then gives us three possible scenarios: (1) *disc capture* – eccentricity is close to zero ($e \sim 0$), (2) *gas assisted accretion* – moderate eccentricity ($e < 1$) and (3) *direct accretion* – eccentricity is close to one ($e \sim 1$). In each of these categories a star *may* go through five phases: (1) scattering, (2) slow decay, (3) fast decay, (4) disc migration and (5) radial infall. In the first phase only interactions between other stars cause change in angular momentum and binding energy while the disc is far away and its action is negligible. The slow decay phase begins when the star's orbit is scattered towards the disc so that the star starts 'feeling' the drag force. The fast decay phase – as its name suggests – features rapid orbital decay and happens when the star is almost aligned with the disc. The star on nearly circular orbit fully aligned with the disc plane experiences the disc migration phase until it is captured by the SMBH. The radial infall phase is only experienced by plunge type 3 stars which do not interact with the disc and are subject to the loss-cone mechanism. So, the defined above plunge types reflect a star's path to the accretion. The plunge types 2 and 3 also feature uniform distribution of orbital inclinations, while plunge type 1 stars are accreted in the AD plane (inclinations are close to zero).

As an example, we select stars from the three plunge categories and show (see Fig. 4.1) how their semi-major axis, eccentricity and inclination change in time *before* the star is accreted. Panels (a) and (b) show the disc capture with one example accreted from a prograde orbit and another from a retrograde one (relative to the orbits of gaseous disc particles). After both of them align with the disc, their orbits rapidly become circular.

4.3 Formation of a central stellar disc

In the previous section (Sec. 4.2), we analysed statistics of orbital parameters of accreted particles and found that the paths that they take to accretion depend on their final eccentricities and inclinations. We identified three broad paths or *plunge types*, these are (1) disc capture, (2) gas assisted accretion, and (3) direct accretion. The plunge type 1 stars were captured by the AD and went through a disc migration phase. Here we focus on the migration phase and examine how it shapes the inner parts of the stellar system.

Figure 4.2 shows the cumulative distribution of inclination i and eccentricity e at the time of accretion. The blue and red lines in the Fig. 4.2 clearly show that about 40% of all accreted particles throughout the simulation are accreted with very low

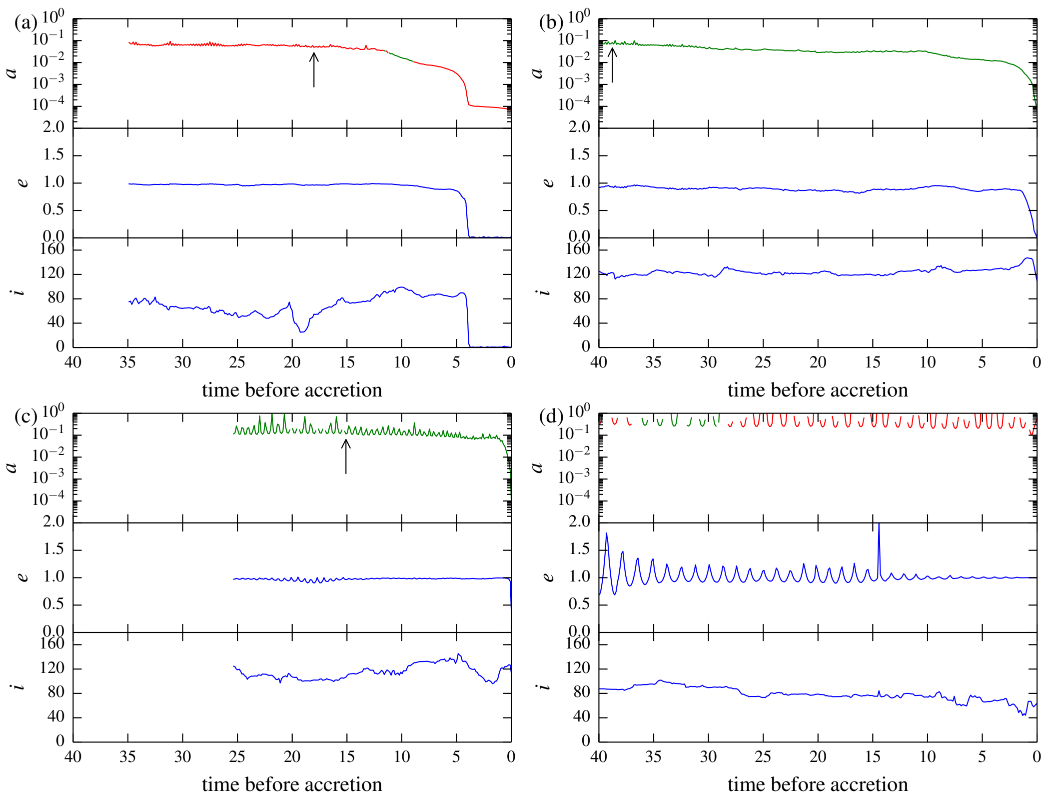

FIGURE 4.1: "Semi-major axis, eccentricity and inclination of a few sample orbits for the three types described in Section 4.2. The semi-major axis is plotted in red when the orbits is prograde ($i < 90°$) and green when retrograde. Panel (a) shows a disc captured star with $e_{acc} \sim 0$ and low inclination prograde orbit, (b) shows a star captured into the disc on a retrograde orbit, (c) shows a gas assisted accretion $e_{acc} < 1$ where the inclination distribution for those orbits is uniform, (d) shows a direct accretion onto the SMBH with $e_{acc} \sim 1$ and also from a uniform inclination distribution. Black arrows indicate where the decay phase begins (see text). Panel (d) shows a direct capture, and thus has no decay phase; the gaps in the semi-major axis occur when the orbit is instantaneously unbound". Source: Kennedy et al., 2016

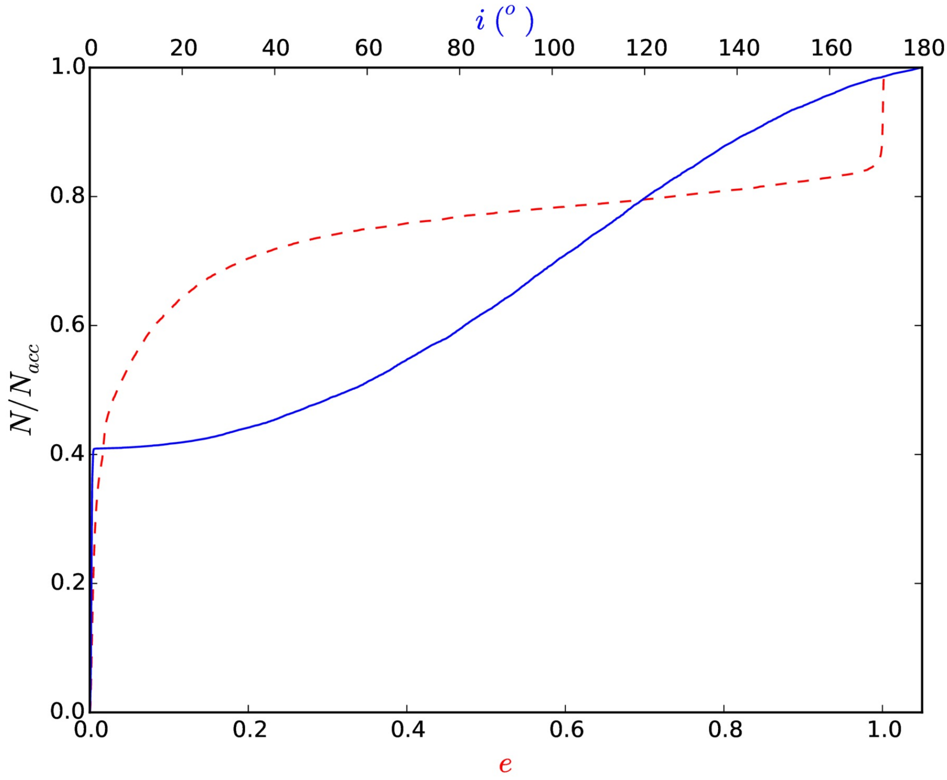

FIGURE 4.2: Cumulative distribution of the orbital parameters of all accreted particles at the moment of accretion. The red line represents eccentricity distribution and corresponds to the bottom X-axis. The blue line represents inclination angle distribution and corresponds to the top X-axis.

inclinations and eccentricities meaning the accretion through the AD (plunge type 1). As we will show, these particles were accreted only after several orbital times of residency inside the disc. While on the migration phase, the particles form a nuclear stellar disc (NSD) as we show later. Moreover, the stellar disc remains stationary during the simulation and is supported by a constant inflow of stars from the outer parts of the NSC. In the following sections, we examine the properties of the NSD and the stellar migration time-scale.

4.3.1 Spatial distribution of the NSD particles

The initial mass profile as well as the mass–radius dependence for the models with and without the AD at $t = t_{\rm rel}$ are presented in Fig. 4.3. The cumulative mass profile of the NSC at 1 and 2 relaxation time reveals the mass concentration in the inner part of the cluster, the profile remains very similar also at 2 relaxation times. Although the stellar accretion from disc-captured particles occurs, we see no change in the mass profile after another relaxation time, that means that the stellar disc is continuously supplied from the NSC. The mass of the NSD stays the same in order of magnitude and equals to $M_{\rm NSD} \approx 7.0 \times 10^{-4}$ at the end of the simulation.

Figure 5.4 shows spatial density distribution of the NSC. As we can see from the Fig. 5.4 the initial Plummer sphere (looks like a triangle in the logarithmic z vs R plane) is slightly distorted inwards due to the presence of a SMBH, while the AD leads to the formation of a 'tail' of stars in the innermost part of the cluster with

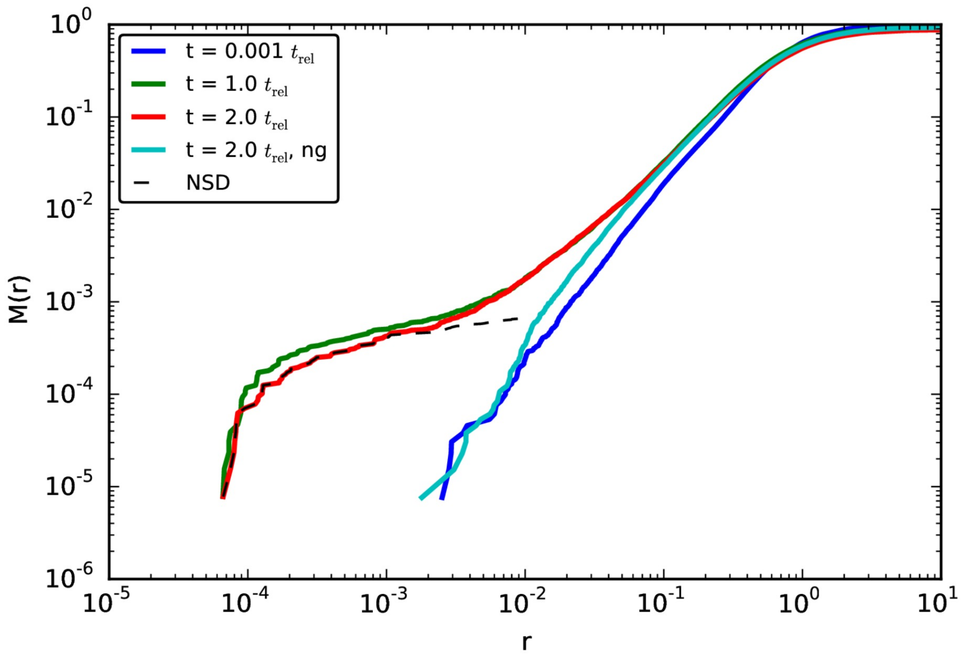

FIGURE 4.3: Evolution of the NSC. Cumulative mass profiles. Blue and cyan lines represent the initial model and model without the AD at the end of simulation, red and green lines show NSC mass profiles at 1 and 2 $t_{\rm rel}$ respectively. The black dashed line is the cumulative mass of the stellar disc.

$|z| \ll R$. The 'tail' can be clearly visualized as a disc of stars (Fig. 4.5). We call the disc of stars the *nuclear stellar disc*.

In order to investigate the properties of the NSD particles and the NSD as a whole, we have to define the criterion for a stellar disc particle. The 'tail' in Fig. 5.4 panel (c) gives us constrains on vertical and radial distances of the NSD particles. Comparing panels (b) and (c) of the same figure we set the condition: $R < 10^{-2}$ & $z < 10^{-3}$. Further on we require $e < 0.5$ in order to remove transient particles and since the orbital inclination angle is derived as $\cos i = \frac{L_z}{|L|}$, the condition $\cos i > 0.0$ excludes the counter-rotating stars from the NSD. Putting all together we define the NSD particles as particles that satisfy the following criteria:

$$\begin{aligned} &R < 10^{-2}; z < 10^{-3}; \\ &\cos(i) > 0.0; e < 0.5. \end{aligned} \tag{4.6}$$

where R is the projected distance to SMBH.

We ensure that these criteria select plunge type 1 stars by plotting the distribution of selected NSD particles in eccentricity–inclination plane when they still live in the stellar disc ($t = 1.0 t_{\rm rel}$) and when they were accreted onto the SMBH ($t = t_{\rm acc}$). Fig. 4.6 shows that all these particles were accreted with very low values of eccentricity and orbital inclination. The size of the NSD is ≈ 3 times smaller than the effective radius of the AD ($R_{\rm eff}$ in Kennedy et al. 2016; a characteristic location in the AD where most stars begin their plunge).

Figure 4.7 shows that the inclination declines approximately proportional to the size of the orbit as expected due to the friction force in a Kepler rotating AD. The

(a) $t = 0.001t_{\mathrm{rel}}$

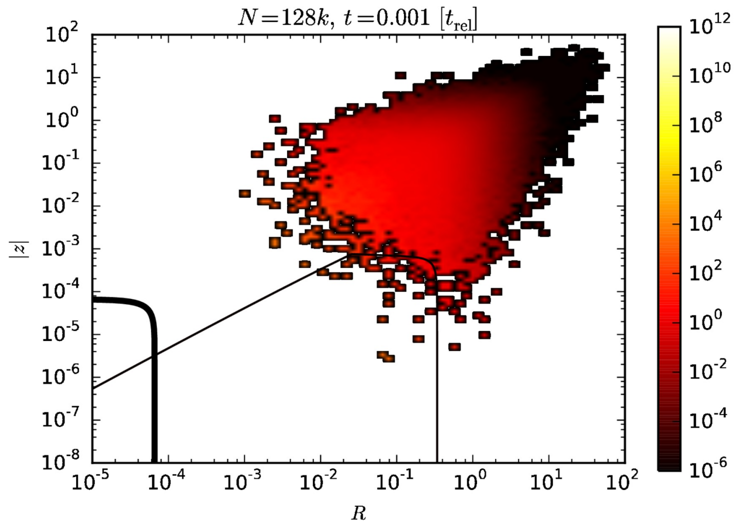

(b) $t = 2t_{\mathrm{rel}}$, without AD

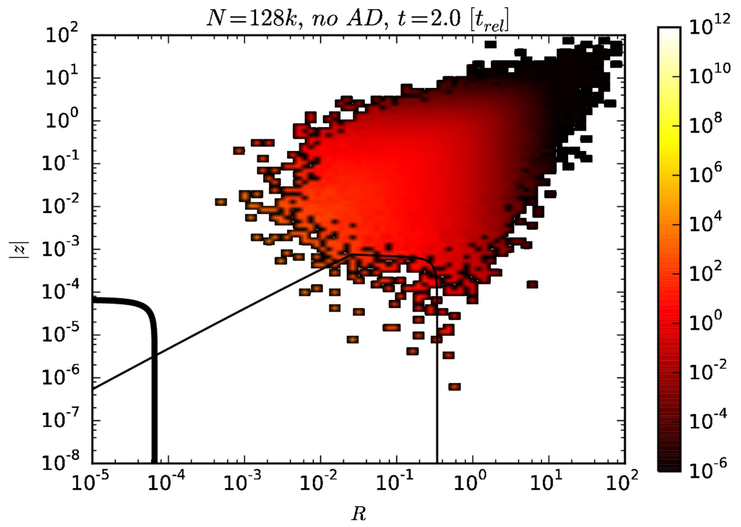

(c) $t = 2t_{\mathrm{rel}}$, with AD

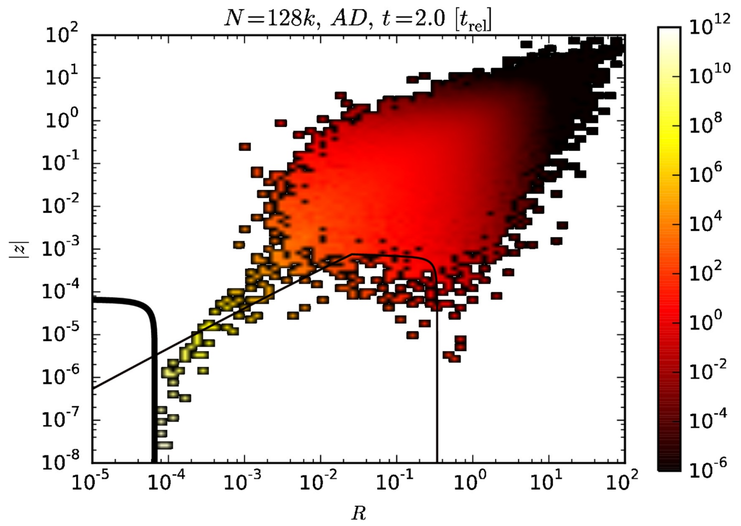

FIGURE 4.4: Density distribution of NSC. The thick black line represents the accretion radius r_{acc} and the thin line stands for the accretion disc density $\rho = 1$. The colour-code indicates stellar volume density.

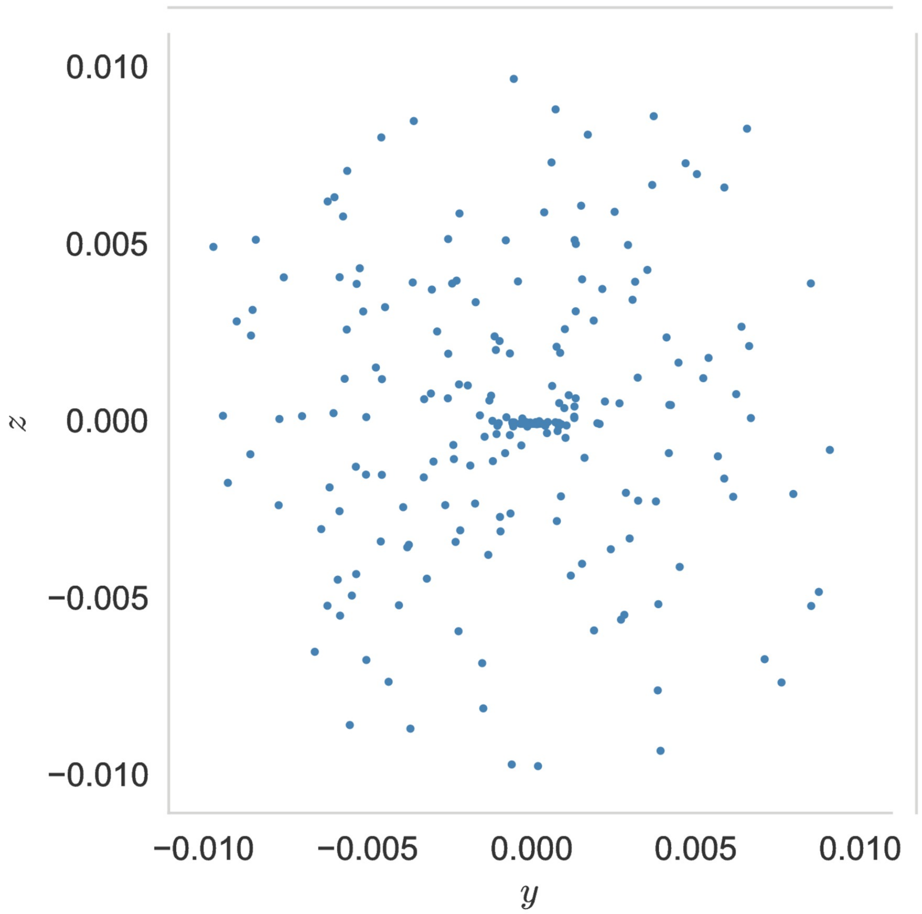

FIGURE 4.5: Spatial distribution of stars inside $r = 0.05 \times R_{\rm d}$ in YZ plane at time $t = 1.0t_{\rm rel}$. At the centre a disc-like structure formed due to star–disc interactions.

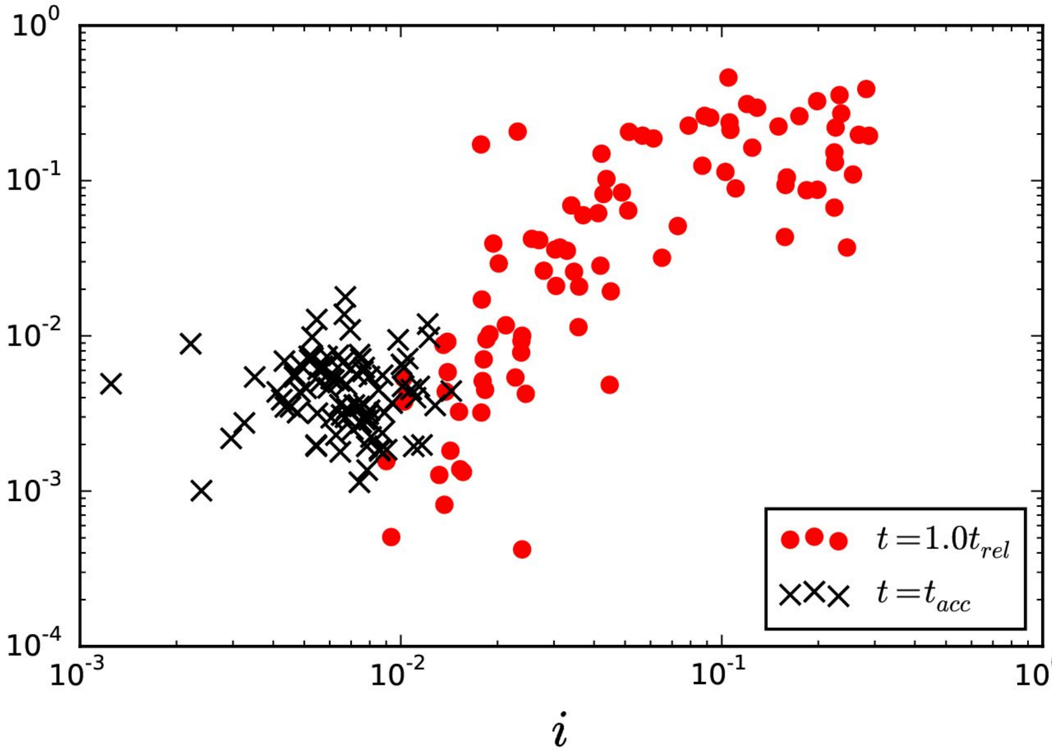

FIGURE 4.6: Distribution of the disc particles in eccentricity–inclination plane at the $t_{\rm cur} = 1.0 t_{\rm rel}$ (red circles). The black crosses are the eccentricity and inclination values of those stars at their time of accretion.

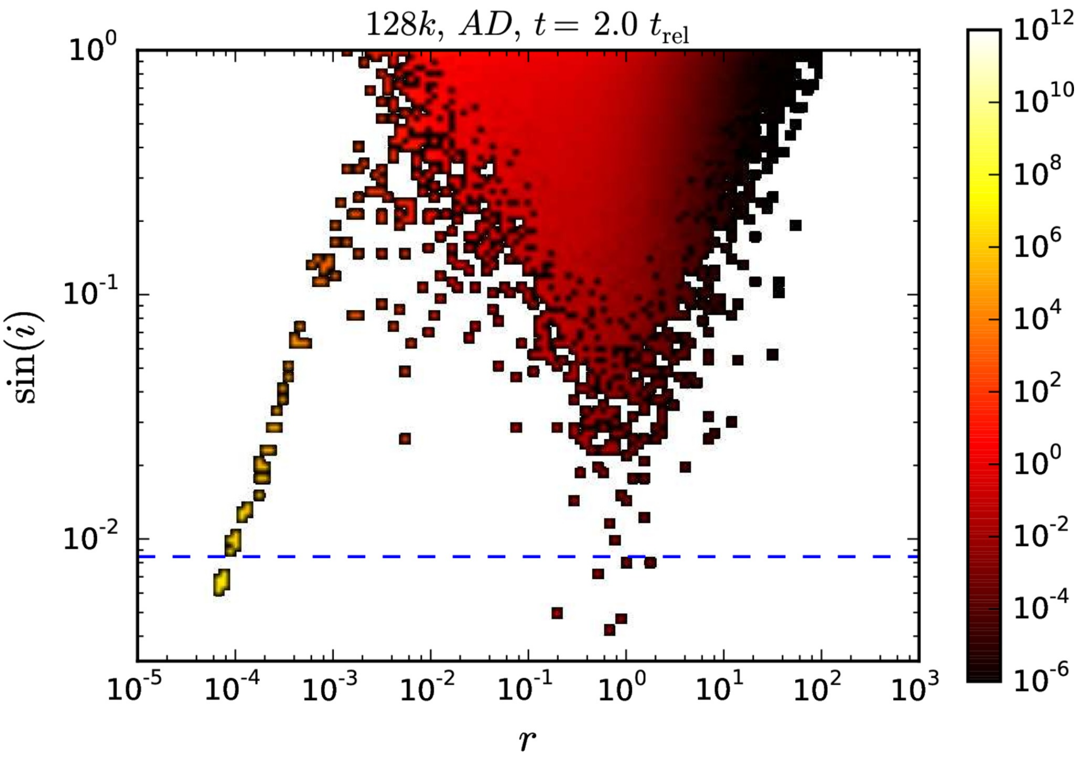

FIGURE 4.7: Inclination angles of all stars depending on a distance from SMBH coloured by the stellar density. Blue dashed line indicates the opening angle of the AD.

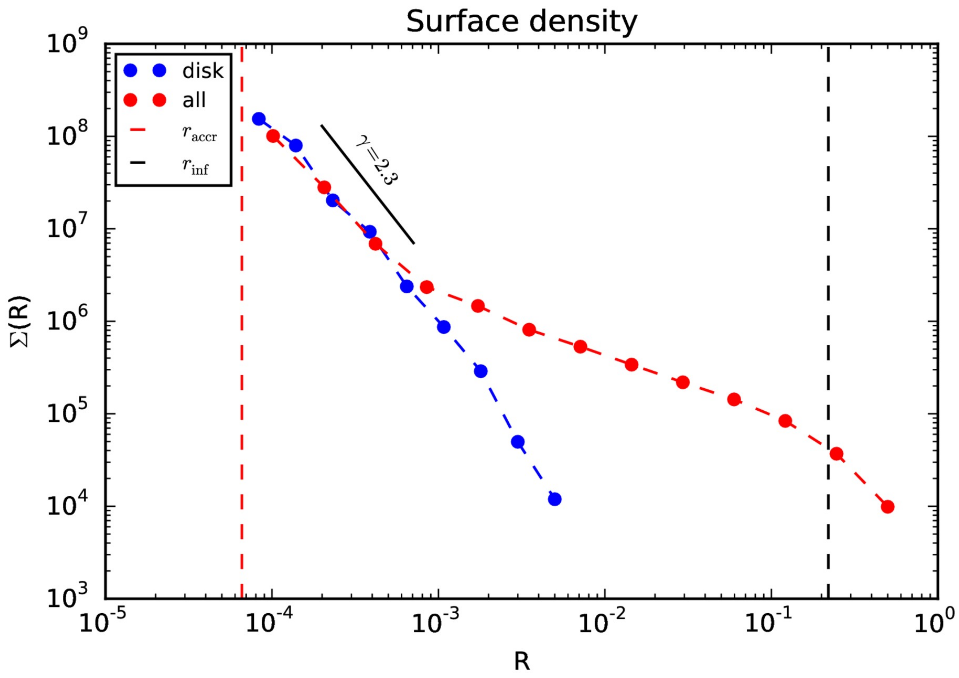

FIGURE 4.8: Surface density of the NSD. Red dotted line represents all NSC stars, the blue one shows only the stars that belong to NSD. Dashed red and black vertical lines represent the accretion radius and the influence radius respectively.

surface number density of the NSD at $t = t_{\rm rel}$ is displayed in Fig. 4.8. The figure shows strong overdensity in the inner region ($r < 10^{-3}$) of the NSC. The surface density features a steep power law profile with $\gamma = 2.3$.

4.3.2 Lifetime and evolution of the NSD.

A look at some properties of the NSD stars at some arbitrary current time $t_{\rm cur}$ and the time left for the accretion gives details on how and how fast these properties change during the migration phase. Fig 4.9 shows time left for accretion against the orbital parameters of the NSD particles at time $t_{\rm cur} = t_{\rm rel}$ and demonstrates the decay of eccentricities and inclinations in the migration phase. All the NSD particles accrete in a fraction of the relaxation time. Figure 4.10 shows the same distribution as the bottom panel of Fig. 5.4, but colour coded by the time left to accretion for all stars in the NSC. It is clearly seen that there is an inflow of the particles towards the SMBH at $R < 10^{-3}$.

In order to compute the time a star spends inside the AD during the plunge, we track it from the moment it is captured (equation 4.6 is fulfilled) and follow the stellar orbit until it is gone inside the accretion radius (Fig. 4.11). We tracked all NSD particles from the beginning of the simulation up to $t = 1.8t_{\rm rel}$ and found that the median time (between capture and accretion) equals to $t_{\rm migr} = (0.026 \pm 0.002)t_{\rm rel}$ and represents the fact that 50% of all the NSD stars spend in the disc no more than $t_{\rm migr}$. On the other hand it represents the renewal time of the NSD as we show below.

Indeed, the cumulative number of stars captured by the AD is a linear function of time (see Fig. 4.12) and its derivative represents the total stellar influx:

$$f_{\rm NSD} \equiv \frac{dN_{\rm cap}}{dt} = 3.649 \pm 0.001 \tag{4.7}$$

where $N_{\rm cap}$ is the cumulative number of stars captured by the NSD (but not necessarily the number of stars actually residing in the NSD, as stars eventually are accreted onto the SMBH) and $f_{\rm NSD}$ is the stellar flux, or the capture rate by the AD which equals $\simeq 3.65$ particles per N-body time unit (this is the straight line fit in Fig. 4.12).

The number of stars resident in the NSD is roughly constant in time and its average value is $\langle N_{\rm NSD}\rangle = 81.5$ with standard deviation of 8.7. From this number and the influx rate, we can calculate a characteristic time-scale in which the entire resident stellar population of the NSD is replaced. We define this time-scale as the renewal time, which is then:

$$t_{\rm renew} = \frac{\langle N_{\rm NSD}\rangle}{f_{\rm NSD}} = 22 \pm 2 \tag{4.8}$$

As expected, $t_{\rm renew}$ is $\simeq 2.5\%$ of the half-mass relaxation time, and equals the migration time calculated previously $t_{\rm migr}$. This time-scale is also associated with the formation time of the NSD.

Comparison of the migration time with the stellar dissipation time $t_{\rm diss} = E_{\rm kin}/\dot{E}_{\rm sd}$ (see Eq.(16) of Just et al. 2012), where $E_{\rm kin}$ is the kinetic energy of all stars and $\dot{E}_{\rm sd}$ is the total energy dissipation rate due to the AD, shows that $t_{\rm diss}$ exceeds $t_{\rm migr}$ by two orders of magnitude. On the other hand, the viscous time scale of the AD

$$\tau = \left(\frac{h}{R_{\rm d}}\right)^{-2} \frac{1}{\alpha\Omega} \tag{4.9}$$

can be shorter or longer than the effective migration time and depends on the viscosity parameter α (Fig. 4.13). Here Ω is Keplerian orbital frequency.

The total number of accreted stars onto the SMBH is greater than total number of stars captured by the AD because there is also a contribution from higher eccentricity orbits (plunge types 2 and 3 from Kennedy et al. 2016). Fig. 4.14 shows long-term origin of accreted stars in the interval 1 - 2 $t_{\rm rel}$ including all plunge types. We clearly see that $\sim$50% of stars accreted quickly are captured by the AD. On the other hand a significant fraction originate from $r = 0.1 - 1$ and at first scattered into the loss cone before being accreted or captured. The change in the shapes of the curves shows the consistency with the derived value of the effective migration time.

We note that a closer look at the spatial distribution of the stellar disc particles reveals small precession of the disc and warps. But the dynamics of individual NSD particles relative to each other is complex and lies beyond the scope of this work.

4.4 Scaling to real galactic centres

For calibration to real systems, the value of $Q_{\rm tot}$ have to be chosen accordingly (all other parameters in our simulations are independent of N). For example, when scaling the results of the simulation with $N = 1.28 \times 10^5$ to M87 using Eq. 4.3, Eq. 4.5 and data from Table 4.1, we get the values of $Q_{\rm tot}(1.28 \times 10^5) = 5.42 \times 10^{-4}$ and $Q_{\rm tot}(6.6 \times 10^{10}) = 2.1 \times 10^{-9}$. Thus, the value is artificially enlarged by 5 orders of magnitude setting the dissipation and relaxation time-scales in correspondence. The

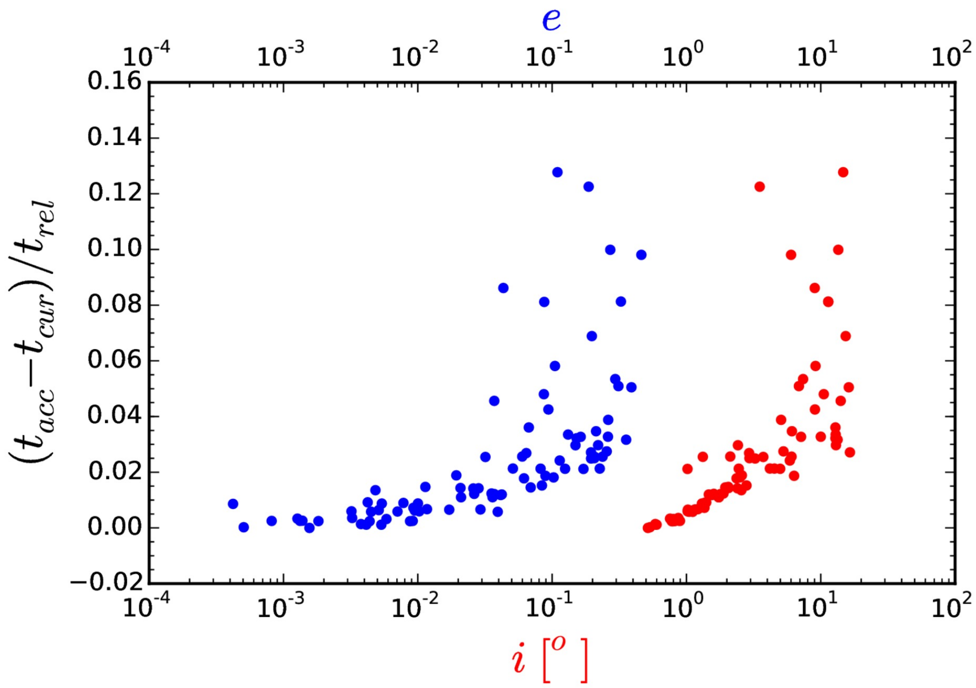

FIGURE 4.9: The time intervals left to the accretion as function of the inclination (lower horizontal axis) and eccentricity (upper horizontal axis) at $t = 1.0t_{\rm rel}$ of the disc particles.

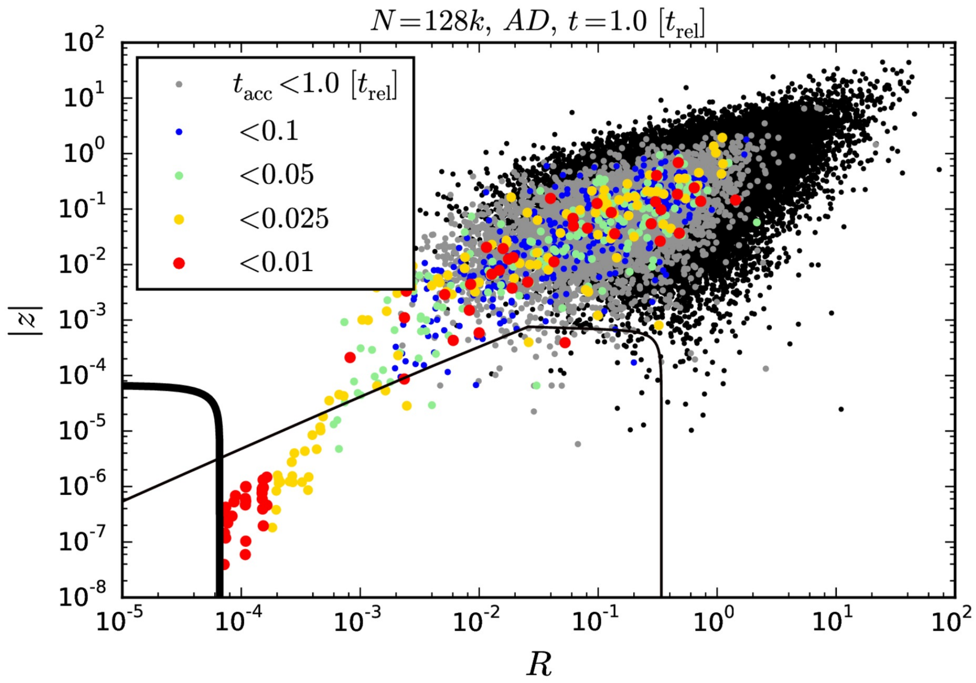

FIGURE 4.10: Spatial distribution of all stars in the NSC at $t = 1.0t_{\rm rel}$ coloured by the time left for the accretion. Thick and thin black lines are the same as in Fig. 5.4

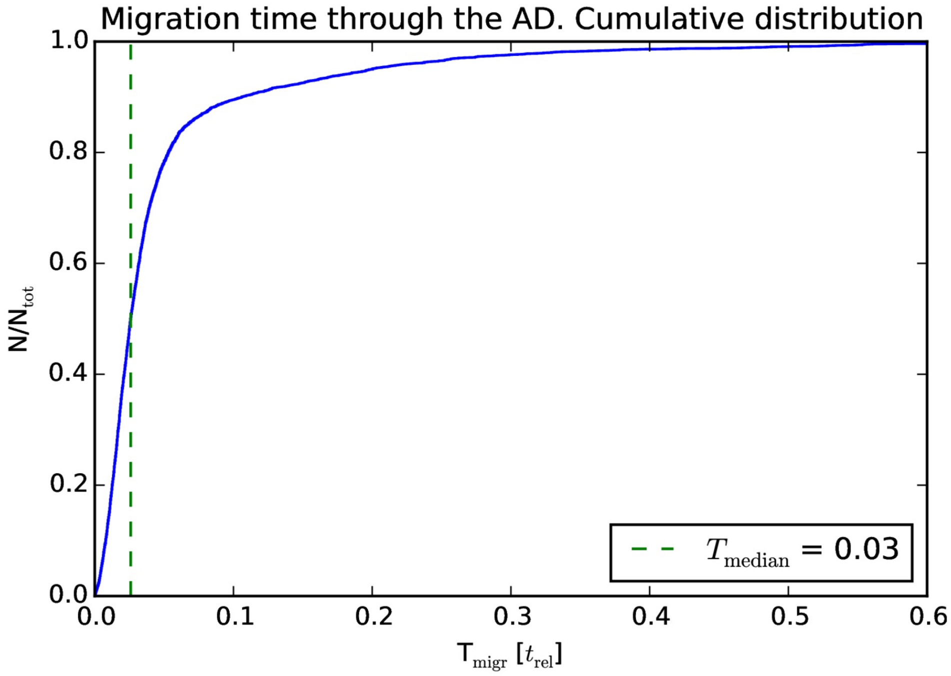

FIGURE 4.11: Cumulative histogram of the time intervals from the moment of capture by the AD until the accretion to the SMBH. Dashed vertical lines represent median and mean time correspondingly.

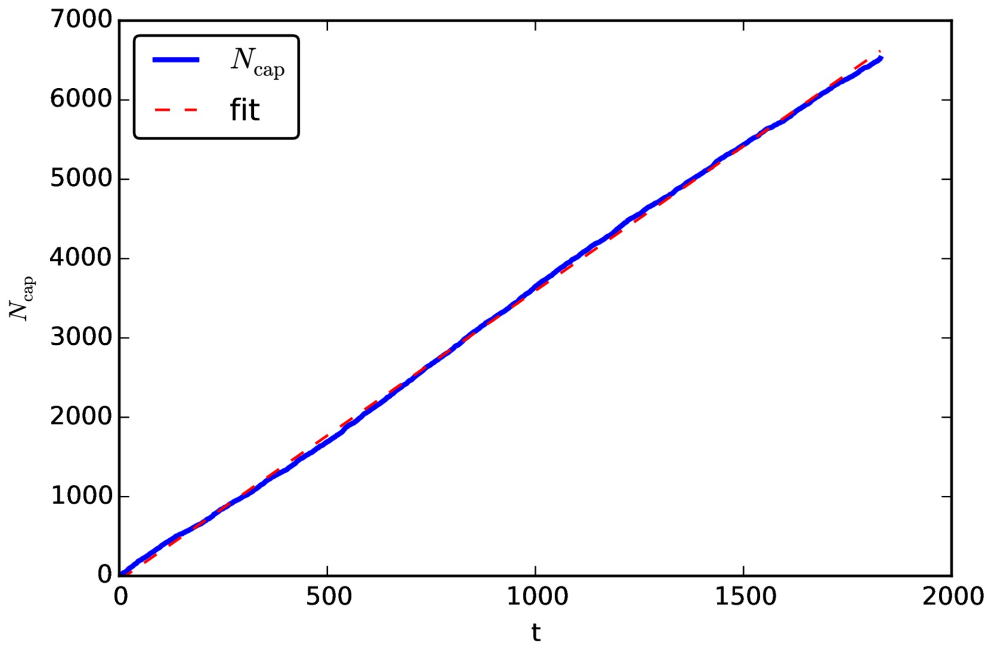

FIGURE 4.12: Cumulative number of new captured particles by the AD. The dashed line shows linear fit $N_{cap} = kt$ with $k = 3.65$

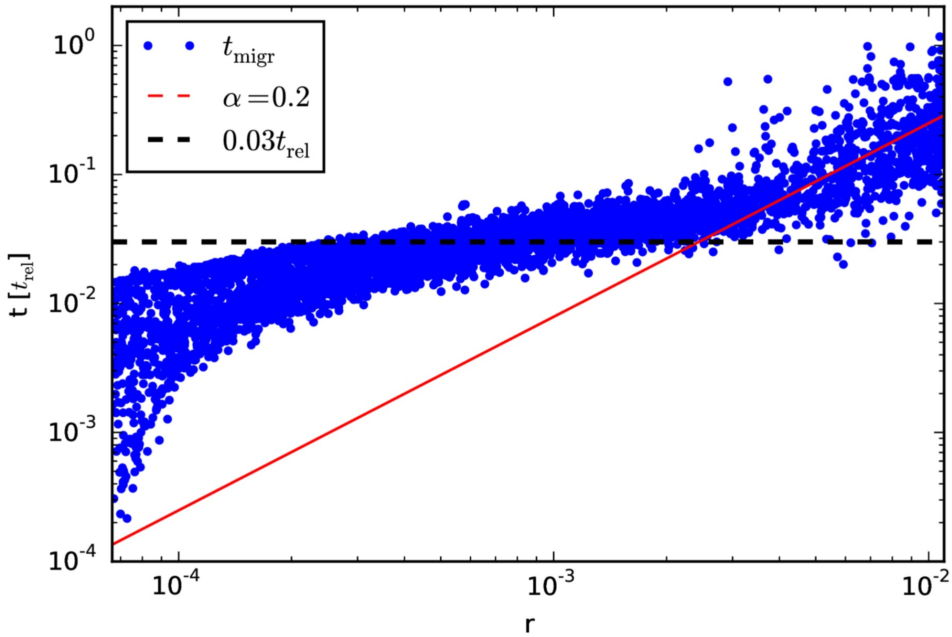

FIGURE 4.13: Migration time as a function of distance from the SMBH at which the stars 'enter' the NSD. The red line represents the AD viscous time-scale with $\alpha = 0.2$, the dashed line shows the effective migration time .

TABLE 4.1: Predicted nuclear stellar disc properties for a sample of galactic nuclei.

Object	M_{SMBH} ($M_\odot$)	r_{inf} (pc)	t_{rel} (Gyr)	M_{NSD} ($M_\odot$)	R_{NSD} (pc)	T_{migr} (Gyr)
M 87	6.6×10^9	291	6×10^5	4.6×10^7	14.55	18000
NGC 3115	9.6×10^8	78	3.4×10^4	6.72×10^6	3.9	2040
NGC 4291	3.2×10^8	24	3400	2.24×10^6	1.2	729
M 31	1.5×10^8	25	2690	1.05×10^6	1.25	238
NGC 4486A	1.3×10^7	4.5	68.8	9.1×10^4	0.225	16.7
MW	4.0×10^6	1.4	7.2	2.8×10^4	0.07	5.35
M 32	3.0×10^6	2.3	12.9	2.1×10^4	0.115	2.76

Notes. We extrapolate results to this sample of galactic nuclei (adopted from Just et al. 2012 and Kennedy et al. 2016). Columns 1–4 are the object's name, SMBH mass, radius of influence (calculated from the stellar velocity dispersion) and half-mass relaxation time, respectively. Column 5 gives the mass of the nuclear stellar disc; Column 6 gives the maximum radial size of the NSD; Column 7 gives *upper limits* of the 'effective' migration time of a star through the AD to the SMBH.

scaling for arbitrary N is given by (Eq. 11 of Paper II) :

$$Q_{\rm tot}(N) \approx 5.42\ln(0.4N)/N \tag{4.10}$$

All our simulations are done according to this equation, meaning that additionally to the scaling of mass and size of the system, we also assume that the dissipation time-scale is similar to the relaxation time:

$$\eta = t_{\rm diss}/t_{\rm rel} \tag{4.11}$$

(see Eq. 16 and Fig. 6 of Paper I). Since the accretion rate scales with the friction force $a_{\rm d} \sim Q_{\rm tot}\rho \sim Q_{\rm tot}M_d$ and time-scales scale with $t_{\rm diss} \sim 1/a_d \sim 1/(Q_{\rm tot}M_d)$, for the Galactic Centre with given $M_d = 0.1M_{\rm SMBH}$ the correct $Q_{\rm tot}$ would be ~ 20 times smaller leading to a 20 times smaller accretion rate and 20 times longer time to form the NSD. If the physical $Q_d = 5$ per star is enhanced by dynamical friction by some factor 2-1000 dependent on the velocity and sound speed, then rough estimate gives that the correct value for $Q_{\rm tot}$ in the simulation would be larger by the same factor. The mass of the NSD depends on the feeding by the friction force and the loss of stars by friction. If the scatter by 2-body relaxation is not important then the stationary stellar disc would have the same mass. If 2-body relaxation determines the feeding time-scale then the NSD mass would be proportional to η and would be larger by a factor of 20 in the Galactic Centre.

In a real galactic nucleus, the total number of stars $N_{\rm real}$ is greater than the number of particles in our simulation, $N_{\rm sim}$. So in the simulation, one particle represents $N_{\rm scale} = N_{\rm real}/N_{\rm sim}$ stars. Given the core velocity dispersion σ and mass of the SMBH (can be taken for example from Gültekin et al. 2009), one can calculate the influence radius $r_{\rm inf} = GM_{\rm SMBH}/\sigma^2$ and the relaxation time (given by Eq. 8 of Kennedy et al. 2016), taking into account that the half-mass radius equals $r_{\rm hm} = 3r_{\rm inf}$. The time and length scalings are done in a way that the relaxation time of the real system is the same as the relaxation time of the modelled system, as well as the influence radius of the SMBH in the real system is the same as in the modelled system (detailed description of the scaling procedure is given in Just et al. (2012) and Kennedy et al. (2016)). $T_{\rm scale} = t_{\rm rel}^{\rm real}/t_{\rm rel}^{\rm sim}$ and $R_{\rm scale} = r_{\rm inf}^{\rm real}/r_{\rm inf}^{\rm sim}$.

The capture rate by the AD for the Milky Way is thus (see Table 4.1):

$$\frac{dN_{\rm cap}}{dt} = 3.65 \times \frac{N_{\rm scale}}{T_{\rm scale}} \approx 140[\text{stars} \times \text{Myr}^{-1}], \tag{4.12}$$

In other words, after 100 Myr of evolution, we expect 14000 stars to be trapped by hypothetical gaseous disc, while most of them would be still in the migration phase. The 'effective' migration time for the MW equals to 2.76 Gyr. At $t = t_{\rm rel}$, the mass of the NSD is 0.07% of the initial total stellar mass of the NSC, converting to solar masses we get $M_{\rm NSD} \approx 3.0 \times 10^4 M_\odot$. Note that this is an order of magnitude estimate, whereas in the real system due to mass segregation we expect more massive stars to populate the NSD. A detailed realistic simulation is our long-term goal. The mass of the NSD is of the order of magnitude the observed mass of the young stellar disc(s) in the MW $\simeq 10^4 M_\odot$ (Bartko et al., 2010), but the NSD stars should be older because of the long migration time.

Table 4.1 gives the mass and size of the NSD as well as the migration time-scale, in physical units scaled according to the SMBH mass and its influence radius in nuclei of several nearby galaxies (adopted from Just et al. 2012). This time-scales have to be treated as upper limits for the formation of the NSD. If the time is boosted

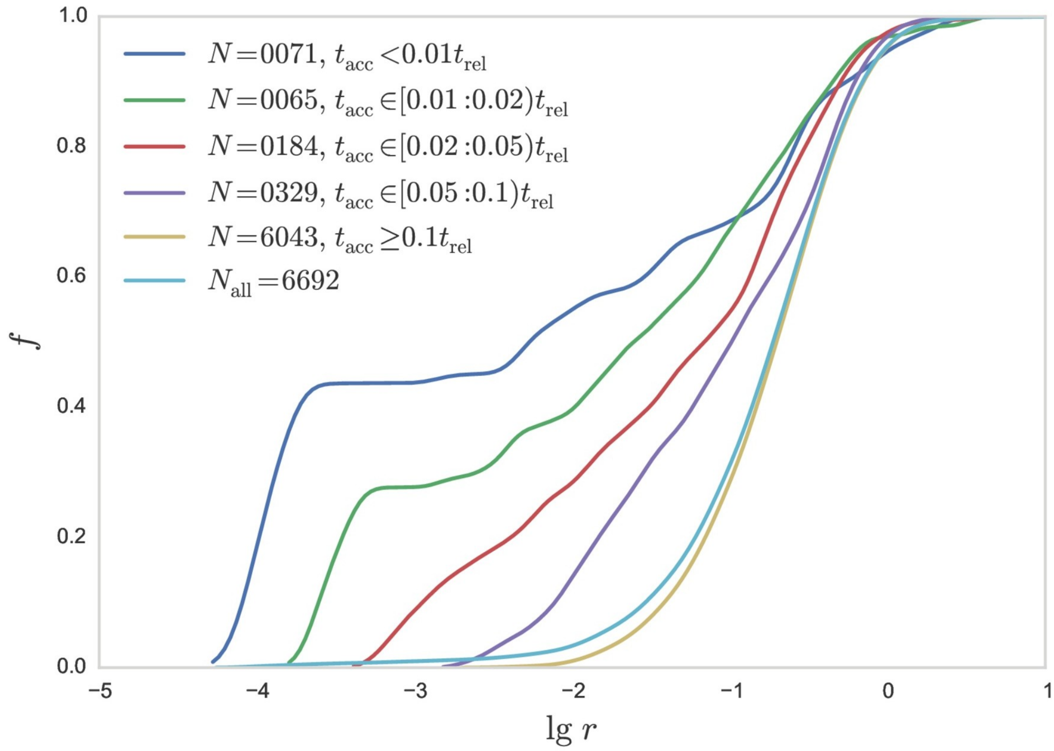

FIGURE 4.14: The distribution the time intervals left to the accretion at $t = 1.0\ t_{rel}$ of all particles captured in time interval from 1.0 to $2.0t_{rel}$.

by the dynamical friction, we can expect the presence of the NSD in lower mass systems while we do not expect stationary discs to form in massive galactic nuclei.

The stellar migration time could be boosted by taking into account the pressure gradient of the AD, but this effect is very small and only relevant for the innermost particles.

4.5 Summary and discussion

In this study we present the results from long-term simulations of a dense nuclear star cluster surrounding a star-accreting SMBH and interacting with a central gaseous disc which acts as a drag force and dissipates stellar kinetic energy. First simulations of this kind were performed and described in Just et al., 2012, improved in Kennedy et al., 2016. We examined the effect of star–disc interactions on the inner structure of the compact stellar cluster by means of direct N-body simulations. We found that the stars form a nuclear stellar disc before being absorbed or disrupted by the SMBH. The AD leads to formation of a stellar disc in very close vicinity of the SMBH with mass of $M_{NSD} \approx 0.007 M_{SMBH}$. But the AD lifetime may be too short to form the NSD. We derived the effective stellar migration time through the AD towards the SMBH. Scaling the results to the Milky Way galaxy gives the mass of the NSD $M_{NSD} \approx 3.0 \times 10^4 M_\odot$ which is the same by order of magnitude as the observed disc of young massive stars in the MW, but note that the NSD formed in our simulations consists of stars originating from the old population of the spherical NSC. The outermost stars found in our NSD are located at a distance of 0.07 pc from the SMBH.

The observed young Galactic Centre stellar disc resides between 0.04 to 0.5 pc. We think that an NSD consisting of old stars, as found in our models, could coexist with the observed stellar disc, but the old stars are just too faint to be detected. The second generation instrument for the Very Large Telescope Interferometer GRAVITY (Eisenhauer et al., 2011) or James Webb Space Telescope may be able to detect some of the NSD stars. Assuming that the young stars formed from the same AD (disc fragmentation) which created the NSD (by trapping stars), a detection of a disc of old stars (NSD) would be a strong evidence for past activity and the former presence of an AGN disc and may give some hints on the efficiency of dynamical friction in the gaseous medium near the SMBH.

Note that our results are nicely consistent with recent ideas about the non-stationary history of our own Galactic Centre, with sporadic AGN activity. The constant flow of gas to galactic nuclei inevitably produces an accumulation of gas, the formation of a central disc. This will trigger both a central AGN flare-up activity as well as a central starburst after which the gaseous disc has disappeared (e.g. Novak, Ostriker, and Ciotti, 2012). A huge Fermi bubble has been detected on both sides of the Galactic Centre (Bordoloi et al., 2017), which could be a remnant of an AGN evolutionary phase of our own galaxy several Myr ago.

The NSD is located inside the effective radius of the AD. As we have shown in Kennedy et al., 2016, it equals to $R_{\rm eff} = 0.032$ leading to an enclosed mass of $M_d(< R_{\rm eff}) = 0.09 M_d$ (note a typo of 42% in Sec. 3.2 of Kennedy et al. 2016). That means that if we would cut the disc at $R_{\rm eff}$, the AD mass would be $\simeq$ 1% of the $M_{\rm SMBH}$ with essentially the same effect. If we reduce the surface density, the enclosed mass and the force would decrease proportionally leading to a smaller accretion rate. But the stellar disc mass would be similar, because it would just take longer to pass this phase. As a consequence the formation time would be larger. On the other hand, Just et al., 2012 have shown (see their Fig. 1) that dynamical friction would be very effective if the relative velocity falls below the escape speed at the stellar surface ($\simeq 600\,{\rm km\,s^{-1}}$). The friction force would be orders of magnitude larger leading to the same accretion rate if we reduce the surface density of the AD accordingly. Inside $R_{\rm eff}$ the flattening of the potential is already a factor of 10 smaller and with the smaller surface density combined with dynamical friction, it would be completely negligible. The outer radius of the AD is chosen to be equal to the influence radius of the SMBH in the sense of $M_{\rm cl}(< R_d) = M_{\rm SMBH}$, therefore the AD mass is 10% of the M_{SMBH} and 5% of the $M_{\rm SMBH} + M_{\rm cl}$ at R_d. The correction to the rotation curve would be dominated by self-gravity of the cluster.

As was described in Sec.4.1, the contribution from the dynamical friction (in other words gravitational focusing) was ignored in this study. But in case of subsonic motion the dissipation force may be enhanced leading to faster formation time of the NSD. This enhancement can be taken into account by replacing the drag coefficient Q_d to the form of $Q_d + (v_{\rm esc}/V_{\rm rel})^4 \ln\Lambda$, where $v_{\rm esc}$ is the escape velocity from stellar surface, $V_{\rm rel}$ is the relative velocity of a star in the AD and $\ln\Lambda \simeq 10 - 20$ is Coulomb logarithm. Given that for a SMBH mass of $\simeq 10^8 M_\odot$, typical relative velocities are of the order of $1000\,{\rm km\,s^{-1}}$ at distanced below 1pc, the dynamical friction is ignored. But it can be sufficient for compact objects since the escape velocity from their surface is high. The supersonic motion of stars through the gaseous medium is an active field of research in astrophysics e.g. Thun et al., 2016 and we will incorporate new results from this field to our simulations, such as Q_d as a function of ρ_g and $V_{\rm rel}$.

It is more likely that NSDs may reside in low mass galactic nuclei (with $M_{\rm SMBH} \simeq 10^6 M_\odot$). We assumed long-lived ADs (several hundred Myr) but in reality, the AD may be short-lived and the NSD would not form completely within the lifetime of the AD. The observational estimates of AGN lifetime give wide range of values. For example, the AGN fraction in SDSS data implies long lifetimes of $t_{\rm AGN} > 10^8$yr (Miller et al., 2003), but Schawinski et al. (2015) argue that the SMBH growth period consists of many short episodes of activity with $t_{AGN} \simeq 10^5$yr. The estimates based on the effects of quasar proximity on the surrounding gas (studying the absorption lines) yield the AGN lifetimes of order of $10^6 - 10^7$ years (e.g. Schirber, Miralda-Escudé, and McDonald, 2004; Syphers and Shull, 2014; Segers et al., 2017, and references therein). It is likely that an NSD forms even in the case of a short active phase, if AGN activity repeats and a gaseous disc forms in the same orientation in each such short episode (Schawinski et al., 2015). Our results show that for shorter disc lifetimes (see Fig. 4.12) we will get a NSD, consisting of smaller mass. We find that after around 10^9 years a stationary state is established, if the disc lives that long.

If the AD disappears when the NSD is already formed then the latter will survive for a fraction of relaxation time. Although the orbital orientations of stars in NSD may be randomised by resonant relaxation (e.g. Hopman and Alexander, 2006), this mechanism was proposed to explain random orbital orientations of the Galactic Centre S-stars (e.g. Perets et al., 2009; Antonini and Merritt, 2013). But whether the resonant relaxation is really dominant in real systems, with mass spectrum, small deviations from spherical symmetry (like our disc potential) are highly controversial.

Miralda-Escudé and Kollmeier (2005) argue that stars captured by the accretion disc are eventually destroyed and their matter diffused within the AD. This might happen in the very inner region of the galactic nucleus where contact stellar collisions play important role, but our simulations do not resolve to that extent and the NSD forms further outside. The evolved and more massive stars have lower surface densities and their interaction with the AD can strip outer layers of the crossing star resulting in shallower stellar density profile (Amaro-Seoane and Chen, 2014; Kieffer and Bogdanović, 2016).

The star–disc interactions in AGN with a stellar mass spectrum and stellar evolution are planned to be examined in future work. In particular, formation, evolution and subsequent merging of binary black holes in the gaseous disc are of great interest. While residing in the AD, black holes can accrete material and merge with masses comparable to those detected by LIGO (Abbott et al., 2016). Bartos et al., 2017 and McKernan et al., 2017 used semi-analytic approaches to calculate the detection rate of such events by LIGO, but their estimates span three orders of magnitude (McKernan et al., 2017). Haggard et al. (2010) found that $0.16\% \pm 0.06\%$ of all galaxies in the local universe are active (some nearby active galaxies are NGC4051 at $\simeq 10$ Mpc and NGC4151 at $\simeq 14$ Mpc; Bentz and Katz 2015), implying a very large number of AGN ADs within the LIGO sensitivity volume. High resolution direct N-body simulations including realistic physics of gaseous ADs may set much better constrains on this problem. Exploring effects of stellar crossing on the gaseous disc requires detailed SPH or hydrodynamical simulations of the AD including all relevant physics. The fully realistic direct N-body simulation of AGNs remains as our long-term goal.

Chapter 5

A million–body simulation of the Galactic centre

The results presented in this chapter are published in the peer-reviewed article Panamarev, Taras; Just, Andreas; Spurzem, Rainer; Berczik, Peter; Wang, Long; Arca Sedda, Manuel "Direct N-body simulation of the Galactic centre", Monthly Notices of the Royal Astronomical Society, Volume 484, Issue 3, p.3279-3290. T. Panamarev improved the code to include relevant physics,performed the simulation, analyzed the output data and wrote the text. The co-authors contributed by comments, ideas, discussion with the referee, support with the code development and supervision.

5.1 Method

We model the NSC of the MW galaxy using the direct N-body fully parallel code NBODY6++GPU (Wang et al., 2015). The code is a multi-node massively parallel extension of NBODY6 (Aarseth, 2003) and NBODY6GPU (Nitadori and Aarseth, 2012) and also features accurate treatment of binary stars and close encounters using the algorithm developed by Kustaanheimo and Stiefel, 1965 and the chain regularization (Mikkola and Aarseth, 1993). We refer to Wang et al. (2015) for a detailed description of the numerical features and differences with NBODY6/NBODY6GPU.

We approximate the NSC with $N \simeq 10^6$ particles. Although this is the largest number of particles ever used in the direct N-body modelling of the GC so far, the real number of stars in the MW NSC is up to two orders higher. The simulation takes into account stellar evolution as well as the formation and evolution of binary stars. We start the simulation after gas removal and after the onset of virial equilibrium. Moreover, we include in our model a population of initial binaries, being 5% of the total particles number. Our choice is compatible with observational evidences suggesting that globular clusters dense cores are expected to host a low fraction of binaries (Bellazzini et al., 2002). As shown by Ivanova et al., 2005 via numerical models, even assuming a 100% fraction of initial binaries, a typical globular cluster would retain only 5-10 per cent of them at present-day. In NSCs, this fraction can be even lower, due to the higher velocity dispersion that tend to enhance binary disruption via close encounters (e.g. Hopman, 2009). Many of the initial binaries are wide and destroyed in the first few dynamical times by few-body interactions. From Sec. 5.4 and Fig. 5.9 we conclude that the binary fraction of 5% on average is quite stable with time; therefore we think that choosing initial binary fractions larger or even much larger than 5% will not significantly affect the results for the long term evolution.

The SMBH is included as an external point-mass potential with initial mass of 10% of the total stellar mass of the system (given the initial NSC mass of $4.0 \times$

$10^7 M_\odot$). The SMBH can grow via stars accretion if a star's orbit intersect the region encompassed by the accretion radius, $r_{\rm acc}$. In our model, we assume $r_{\rm acc} = 4.2 \times 10^{-4}$ pc $= 10^3 R_S$, being R_S the SMBH's Schwarzschild radius. In the case of an SMBH with mass $M_{\rm SMBH} = 4.3 \times 10^6$ M$_\odot$, a Sun-like star undergoes disruption at a distance larger than the Schwarzschild radius, and it can appear observationally as a TDE. Compact remnants (WDs, BHs and NSs) disruption radius falls inside R_S and their accretion onto the SMBH is likely not associated to any electromagnetic counterpart. On the other hand, compact remnants can tightly bind to the SMBH and undergo slow inspiral through low-frequency GWs emission. These so-called EMRIs represent a class of promising sources to be detected with space-borne detectors like LISA (e.g. Amaro-Seoane et al., 2007), or TianQin (Luo et al., 2016a). We note that due to the limit of resolution in the number of particles we increase r_t for all stars so that it equals to $r_{\rm acc}$[1]. In this simulation we analyse number counts for extreme mass ratio inspirals (accretion of compact objects onto the SMBH) as well as the TDEs by scaling r_t and the number of events to real values as shown in Sec. 5.3.1.

5.1.1 Initial conditions

To initialise our model, we construct a Plummer, 1911 equilibrium model immersed in a point-mass external potential (see McMillan and Dehnen 2007), assuming $N = 950k$ single stars and $N_b = 50k$ binary stars. The point-mass potential represents the SMBH which is fixed at the origin. We let the Plummer model adjust to the presence of the central potential and we start the modelling after this adjustment. Since this paper focuses on the inner part of the NSC, the effects from bulge, Galactic disc and dark matter halo are ignored.

We assumed a Kroupa, 2001 initial mass function, selecting masses in the range $0.08 - 100\ M_\odot$. The initial binaries are paired with mass ratios $f(q) \propto q^{-0.4}$ motivated by observed values of the Scorpios OB2 association (Kouwenhoven et al., 2007), log-uniform distribution in semi-major axis with minimum and maximum values of 0.005 and 50 astronomical units[2] (AU) and thermal eccentricity distribution: $f(e) = 2e$.

Single and binary stars are evolved using the stellar evolution packages SSE (Hurley, Pols, and Tout, 2000) and BSE (Hurley, Pols, and Tout, 2002). We assume that NSs at formation are subjected to a natal kick, whose amplitude is drawn according to a Maxwellian distribution with 1D velocity dispersion of $\sigma = 265\,{\rm km\,s^{-1}}$ (Hobbs et al., 2005). For BHs, the kick is calculated following the *fallback prescription* (see Belczynski, Kalogera, and Bulik 2002 for further details). The population of WDs, instead, is assumed to receive no kick at formation. The initial parameters are chosen to be as close as possible to those of the DRAGON simulations (Wang et al., 2016).

The star formation in the MW NSC is still ongoing and has complex history (see e.g. Mapelli and Gualandris 2016 for a recent review), but for simplicity we represent the NSC by a single stellar population of solar metallicity stars.

[1]Note that the scheme we adopt for modelling stellar accretion leads the SMBH to consume more stars than in reality.

[2]Since we want to cover the full possible range of binary parameters, some of them are overlapping at the initial moment. But they are merged at the next time-step, their number is very small and they do not affect the results discussed in this paper.

5.1.2 Scaling

In order to convert the original scale-free simulation of 10^6 particles in N-body units to the real system in physical units, we assume the MW NSC mass to be $M_{\rm NSC} = 4.0 \times 10^7 M_\odot = 10 M_{\rm SMBH}$. The Kroupa, 2001 initial mass function gives the simulated mass of $M_{\rm tot} = 6.18 \times 10^5 M_\odot$, thus one particle in the simulation represents a group of 65 stars. Therefore, stellar number counts are multiplied by 65 to be converted into real values.

For the radial scaling, we measure the influence radius of the SMBH at $t = 0$ to be 0.66 N-body units and equate it to the value of the influence radius for the MW which is calculated using the central velocity dispersion taken from Gültekin et al., 2009, $r_{\rm inf} = G M_{\rm SMBH}/\sigma^2 = 1.4$ pc. Assuming that half-mass radius $r_{\rm hm} = 3 r_{\rm inf}$, we can calculate the half-mass relaxation time (Spitzer, 1987)

$$t_{\rm rel} = \frac{0.14 N}{\ln(0.4N)} \left(\frac{r_{\rm hm}^3}{G M_{\rm tot}} \right)^{1/2} \tag{5.1}$$

for the MW NSC in physical units ($\simeq$ 11 Gyr) and for the model in N-body units and scale the time accordingly. By equating the relaxation time of the model with the relaxation time of the real system we can set the stellar evolution time in correspondence with the dynamical time of the system by

$$\frac{t'_{\rm rel}}{t'_{\rm stev}} = \frac{t_{\rm rel}}{t_{\rm stev}}, \tag{5.2}$$

where the prime denotes the modelled system and $t_{\rm stev}$ can be any stellar evolution time-scale.

The simulation was evolved up to 5.5 Gyr, which corresponds to a half of the initial half-mass relaxation time, but covers a few relaxation times inside the influence radius of the SMBH.

All values discussed below in the paper (densities, number counts, etc.) are given in physical units (except stated otherwise) for the *realistic* MW NSC.

5.2 General evolution of the system

Throughout the simulation, the NSC lost roughly half of its initial mass mostly owing to stellar evolution with small contribution from the accretion of stars onto the SMBH (see Sec.5.3). The final mass of the NSC is consistent with its present-day mass inferred from observations (Schödel et al., 2014).

The NSC overall evolution can be monitored through the time evolution of the Lagrangian radii, which are the radii containing a certain fraction of the total stellar mass. As seen in Fig. 5.1, the stellar system experiences an initial adjustment to the SMBH potential, explained by the fact that the binaries are not taken into account for the generation of initial conditions. Also, there is a strong mass-loss rate during the first tens of Myr. Overall, the expansion of the NSC is driven by the stellar evolution mass-loss (the magenta line in Fig. 5.1 clearly shows the expansion), but the Galactic bulge would keep the outer Lagrange radii at roughly a constant value. The small expansion of the inner Lagrange radius (0.1%) is driven by the accretion of stars onto the SMBH.

The time evolution of the average stellar mass, in Lagrangian shells, reveals mass segregation, as shown in Fig. 5.2. After all the heavy stars lost most of their mass ($\sim$

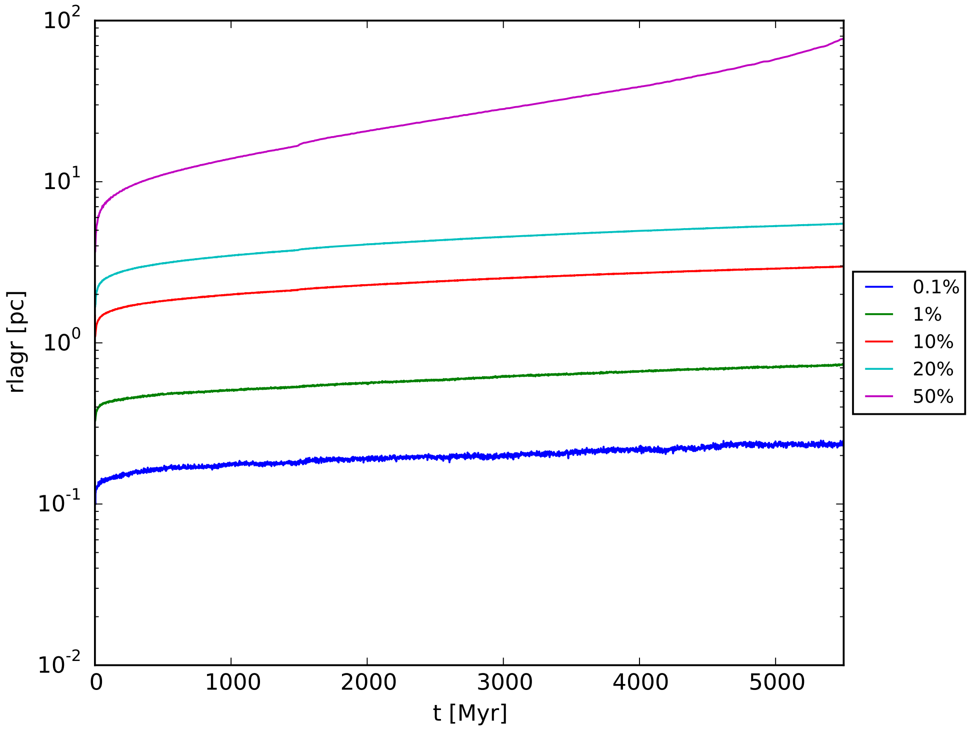

FIGURE 5.1: Evolution of the Lagrangian radii of the NSC. Blue dotted line shows the time evolution of 50% Lagrange radius, while dashed green, dash-dotted red, dotted cyan and solid magenta lines correspond to 20, 10, 1 and 0.1% respectively.

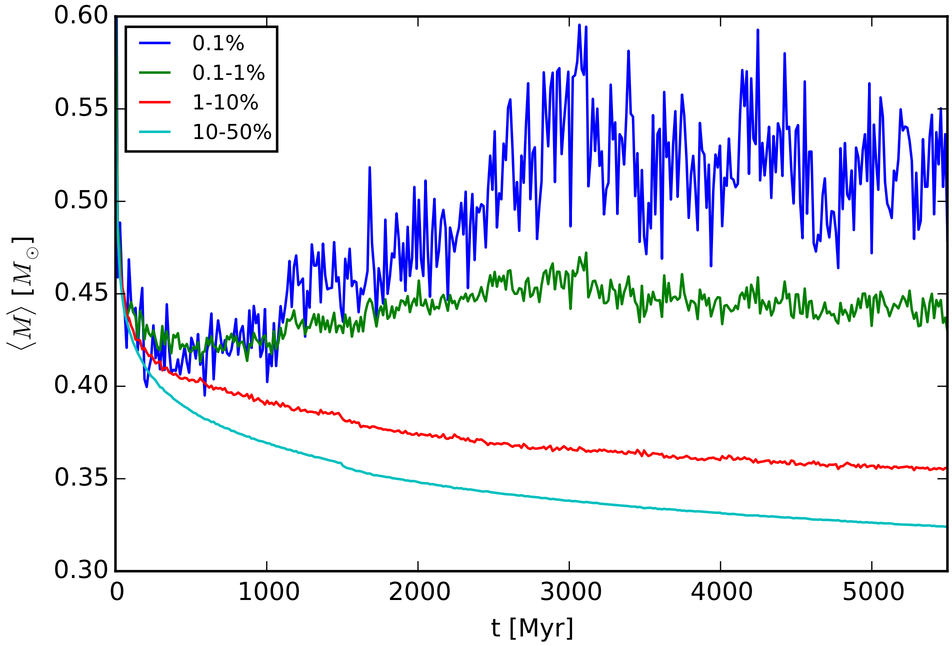

FIGURE 5.2: Time-evolution of the average stellar mass between shells of Lagrangian radii. Solid blue line corresponds to the evolution of average stellar mass in the region where Lagrangian radius is less than 0.1%, thick green line shows the average mass between 0.1 and 1%, red and cyan lines represent masses between 1 - 10% and 10 - 50% respectively. Two upper curves indicate mass segregation.

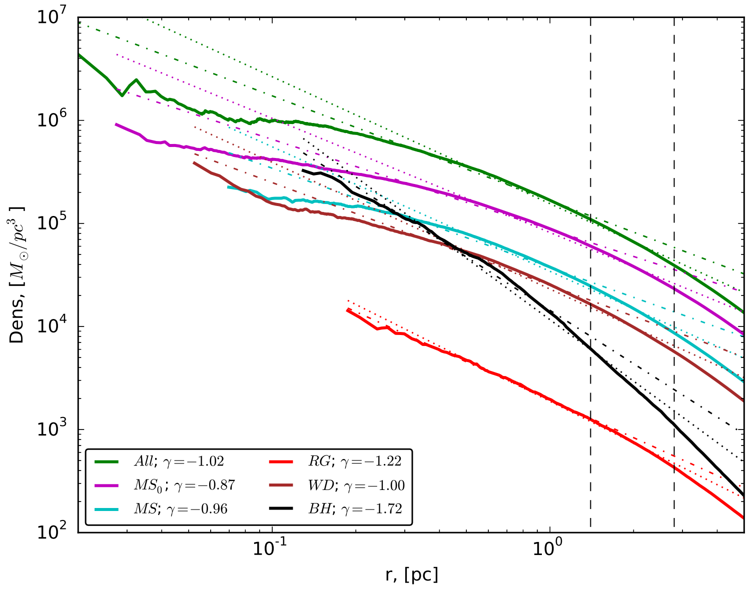

FIGURE 5.3: Stellar density profiles at $t = 5$ Gyr for different stellar types. Thick solid lines correspond to: All - all stars, $\mathrm{MS_{low}}$ - low mass main sequence stars, MS - main sequence, RG - red giants, WD - white dwarfs, BH - black holes. Corresponding power-law slopes fitted inside the initial and final influence radii of the SMBH are shown as dash-dotted and dotted lines of the same colour. The dashed vertical lines denote the initial influence radius ($r = 1.4$ pc) and the influence radius at $t = 5$ Gyr ($r \sim 2.8$ pc) of the SMBH. The power-law indices fitted inside $r = 1.4$ pc are shown in the legend.

300 Myr), the mass segregation overtakes the time evolution of the average masses in Lagrangian shells. After ~ 3 Gyr of evolution, a quasi-steady state is established for the innermost regions. The total number of stars in terms of different stellar evolution components[3] and their properties are described in subsequent sections and summarized in Table 5.1.

5.2.1 Density profiles

Typically the 3D stellar density (as well as the surface density) is described by a power law of the form $\rho(r) \propto r^{\gamma}$, where r is the distance from the SMBH. For the case of equal mass solar type stars the slope becomes $\gamma = -1.75$ inside the influence radius of the SMBH (Bahcall and Wolf, 1976). For the case of a mass spectrum the dominant component obtains the -1.75 slope (Bahcall and Wolf, 1977).

In Fig. 5.3 we present 3D stellar density profiles for various stellar types. In order to get a better accuracy, we measured the density profile power-law slopes for 10 snapshots around $t = 5$ Gyr and averaged the results. Due to the low particle number in the inner part, we required at least 3 particles for the calculation of the density. Stellar mass BHs have the steepest slope of $\gamma = -1.72 \pm 0.04$ while the low mass and high mass main sequence (MS) stars are characterized by a shallower slope, being $\gamma = -0.87 \pm 0.01$ and $\gamma = -0.96 \pm 0.02$, respectively, calculated at 5 Gyr. The slopes are measured inside the SMBH influence radius. White dwarfs (WDs) have a similar slope ($\gamma = -1.00 \pm 0.02$), but red giants (RGs) are slightly steeper with $\gamma = -1.22 \pm 0.12$. Comparison with BAS2018 (see their Fig. 2) yields very similar slopes for the giants, although, for the upper and lower MS stars their simulations show steeper slopes. In principle, the results are consistent with each other since BAS2018 use slightly different definitions for lower and upper MS stars, and they show the results at $t = 13$ Gyr. Another point is that BAS2018 have exponentially declining star formation rate, they implement it by adding new stars every Gyr. The power law slope for the BHs is remarkably consistent with the analytical prediction of Bahcall and Wolf (1977) and with a recent study based on Fokker-Planck approach (Vasiliev, 2017). The cusp is already formed at $t < 2$ Gyr, less than one NSC half-mass relaxation time. However, as shown by Amaro-Seoane and Preto (2011), the cusp regrowth time is 1/4 of the relaxation time, thus our results are consistent with the assumed initial half-mass relaxation time.

Due to stellar mass-loss the influence radius of the SMBH expanded from 1.4 to 2.8 pc and we present the linear fitting for the density slopes for the region $r < 2.8$ pc as well (see columns 4-5 of Table 5.1). The power-law indices for the influence radius at 5 Gyr are more consistent with the strong mass segregation solution, but are still shallower than the values proposed by Alexander and Hopman, 2009 and Preto and Amaro-Seoane, 2010. They claimed that in the case when the number of lower mass objects (stars with masses up to $1M_{\odot}$) is much higher than that of heavy objects (stellar BHs with masses of $10M_{\odot}$) the heavy objects obtain a power-law density slope γ of -11/4 while the light ones have $\gamma = -3/2$. They parametrized the solution by $\Delta = N_h M_h^2/(N_l M_l^2)4/(3 + M_h/M_l)$, where N and M denote the numbers and masses of light and heavy objects. In our simulation the value of Δ approaches zero ($\Delta \sim 5 \times 10^{-8}$) meaning that we are in the strong mass segregation regime, although the density slopes in our simulation are shallower than predictions.

[3]The stellar types are defined as in Hurley, Pols, and Tout, 2000, but for simplicity we combine different types of RGs in one stellar type.

As seen in Fig. 5.3, low-mass MS stars dominate at $r > 0.1$ pc and low-number statistics at smaller radii does not allow us to study the details of stellar density distribution there. We leave this analysis for future work.

5.2.2 Stellar mass black holes and other compact objects

Compact objects may play an important role in the evolution of the NSC. Fig. 5.4 shows the time evolution of compact objects divided by type: carbon-oxygen white dwarfs (COWD), oxygen-neon white dwarfs (ONeWD), NSs and BHs. After 5 Gyr, the population of COWDs is still growing due to stellar evolution, while the formation of ONeWDs already ceased after 100 Myr, although $\sim 1.4 \times 10^5$ ($\sim 1.3 \times 10^5$) of them are still retained at 2 (5) Gyr. While WDs represent still a noticeable population after 5 Gyr, almost all the NSs are ejected, due to the high natal kick received consequently to supernova explosions. We have to note that in a real galactic nucleus the NSs may be still bound to the system under the influence of the potential from the galactic bulge and dark matter halo, that becomes more important at the outer boundaries of the NSC. Fig. 5.5 shows the normalized distribution of velocities for the escaped NSs and BHs calculated at 100 pc. Assuming that the MW bulge potential is reasonably represented by a standard Plummer sphere $\Phi = -GM_{\rm tot}/\sqrt{r^2+b^2}$ with total mass $M_{\rm tot} = 2.0 \times 10^{10} M_\odot$ (Valenti et al., 2016) and the scale length $b = 350$ pc (Dauphole and Colin, 1995), we found that $\sim 60\%$ of escaped NSs have velocities lower than the bulge escape velocity calculated at 100 pc. This suggests that as many as 8×10^5 NSs might be still wandering in the galactic bulge, and possibly can come back to the NSC. For the stellar-mass BH population the situation is different in a way that their kick velocity depends on the fallback factor (Belczynski, Kalogera, and Bulik, 2002). This explains the initial peak in the number of stellar BHs (dash-dotted line of Fig. 5.4): more than half of them escaped but after that the number of BHs declines slowly and we expect $\sim 2.2 \times 10^4$ ($\sim 1.8 \times 10^4$) stellar-mass BHs after 2 (5) Gyr. The black line in Fig. 5.5 shows that $\simeq 95\%$ of all escaped BHs would be still bound to the system, increasing their total number.

Fig. 5.6 shows the number of stellar-mass BHs in the inner part of the NSC as a function of time. Since the BHs are the heaviest objects in the NSC, they experience the strongest mass segregation. The number of BHs in the inner 0.5 and 0.3 pc increased significantly over time. We expect ~ 2000 and ~ 1000 BHs inside central 0.5 and 0.3 pc respectively and ~ 6000 inside the initial influence radius of the SMBH (1.4 pc) at 5 Gyr. Having in mind Fig. 5.5, we note that the numbers of BHs above have to be treated as lower limits.

5.3 The supermassive black hole

Close stellar passages around the SMBH may result either in the star disruption, a phenomenon called TDE, or in its gravitational wave (GW) induced inspiral/plunge. In the latter case, the tight SMBH-star binary evolve mostly through GW emission, possibly resulting in a so-called extreme mass ratio inspiral (EMRI).

In this section, we try to quantify the amount of TDEs and EMRIs expected to form over the whole NSC lifetime.

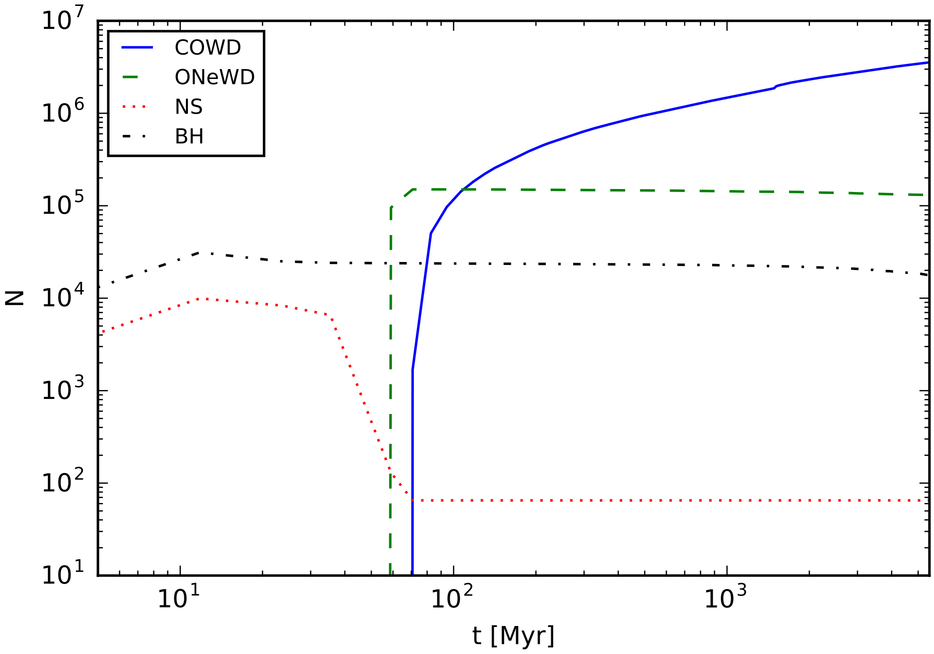

FIGURE 5.4: The number of compact objects as function of time. All lines show only the single stars. Solid blue and dashed green lines show WDs, dash-dotted black and dotted red lines show BHs and NSs respectively. High natal kicks remove most of the NSs from the system, while there are still more than 10^4 stellar BHs.

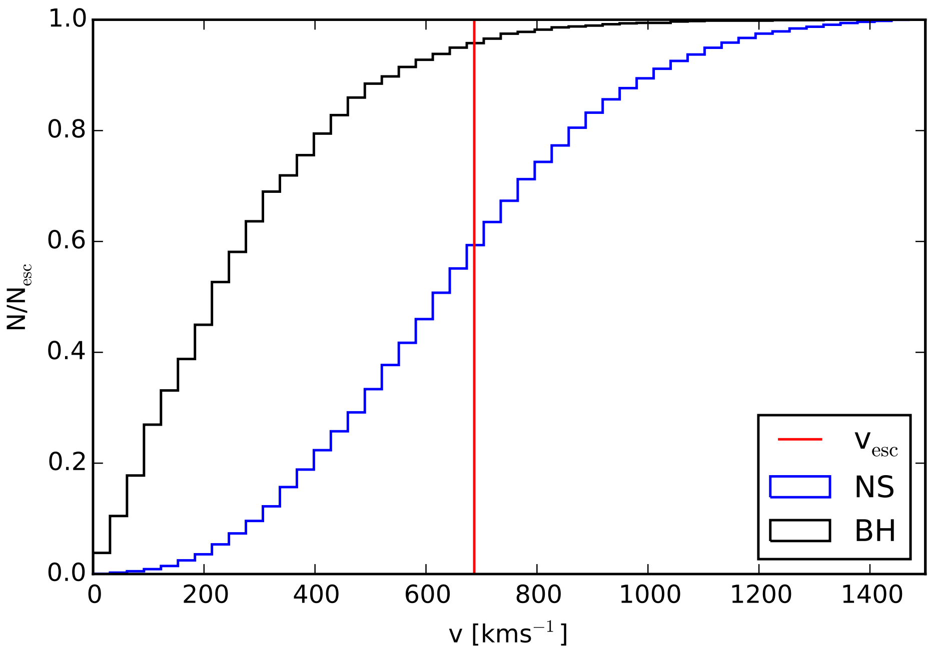

FIGURE 5.5: Cumulative normalized histogram showing velocities of the escaped NSs (blue) and BHs (black). The red vertical line represents the escape velocity for the MW bulge at 100 pc.

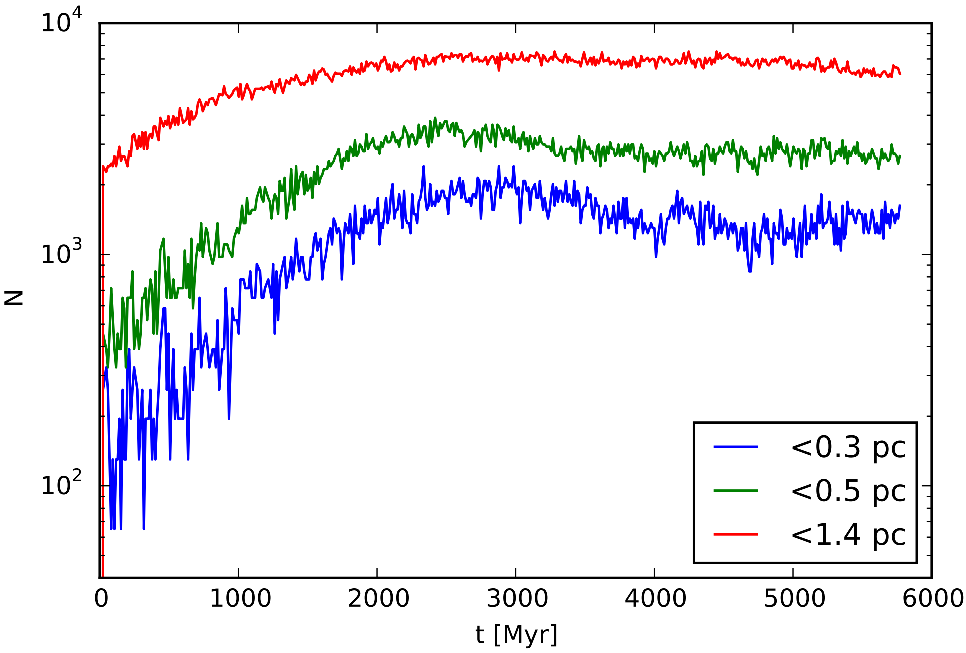

FIGURE 5.6: The number of BHs as function of time. The red, green and blue line show the number of stellar mass BHs inside 1.4, 0.5 and 0.3 pc respectively.

TABLE 5.1: Properties of different stellar types at $t = 5\,\mathrm{Gyr}$.

Stellar type	N_{tot}	$<m>$ ($M_\odot$)	$\gamma(r < 1.4\mathrm{pc})$	$\gamma(r < 2.8\mathrm{pc})$	$<r_t>$ pc	$\dot{N}_{\mathrm{acc}}$ (Gyr^{-1})
Low-mass main sequence	5.0×10^7	0.25	-0.87 ± 0.01	-1.11 ± 0.03	1.5×10^{-6}	3278
Main sequence	4.3×10^6	0.92	-0.96 ± 0.02	-1.21 ± 0.05	4.0×10^{-6}	658
Red giant	1.5×10^5	1.24	-1.22 ± 0.12	-1.34 ± 0.15	4.9×10^{-5}	39
White dwarf	1.6×10^6	0.71	-1.00 ± 0.02	-1.23 ± 0.03	1.6×10^{-6}	255
Black hole	1.8×10^4	10.05	-1.72 ± 0.04	-1.98 ± 0.07	1.6×10^{-6}	4
All stars	5.8×10^7	0.33	-1.02 ± 0.02	-1.23 ± 0.03	-	4120

Notes. Column 1 is the name of the stellar type, columns 2 and 3 show the total number of stars at 5 Gyr and the average stellar mass in solar masses, columns 4 and 5 represent the 3D density power-law indices inside 1.4 and 2.8 pc respectively, column 6 shows the average tidal disruption radius that was used in Eq. 5.5 (for compact objects we used the value of $4R_{\mathrm{S}}$ as described in Sec. 5.3.2), column 7 gives the number accretion rate per Gyr derived over the period of 5 Gyr and column 8 shows the EMRI rate per Gyr for BHs and WDs. Numbers in columns 7 and 8 are rescaled using Eq. 5.5.

5.3.1 Tidal disruption events

A star with mass m_* and radius r_* can get tidally disrupted if the SMBH tidal forces overcome the star self-gravity. The resulting stellar debris distribute in a disc, feeding the SMBH while emitting X-ray radiation, giving rise to an observable phenomenon called TDE (Hills, 1975; Frank and Rees, 1976). Equating the gradients of these two competing forces allows us to calculate the tidal disruption radius, which is given by

$$r_{\rm t} \simeq r_* \left(\frac{M_{\rm SMBH}}{m_*}\right)^{1/3}. \tag{5.3}$$

In our model, we assumed that a star passing sufficiently close to the SMBH is completely accreted, without any mass left. Since the number of particles used to model the NSC is 65 times smaller than in the real NSC, the number of possible TDEs is limited by low-resolution in the SMBH vicinity. To deal with this problem, we initially set a large tidal radius, $r_t = 4.2 \times 10^{-4}$ pc (the same for all objects), scaling down *a posteriori* to the actual r_t (computed using stellar radius and mass at the moment of accretion) values. In particular, we scale the number of events using the relation obtained from loss-cone theory, according to which the number of stars accreted through tidal disruption depend on the stellar tidal radius and the total number of stars in the system,

$$N_{\rm acc} \propto r_t^{4/9} \times (N/\ln(0.4N))^{4/9} \tag{5.4}$$

(Baumgardt, Makino, and Ebisuzaki, 2004a; Kennedy et al., 2016). Therefore, the number of accreted stars in the real system can be estimated using the above scaling relation

$$N_{\rm acc}^{\rm real} = \left(\frac{r_t^{\rm real}}{r_t^{\rm sim}}\right)^{4/9} \times \left(\frac{N_{\rm real}}{N_{\rm sim}}\right)^{4/9} \left(\frac{1}{\ln(0.4N_{\rm real}/N_{\rm sim})}\right)^{4/9} \times N_{\rm acc}^{\rm sim}. \tag{5.5}$$

For each of the 5 star groups summarized in Table 5.1, we calculated the corresponding average tidal radius through Eq. 5.3 using the values for stellar mass and radius at the moment of accretion (see column 7 of Table 5.1), and the number of stars passing closer than r_t in our simulation, namely $N_{\rm acc}^{\rm sim}$. This quantity is then used in Eq. 5.5 to scale our results to the real NSC.

Table 5.1 (columns 7 and 8) lists the number of tidally disrupted (or accreted) stars per Gyr derived from the total number in 5 Gyr (scaled using Eq.5.5). The majority of TDEs are due to low-mass MS stars, while the SMBH growth is mostly due to MS stars. As shown in Fig. 5.7, the time evolution of the accreted mass saturates to a nearly constant value in 2.8 Gyr, allowing us to provide an upper limit to the SMBH accreted mass by 5 Gyr as $\Delta M_{\rm SMBH} \simeq 10^4 M_\odot$ or $\simeq 0.23\%$ of the initial SMBH mass. This implies a mass accretion rate $\dot{M} = 2.0 \times 10^{-6} M_\odot {\rm yr}^{-1}$ and a TDE rate $\dot{N}_{\rm TDE} \simeq 4.1 \times 10^{-6}$ yr^{-1} which is consistent with the observed number of TDEs obtained per MW-like galaxy (Stone and Metzger, 2016). We note that due to the initial loss-cone depletion the accretion rate is higher in the beginning and is smaller at later stages of evolution.

As stated above, we assume that a star undergoing a TDE in our model is completely disrupted and 100% of its mass is added to the SMBH. However, the tidal disruption radius for a RG is large while its typical density is generally low, thus a close encounter with the SMBH may lead to an envelope stripping (MacLeod, Guillochon, and Ramirez-Ruiz, 2012; Bogdanović, Cheng, and Amaro-Seoane, 2014) and the core will remain with the structure similar to a WD (e.g. Althaus and Benvenuto

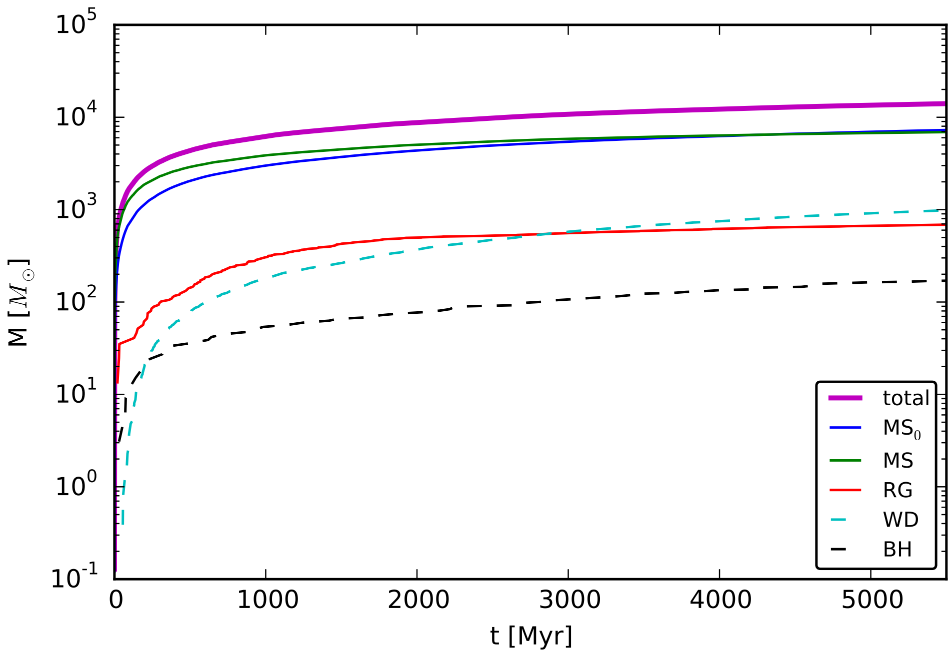

FIGURE 5.7: Growth of the SMBH. The thick magenta line represents the total accreted mass onto the SMBH, other lines the contributions from low mass MS stars (blue), MS stars (green), RGs (red), WDs (cyan) and BHs (black). The accreted mass is calculated using Eq. 5.5

.

1997). These WDs are very hot ($\sim 10^5 K$) and may be observable. Fig. 5.8 shows possible locations of these objects, the radii at which the RGs were stripped (column 7 of Table 5.1 gives numbers of such events), but we do not follow the dynamics of the survived core after the disruption. The detection of the survived cores in the GC may give constrains on the number of giant disruptions. The remnant WDs may also increase the fraction of EMRIs (see next subsection), but these effects will be explored in future work.

5.3.2 Gravitational waves

In general, compact objects (WDs, NSs or BHs) can survive tidal disruption due to their compact sizes and can lead to the formation of an EMRI, a tight binary emitting GWs in the LISA (e.g. Amaro-Seoane et al., 2007) and TianQin (Luo et al., 2016a) expected observational bands. In our models, we consider the accretion of a compact object if it gets inside the last parabolic stable orbit, $4R_S$ (Amaro-Seoane et al., 2007; Amaro-Seoane, Sopuerta, and Freitag, 2013). Objects scattering directly into the $4R_S$ are direct plunges, they emit a burst of gravitational radiation, but are difficult to detect even for the GC since they do not spend much time in the LISA band. The number of direct plunges can be calculated using the loss-cone theory, applying the same procedure as in previous subsection. Column 7 of Table 5.1 lists the numbers for WDs and BHs which we classify as direct plunges. The subclass of these objects would 'plunge' into to the region between $1R_S$ and $4R_S$, we call them *semi-plunges*. The semi-plunges may still make a couple of orbits (depending on the spin of the SMBH) and produce very different gravitational wave signal, but it is still difficult

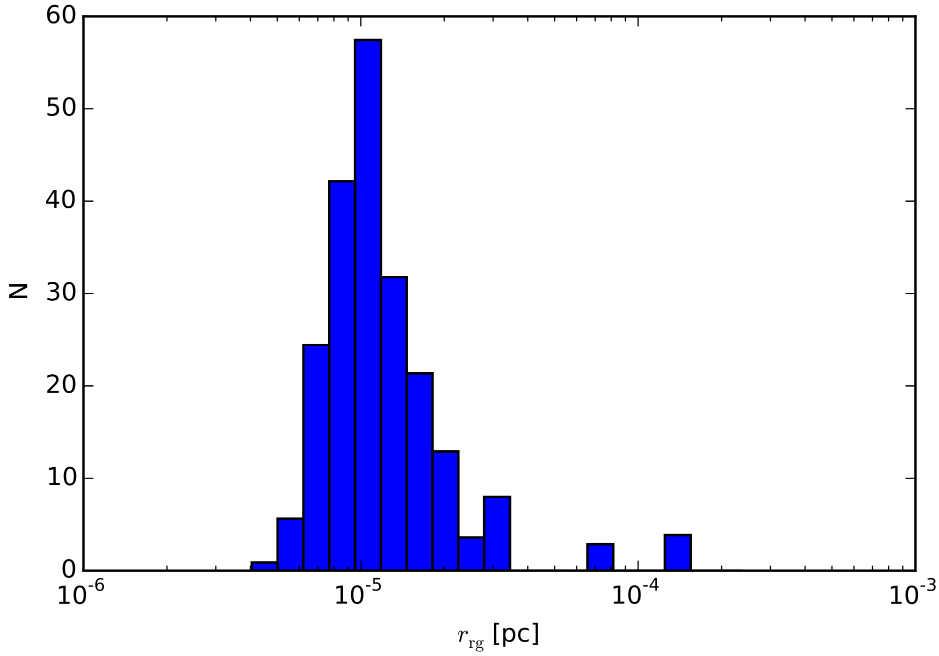

FIGURE 5.8: Histogram of the locations where the red giants were stripped by the SMBH.

to detect them. We find the rate of semi-plunges to be 2 (117) for BHs (WDs) per Gyr. The electromagnetic counterpart will also be different for plunges and semi-plunges for the case of inspiralling WDs or NSs (see e.g. Belczynski et al. 2018 where the authors study double NS mergers).

On another hand, EMRIs evolution is a process that the compact object undergoes a large number of close encounters with the SMBH (Alexander and Hopman, 2003; Amaro-Seoane et al., 2007) that causes energy loss due to gravitational wave emission and, thus, may be detectable by LISA. To verify that its orbit is not affected by two-body relaxation, Amaro-Seoane et al., 2007 define a critical semi-major axis below which GW emission dominates orbital evolution as:

$$a_{\rm EMRI} = 5.3 \times 10^{-2}{\rm pc} \times C_{\rm EMRI}^{2/3} \left(\frac{t_{\rm rc}}{Gyr}\right)^{2/3} \left(\frac{m}{10 M_{\odot}}\right)^{2/3} \left(\frac{M_{\rm SMBH}}{10^{6} M_{\odot}}\right)^{-1/3} \tag{5.6}$$

where $C_{\rm EMRI} \simeq 1$ and $t_{\rm rc}$ is the local relaxation time. The latter is given by (Spitzer, 1987; Binney and Tremaine, 2008b):

$$t_{\rm rc} = \frac{18{\rm Gyr}}{\ln \Lambda} \frac{1 M_{\odot}}{m_{\rm bh}} \frac{10^{3} M_{\odot}{\rm pc}^{-3}}{\rho(r)} \left(\frac{\sigma(r)}{10{\rm km/s}}\right)^{3}, \tag{5.7}$$

where $\ln \Lambda$ is Coulomb logarithm, $m_{\rm bh}$ is the mass of a stellar BH, ρ and σ are the stellar density and 1D velocity dispersion respectively. Assuming $\ln \Lambda \simeq 10$, $\sigma = \sqrt{G M_{\rm SMBH}/3r}$, measuring the BH mass to be $m_{\rm bh}$= 10 $M_{\odot}$ and the density of stellar BHs $\rho = 4 \times 10^{4}\ M_{\odot}{\rm pc}^{-3}$ (see Fig. 5.4), we get $t_{\rm rc} \simeq 6.2$ Gyr at $r = 0.5$ pc. Thus, for a typical BH in our simulation with $m = 10\ M_{\odot}$, the critical semi-major axis equals to $a_{\rm EMRI} = 0.11$ pc. The late evolution of an EMRI is determined by GW emission, leading eventually to the SMBH - compact remnant coalescence over the merging time due to the gravitational radiation given by (Peters, 1964)

$$t_{\rm GW} \approx \frac{768}{425}\frac{5}{256}\frac{c^5}{G^3}\frac{a^4}{m_1 m_2(m_1+m_2)}\left(1-e^2\right)^{7/2} \tag{5.8}$$

(here we use an approximation where $e \sim 1$). If we take the eccentricity to be $e = 0.9999$, then for a BH with typical mass $m = 10\ M_\odot$ and the critical semi-major axis $a = 0.11$ pc orbiting the SMBH of $4.3 \times 10^6 M_\odot$ the merging time equals 94 Myr which is much shorter than the relaxation time. The chosen eccentricity corresponds to the pericentre distance $r_{\rm peri} \simeq 27R_{\rm S}$. Thus, we define the criterion for an EMRI as:

$$\begin{aligned} a &< a_{\rm EMRI}; \\ 4R_{\rm S} < r_{\rm peri} &< 27R_{\rm S} \end{aligned} \tag{5.9}$$

Now we can use the classical loss-cone theory to calculate the number of EMRIs. First, we obtain amount of 'loss-cone' orbits with $r_{\rm peri} < 4R_{\rm S}$ then with $r_{\rm peri} < 27R_{\rm S}$ and take the difference between former and latter, finally we exclude the objects with $a > a_{\rm EMRI}$. The same procedure can be applied to calculate number of EMRIs originating from a WD - SMBH binary coalescence. In this case $a_{\rm EMRI} = 0.02$ pc and $r_{\rm peri} \simeq 5R_{\rm S}$ (we used mean mass of accreted WD from our simulation $m_{\rm WD}$= $0.7M_\odot$). The last column of Table 5.1 provides the EMRI rates of compact objects in our simulation. Our results suggest that $\simeq$ 2 WDs and $\simeq$ 2 BHs are expected to undergo an EMRI over each Gyr. The derived EMRI rates are lower than the previous estimations (e.g. Arca-Sedda and Gualandris, 2018), likely due to the low fraction of retained NSs and BHs in our model. We can conclude that WDs are the main sources of direct plunges in the GC with a minimum rate of more than 250 events per Gyr, we found few BHs and no NS.

We note that here we do not follow the accreted object after it is gone inside $4R_{\rm S}$ or classified as an EMRI.

5.4 Binaries

Although the GC environment is very extreme, some binaries have been detected there (Muno et al., 2005a; Pfuhl et al., 2014). In this section we analyse the number of GC binaries obtained from our simulation. The upper curve in Fig. 5.9 shows the total number of binaries as function of time. We start the simulation with 5% of binaries and roughly half of them survive till $t = 5$ Gyr of evolution. The two lower curves in the same figure show the number of binaries inside 1 and 0.1 pc, respectively, meaning that after 5 Gyr we expect 100-1000 of them inside 0.1 pc and $\simeq 5.0 \times 10^4$ in the inner parsec. These binaries are characterized by an average total mass of 1.0 and $0.69M_\odot$ and a binary fraction of $\sim$ 2% and $\sim$ 2.5% respectively. The initial distribution of the binary semi-major axis (SMA) was assumed log-uniform between a = 0.005 and 50 AU. The SMA defines the binary binding energy ($E_b \propto 1/a$), and allows to determine whether a binary is 'hard' or 'soft' (Heggie, 1975). A sizeable number of 'soft' binaries are quickly destroyed because of the repeated interactions with the surrounding dense environment, leading to a strong decrease of the number of binary systems having initial SMA values larger than 1 AU (compare blue and green lines in Fig. 5.10).

On the other hand, the number of systems with smaller SMA increase in time, thus implying a growing number of 'hard' binaries. Fig. 5.10 compares the SMA

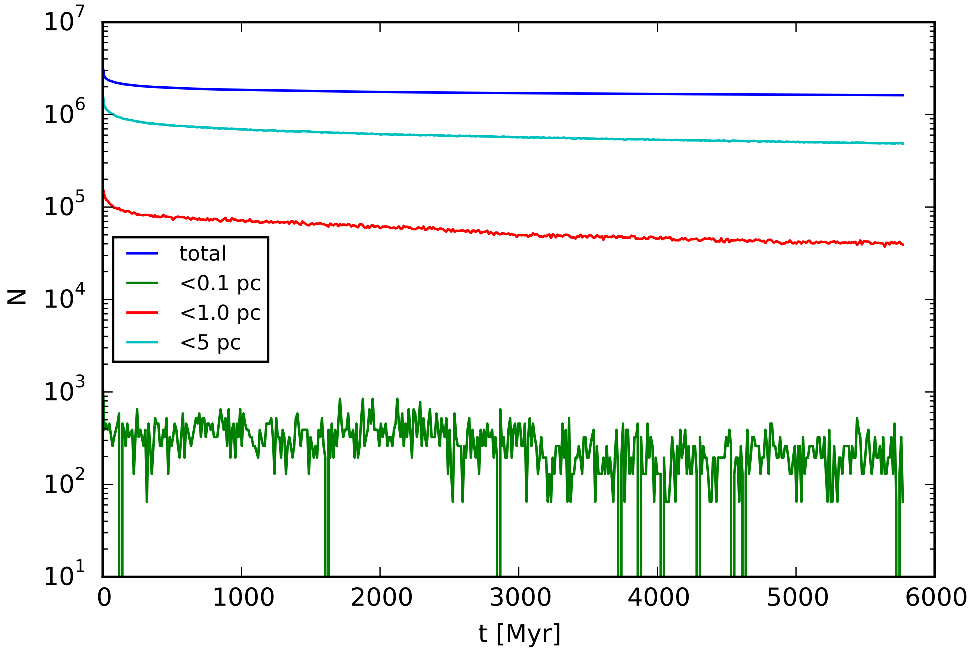

FIGURE 5.9: Number of binaries as function of time. The blue line shows the total number of binaries. Cyan, red and green lines show the number of binaries inside 0.1, 1 and 5 pc correspondingly.

distribution at a time t = 2 Gyr in our simulation (the peaked brown line) with the SMA distribution obtained evolving all the binaries in isolation. This comparison shows the effect of the dense environment on the binary stellar evolution. Thus, the systems with small separations are getting higher in number and their orbits shrink. As opposite to this, the standalone binary evolution code results show that the number of binary systems with smaller separations will decrease (some of them will merge and some of them will get wider orbits after the supernovae explosions). Step-filled histograms on Fig. 5.10 show that the low-separation binaries are dominated by low-mass MS stars and some WDs. Fig. 5.11 shows the distribution of the binding energies of the binaries and their distances to the SMBH at 100 Myr, 1 Gyr and 5 Gyr. As we can see, the number of binaries with binding energies below 10^{-8} N-body units decreases with time, especially in the central part.

The total mass of a binary system is typically twice larger than that of a single star, thus implying that most of the binaries will be subjected to mass segregation. While mass segregation brings the binaries to the centre, the soft ones are being destroyed and hard ones survive, but even a very hard binary can be tidally disrupted by the SMBH. Fig. 5.12 illustrates how the binary fraction changes with the distance from the SMBH for initial moment (blue curve), 100 Myr (green), 1 Gyr (red) and 5 Gyr (cyan). Initially, the binaries were distributed uniformly but already after 100 Myrs the central binary fraction ($r < 1$ pc) dropped from 5% to $\sim$ 2.5 %. Comparison of the red and cyan lines yields that the total number of binaries drops but in general the shape of the curve is established.

Our simulation suggests that the NSC contain a substantial number of WD binaries (Fig. 5.13). These binary systems are of particular interest since they can give rise to supernovae Ia events or, in some cases, they can even form a millisecond pulsar

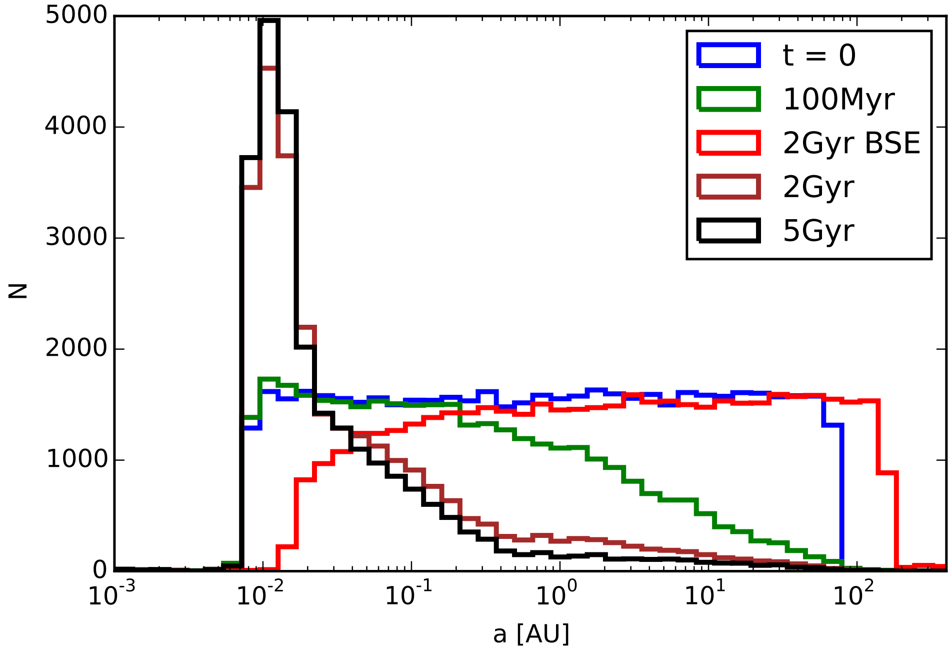

FIGURE 5.10: Semi-major axis of binaries (not rescaled). The blue line shows the initial distribution, green and black lines represent the semi-major axis at t = 100 Myr and t = 5 Gyr respectively. The red line displays the semi-major axis without dynamics (standalone binary stellar evolution (BSE) simulation). Grey and green step-filled histogram indicate the distribution of double low-mass MS binaries and stellar systems with WDs at 5 Gyr respectively.

(a) $t = 100$ Myr

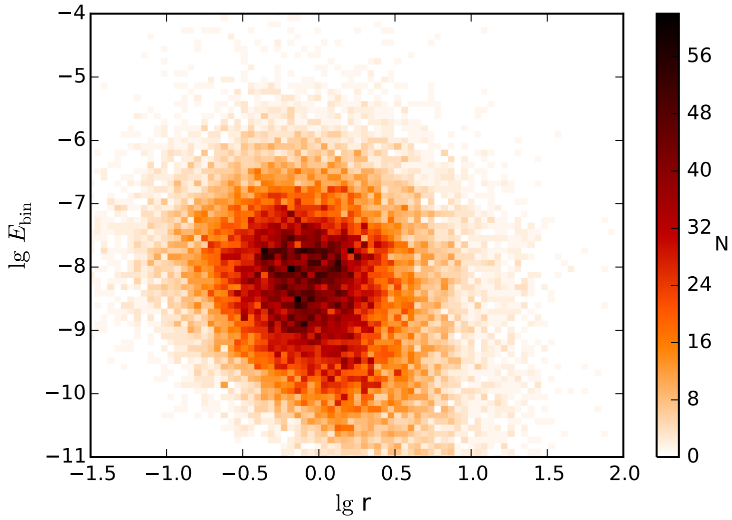

(b) $t = 1$ Gyr

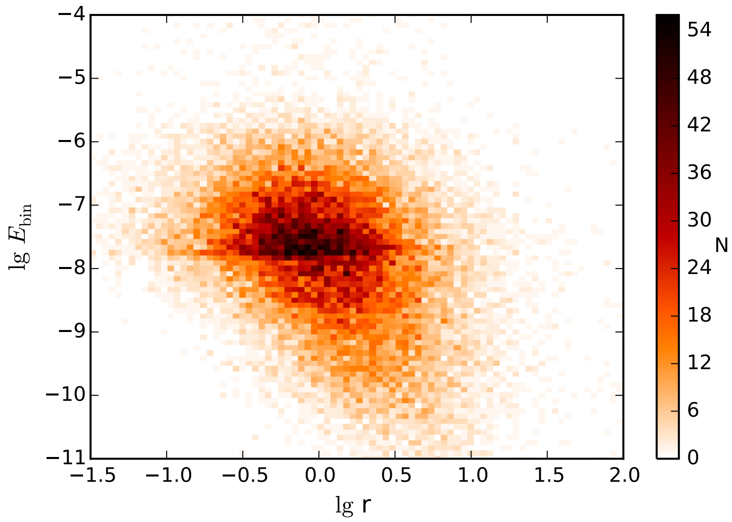

(c) $t = 5$ Gyr

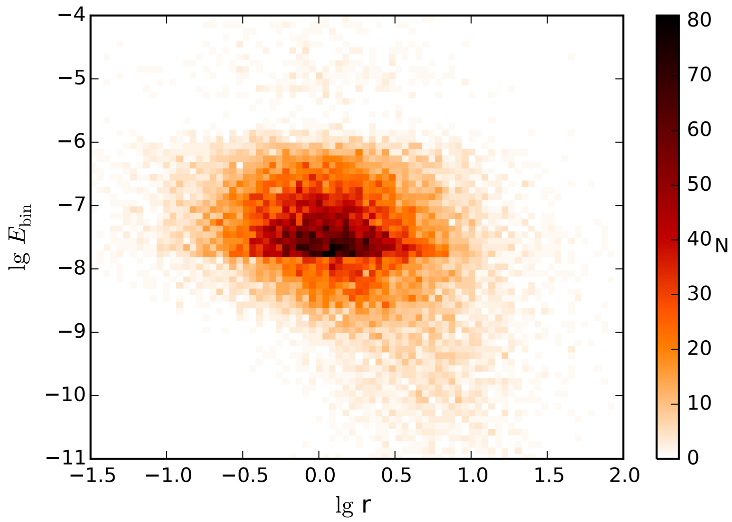

FIGURE 5.11: 2D histogram of binding energies of binaries versus their distances to the SMBH (all values are given in N-body units), colour-coding shows the number of binaries in each bin.

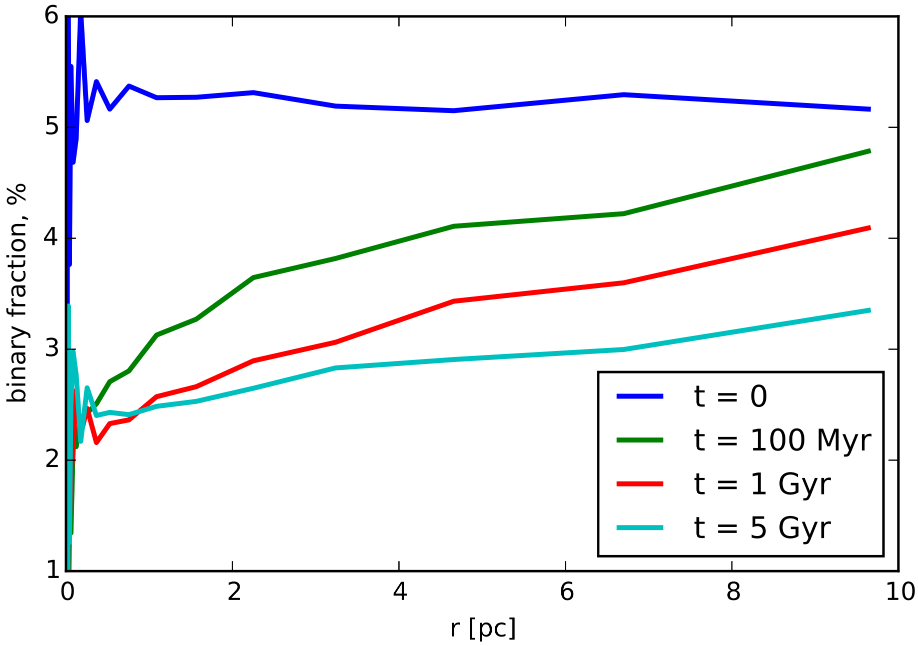

FIGURE 5.12: Binary fraction as a function of the distance from the SMBH. Blue line shows the initial dependence, green, red and cyan lines represent the binary fraction as a function of radius at 100 Myr, 1 Gyr and 5 Gyr respectively.

(MSP) through matter accretion from a companion star onto a highly spinning massive WD (Freire and Tauris, 2014). Double degenerate WD - WD binaries can be the progenitor of supernovae Ia explosions, provided that their total mass exceeds the Chandrasekhar limit (note that there are also sub and super Chandrasekhar models, see review by Maoz, Mannucci, and Nelemans 2014). On the other hand, binary systems containing a NS are almost absent in the system (Fig. 5.14). These types of binaries are possible progenitors of MSPs, which are thought to be recycled NSs spun up by matter accretion from a stellar companion, according to the standard scenario. After the natal kick the NS binaries become very wide (if they survive the supernova explosion) and eventually are ionized. We find that 1000 and $\approx$ 3000 of double and single degenerate pairs are expected to populate the central parsec of the MW galactic nucleus.

5.5 Summary and discussion

We performed a high resolution direct N-body simulation of the GC starting with $\sim 10^6$ particles with 5% of initial binaries taking into account single and binary stellar evolution. This is the largest simulation of this kind so far. We showed that the stellar component forms a cusp with the highest power-law index for the stellar mass BHs $\gamma \simeq -1.72$. Then we demonstrated how mass segregation occurs by analysing average masses between Lagrangian shells. When the stars happen to come very close to the SMBH they are disrupted with a total rate of $\sim 4 \times 10^3$ stars per Gyr. The number of accretion events for compact objects is $\sim$ 270 per Gyr with few of them being possible EMRIs. About half of the initial binaries survived until 5 Gyr of the evolution. Most of the binaries are destroyed due to dynamical interactions with

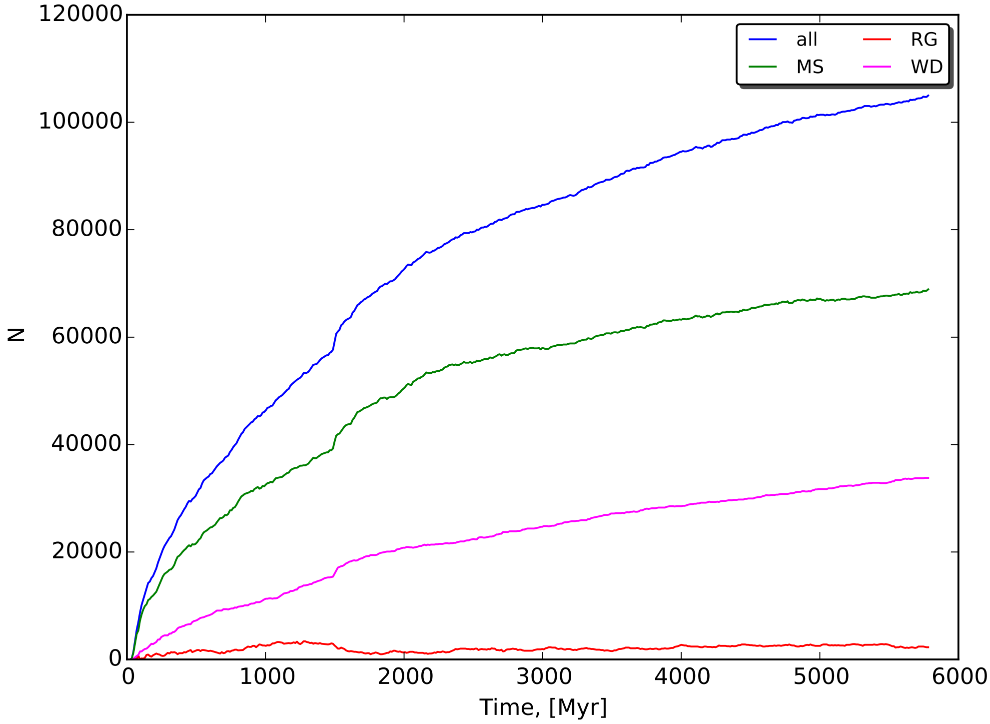

FIGURE 5.13: Number of WD binaries as a function of time. The blue line shows the total number of WD binaries, green and red lines are WD - MS star and WD - WD binaries correspondingly.

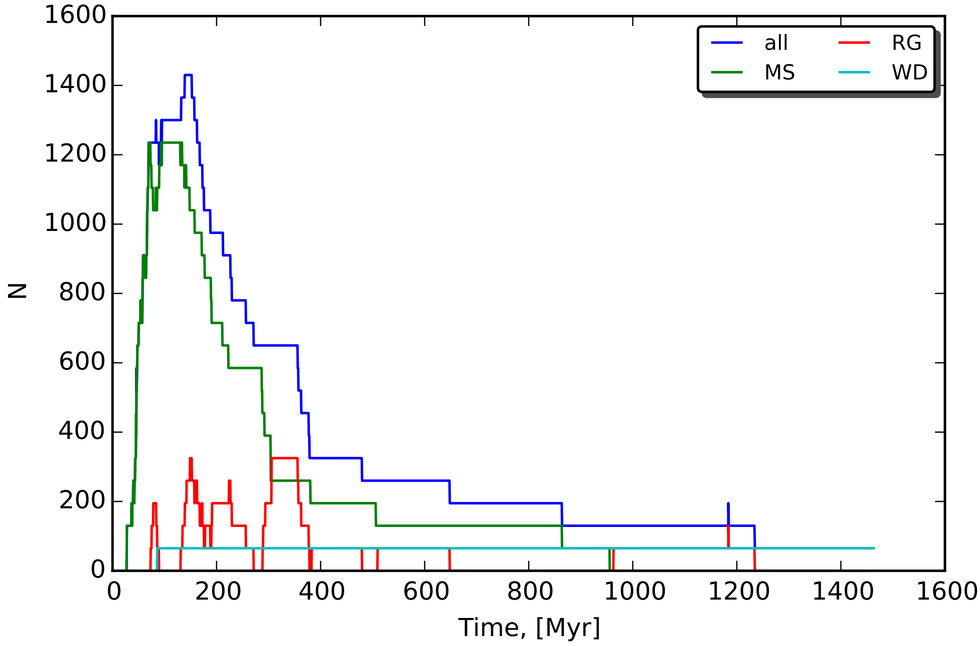

FIGURE 5.14: Number of NS binaries as a function of time. Blue line: all NS binaries, green: NS - MS star, red: NS - RG and cyan: NS - WD.

single stars. The increasing number of WD binaries could imply a high supernovae Ia rate. Once the rotation and non-sphericity of the NSC is taken into account, the amount of TDEs/EMRIs could increase, and the evolution of the system may differ. These effects are to be studied in follow-up papers.

The absence of NSs in the NSC after 200 Myr of evolution is due to high velocity kicks (the velocity distribution of such kicks is still highly debated, see e.g. Beniamini, Hotokezaka, and Piran 2016) at the moment of formation of a NS. This lets them escape from the system. In case of a binary, if the latter survives the supernova explosion, the binary gets a very wide orbit and eventually is destroyed by interaction with single stars in the dense stellar environment. Thus, postulating that all NSs have velocity kicks with 1D dispersion of 265 $\mathrm{km\,s^{-1}}$, makes the formation of a close binary with a NS unlikely. Therefore, the standard scenario for formation of MSPs fails due to a lack of NSs. In this sense our results are consistent with the more simplistic approach by Bortolas, Mapelli, and Spera, 2017 where the authors claim that most of the NSs progenitor binaries do not survive the supernova explosion. But in reality MSPs are observed even in globular clusters (e.g. Manchester et al., 1991) where the escape velocity is much smaller than for a NSC. It means that MSP can form in an alternative scenario, for example from the accretion induced collapse of a WD e.g. Hurley et al., 2010; Taani et al., 2012; Tauris et al., 2013; Freire and Tauris, 2014. If a MSP is detected in the close vicinity of a SMBH it can be used to test general relativity in the strong regime e.g. Psaltis, Wex, and Kramer, 2016. Moreover, the spatial distribution of MSPs in the NSC can give hints on the formation scenario of the NSC (Arca-Sedda, Kocsis, and Brandt, 2017; Abbate et al., 2018). We note that the estimation of number of MSPs in the GC is still to be analysed in more detail. We aim to start several new runs taking into account the MW bulge as an external potential and investigate how many NSs would be bound to the NSC. We expect that the bulge will prevent NSs from escaping and lead to an increase in number of progenitors of MSPs.

A 3-body interactions involving a binary star and the SMBH can result in the binary break up, with one component being captured by the SMBH and the other ejected away with velocities up to 1000 $\mathrm{km\,s^{-1}}$ (Hills, 1988). This mechanism is one of the possible scenarios that can explain the observed population of hypervelocity stars (Brown, 2015). Indeed, if a binary with mass 1 $\mathrm{M_\odot}$ and semi-major axis of 0.1 AU approaches to the MW SMBH as close as its disruption radius $r_{\rm bt} \simeq 10^{-6}$ pc, then it may lead to the formation of a hypervelocity star with $v \simeq 1370\,\mathrm{km\,s^{-1}}$ (Eq. 2 in Brown 2015). As we have seen from Fig. 5.10, the NSC is completely dominated by binaries with small separations at 5 Gyr, meaning that it is likely to expect hypervelocity stars with velocities above 1000 $\mathrm{km\,s^{-1}}$. Our results suggest the majority of the ejected objects are low-mass MS stars or, more rarely, WDs. Since the accretion radius in our simulation exceeds $r_{\rm bt}$ for most of the remained binaries, we leave the detailed analysis of the 3-body interactions that potentially involve them and the SMBH to a forthcoming work.

In this simulation we constructed the initial conditions assuming the in-situ formation of the NSC, but its formation is likely due to star cluster inspiral, at least in part, as firstly suggested by Tremaine, 1976 and Capuzzo-Dolcetta, 1993, although a fraction is likely due to in-situ star formation (King, 2003; King, 2005). Antonini et al. (2012) provided the first self-consistent simulation tailored to reproduce the MW observational properties. Later on, Arca-Sedda et al. (2015) showed that the formation of a NSC around an SMBH weighing a few $10^6\ M_\odot$ is extremely rapid, lasting 0.1-1 Gyr, thus implying that the contributing clusters still are "dynamically young" when arrive to the GC. Moreover, Arca-Sedda et al. (2015) presented the first simulations to model self consistently a whole galactic nucleus and 11 star clusters using, for the whole system, more than 10^6 particles. More recently, Tsatsi et al. (2017) pointed out that the MW NSC rotation can be reproduced by the “star cluster inspiral" scenario. Taking into account these facts, our follow-up simulations may be started with the initial stellar distribution according to the “star cluster inspiral" scenario with some initial rotation.

We note that the rate of TDEs may be enhanced in the presence of an accretion disc (Just et al., 2012; Kennedy et al., 2016). The same is true for the gravitational waves: the drag force of the accretion disc may bring compact objects close to the SMBH resulting in the enhancement of the EMRI rates detectable by LISA, moreover, the gaseous disc may significantly reduce the SMA of stellar binary BHs boosting their merging time (Bartos et al., 2017; Stone, Metzger, and Haiman, 2017; McKernan et al., 2017). In case of NS or WD binaries this mechanism may lead to an enhanced rate of supernovae Ia explosions and gamma-ray bursts. Stellar binaries may merge in the close vicinity of the SMBH due to “eccentric Kozai-Lidov" mechanism (Antonini and Perets, 2012; Prodan, Antonini, and Perets, 2015; Stephan et al., 2016). The Kozai-Lidov oscillations can be studied via the direct N-body modelling with one-to-one particle resolution or by approximating outer stars as a smooth potential. Panamarev et al. (2018) showed that the interaction of stars with the accretion disc may lead to formation of a nuclear stellar disc in the inner part of the galactic nucleus. Such stellar discs may serve as environment for dynamical formation of compact binaries.

Chapter 6

A million–body simulation of the Galactic centre II: observational features

The results presented in this chapter are to be submitted as a peer-reviewed article entitled "Direct N-body simulation of the Galactic centre, part II." with Panamarev, Taras as the first author, Just, Andreas; Spurzem, Rainer; Arca Sedda, Manuel; Berczik, Peter; Wang, Long as co-authors to the journal Monthly Notices of the Royal Astronomical Society. T. Panamarev performed the simulation, analysed the output data, wrote the text. The co-authors contributed by ideas, comments, support with the code development and supervision.

6.1 Method and initial conditions

We simulate stellar dynamics in Milky Way nuclear star cluster will a million particles using direct N-body method see Sec. 5.1. We reach the highest to-date particle number resolution of 65 real stars per one simulated particle. The spatial resolution is down to $r_{\rm acc} = 4.2 \times 10^{-4}$ pc. We keep track of single and binary stellar evolution. The number of fraction of primordial binaries is set to be 5% of the total particle number. When a binary reaches the inner resolution radius ($r_{\rm acc}$), we record its parameters at this moment and do not follow its dynamics any more. Since the number of particles still does not correcpond to the realistic number of stars in the MW NSC, we use scaling methods (described in Sec. 4.4) to apply for the Galactic centre: we synchronize stellar evolution time to correspond to the relaxation time of the NSC. This time-synchronization does not allow to synchronize periods of binary stars with binary stellar evolution at the same time. Thus, the relative velocities of binary companions are slightly larger than they would have been in reality. This drawback does not strongly influence the results derived in this chapter since we do not follow the detailed physics of binary evolution: we ignore gravitational radiation, magnetic braking and use basic approximation for the common envelope phase evolution. We start the simulation with stellar mass spectrum according to Kroupa, 2001 initial mass function. The primordial binaries are drawn in log-uniform distribution of semimajor axis in range between 0.005 and 50 AU with thermal eccentricity distribution.

6.2 Kinematics of the NSC

We start the MW NSC simulation assuming spherically symmetric and isotropic distribution of stars hosting central massive black hole. The evolution of such a system

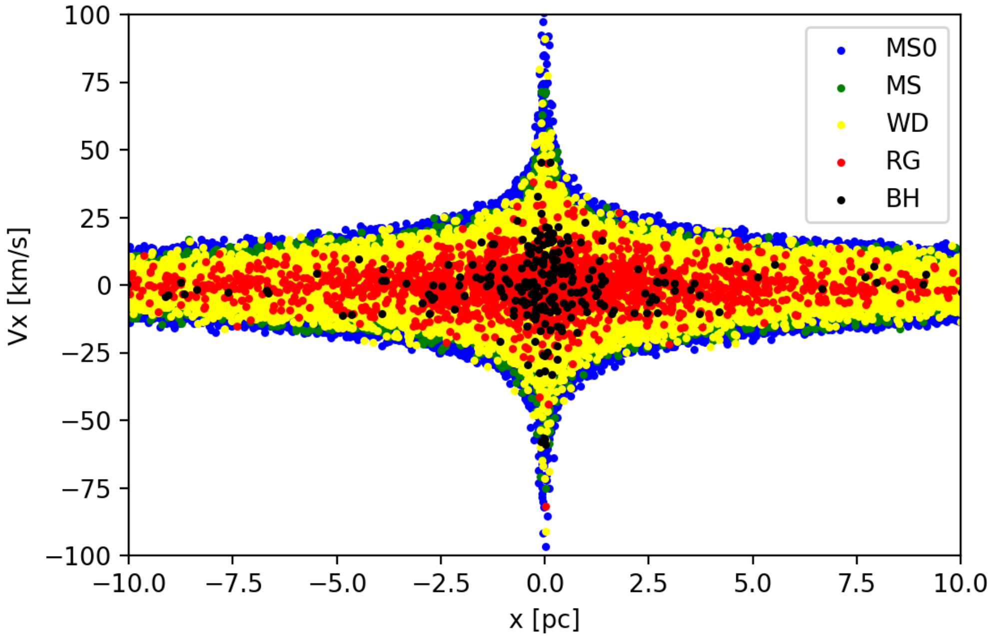

FIGURE 6.1: Position-velocity diagram for various stellar types at $t = 5$ Gyr. Blue colour represents low-mass main sequence stars, green - main sequence, yellow - white dwarfs, red - red giants and black - black holes. The plot shows data only for singe particles.

with equal masses, without stellar evolution and binaries is well understood. We do not expect any deviations of the spherical and isotropic distribution. Although, in more realistic case, taking into account single and binary stellar evolution, accretion of stars onto the SMBH, one may expect that subsystems of stellar objects may behave in different fashion.

Fig. 6.1 shows that overall dynamics (dominated by low-mass main sequence stars) retains isotropy throughout the evolution. The data for different stellar types are plotted on top of each other from low-mass MS stars to BHs in the order according to the legend. The only noticeable feature is the central concentration of stellar BHs, but it is a consequence of the mass segregation as we showed in Sec. 5.2. We observe the same behaviour in the central parsec as well, but now in terms of 3D velocity versus distance to the SMBH (see Fig. 6.2).

Observations of the Galactic centre show that the NSC rotates and is oblate (Feldmeier et al., 2014). Fig. 10 of (Feldmeier et al., 2014) shows anisotropic features. The contradiction of our results with the observations gives another confirmation of the complexity of the system. Anisotropy may arise from axisymmetric potential, initial cluster rotation and several star formation episodes.

Another assumption of our model is the in-situ star formation. Presence of young massive stars in the nearest vicinity of the SMBH (Paumard et al., 2006) points to the ongoing star formation, but it is still debated whether the NSC formation scenario suggests the in-situ formation, migration and merging of globular clusters or combination of both (Antonini, 2013). One of the observational outcomes of the in-situ formation is number and spatial distribution of RRLyrae variable stars. The stars are relatively easy to observe and hence, the comparison with observations may provide a link to the NSC origin. Fig. 6.3 shows histogram of positions of potential RRLyrae

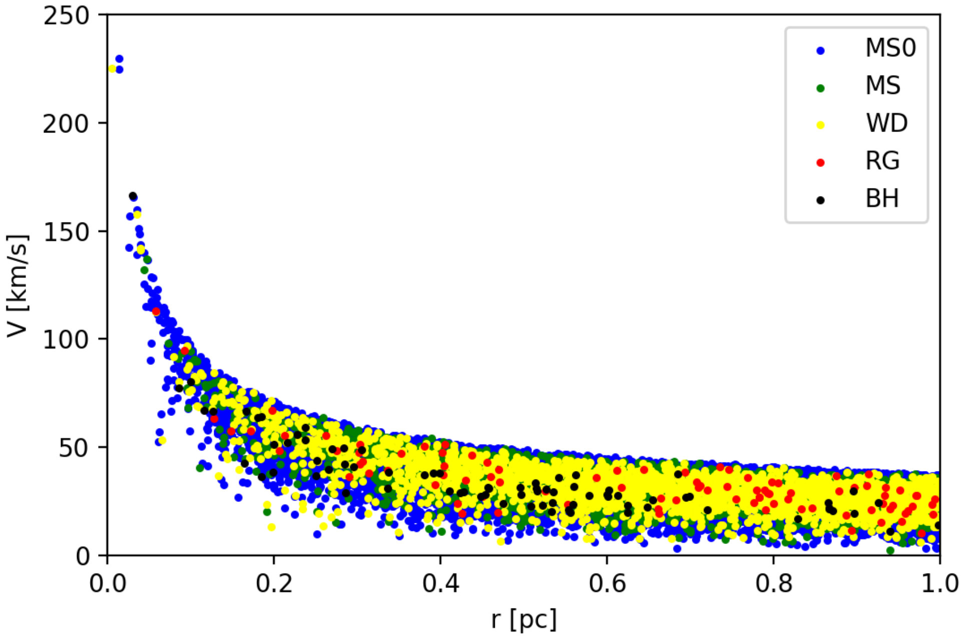

FIGURE 6.2: Radius-velocity diagram for various stellar types at $t = 5$ Gyr inside the central parsec. Colour coding is the same as in Fig. 6.1. The plot shows data only for singe particles.

candidates - stars with main sequence masses of $\sim 0.8 M_{\odot}$. The figure indicates that RRLyrae are concentrated around 8 pc and are shifted in the direction opposite to the SMBH compared with the initial distribution of the possible progenitors. Thus, if a similar pattern is observed in the Galactic centre, it would serve as an indication for the in-situ formation of the NSC.

6.3 Hypervelocity stars

When a binary star approaches a massive black hole, the tidal forces from the hole may disrupt the binary. This process results in ejection of a lighter binary component with high velocity – above the escape speed of the galaxy – and capture of the heavier component on close orbit to the SMBH (Hills, 1988; Brown, 2015).

Our full direct N-body simulation resolves the Galactic centre region down to $\sim 4.0 \times 10^{-4}$ pc. In this section we estimate number and properties of binary encounters with the SMBH that may lead to ejections of hypervelocity stars. We use data for all binaries that crossed the inner radius and extrapolate the results to actual binary disruption radii using the loss-cone theory.

We use the same scaling procedure as we did for the case of tidal disruption events (Sec. 5.3.1). The loss-cone theory suggests number rate of particles falling to specified radius scales with particle number and distance to the SMBH as:

$$N_{\rm acc} \propto r_t^{4/9} \times (N/\ln(0.4N))^{4/9} \tag{6.1}$$

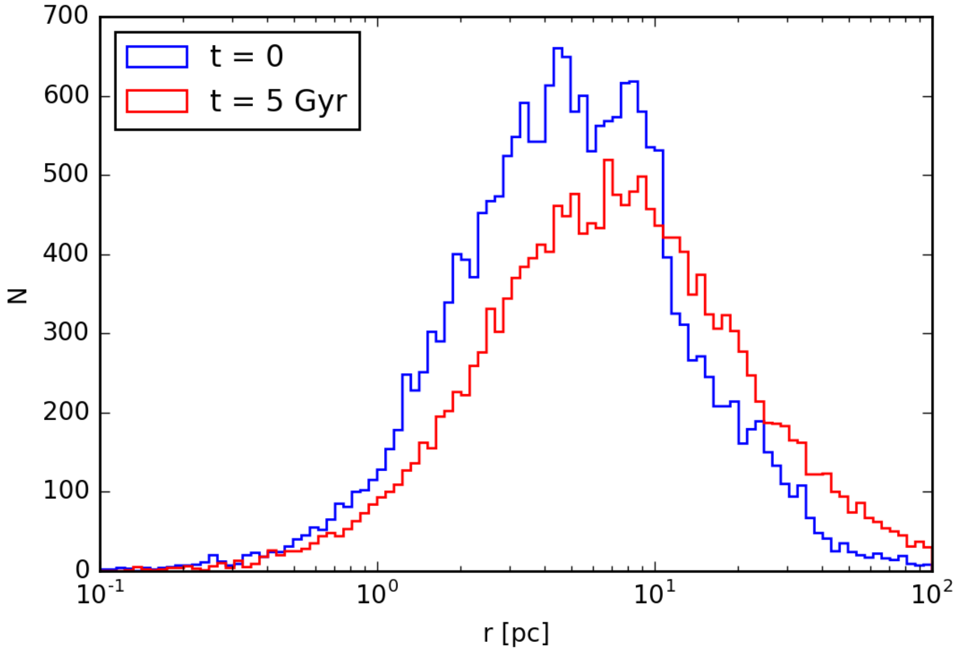

FIGURE 6.3: Number of potential RRLyrae variables (stars with initial masses in range 0.75-0.85 $M_{\odot}$) vs distance from the SMBH in 100 logarithmic bins between 0.1 and 100 pc. Blue and red lines correspond to initial distribution and that at 5 Gyr respectively.

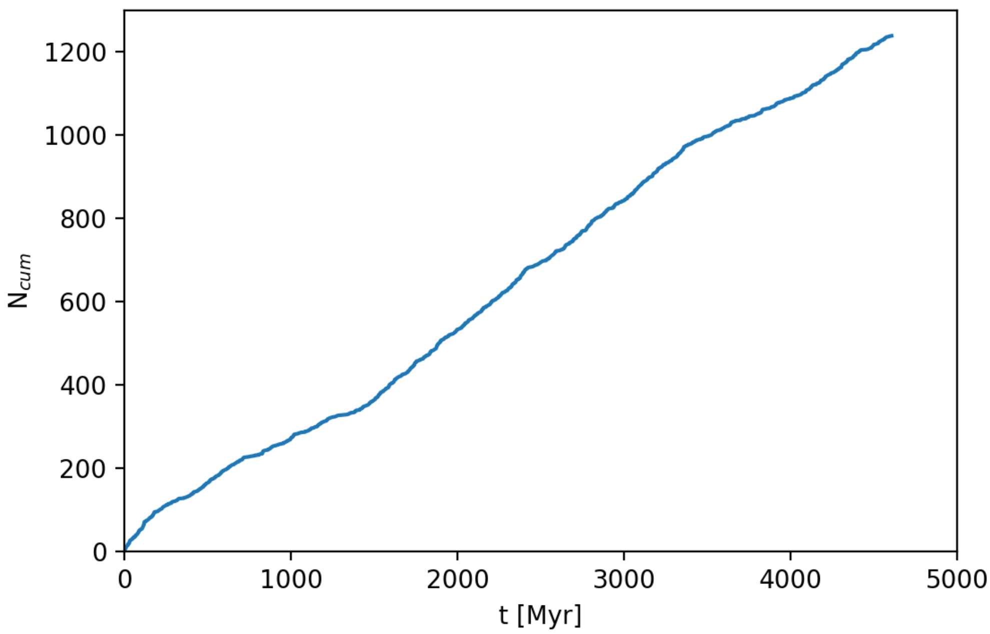

FIGURE 6.4: Number of hypervelocity stars as function of time.

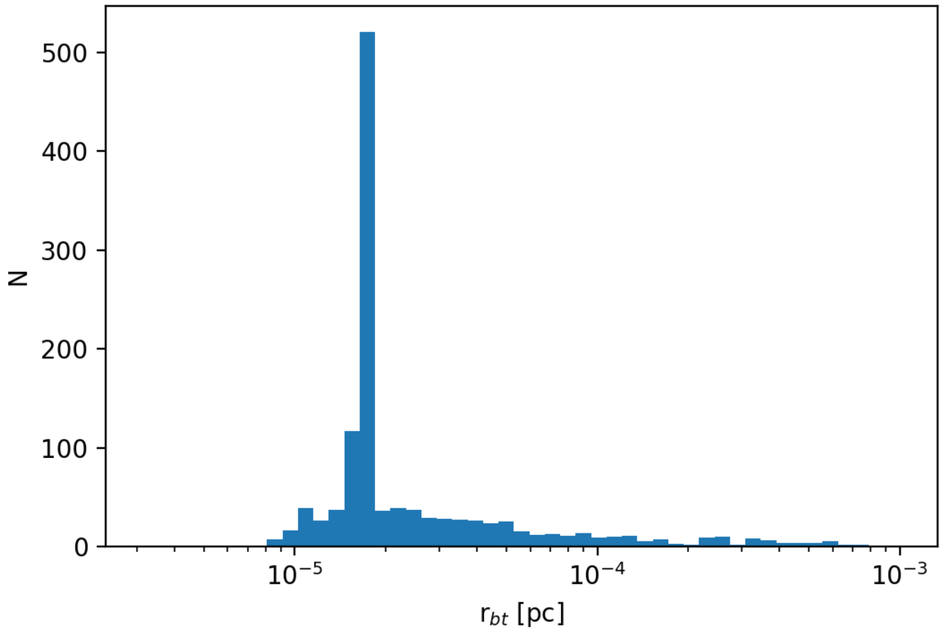

FIGURE 6.5: Distribution of binary disruption radii.

(Baumgardt, Makino, and Ebisuzaki, 2004a; Kennedy et al., 2016). Hence, we can estimate the real number of disrupted binaries as:

$$N_{\text{acc}}^{\text{real}} = \left(\frac{r_{\text{bt}}^{\text{real}}}{r_{\text{acc}}^{\text{sim}}}\right)^{4/9} \times \left(\frac{N_{\text{real}}}{N_{\text{sim}}}\right)^{4/9} \left(\frac{1}{\ln(0.4N_{\text{real}}/N_{\text{sim}})}\right)^{4/9} \times N_{\text{acc}}^{\text{sim}}. \tag{6.2}$$

where $N_{\text{acc}}^{\text{real}}$ is the number of disrupted binaries in the realistic NSC, $< r_{\text{bt}} >$ is the binary disruption radius. N_{real} is the total number of particles in realistic system and N_{sim} is the total number of simulated particles. In the equation above we use the average binary disruption radius that we calculate to be $< r_{\text{br}} >= 4.5 \times 10^{-5} pc$. Given that the total number of disrupted binaries in the simulation by 5 Gyr we measure to be $N\text{sim} = 1359$, then the total number of binaries in the simulation is $N_{\text{acc}}^{\text{real}} = 1741$ giving rate of binary disruption:

$$\dot{N}_{\text{acc}} \simeq 3.48 \times 10^{-7} \text{yr}^{-1} \tag{6.3}$$

Fig. 6.4 shows the cumulative number of disrupted binaries as function of time. The picture indicates that the disruption rate is higher in the beginning especially during first $\simeq$ 200 Myr. This is explained by 2 processes: initial loss-cone depletion and large number of binaries with large separations. During first hundreds of Myr the simulation features high number of HVS ejections with low velocities (due to large separations). For this reason, we restricted out analysis only for the case when the ejection velocity is higher than 500 km s^{-1}.

Fig. 6.5 justifies our choice to use the average value for r_{bt}: most of the particles have similar binary disruption radius.

Thus, the measure of binary disruption rate is quite robust and the uncertainty given by different values of r_{bt} is low. The calculated rate is smaller by 3–4 orders of magnitude than theoretically calculated rate in the case of the full loss-cone

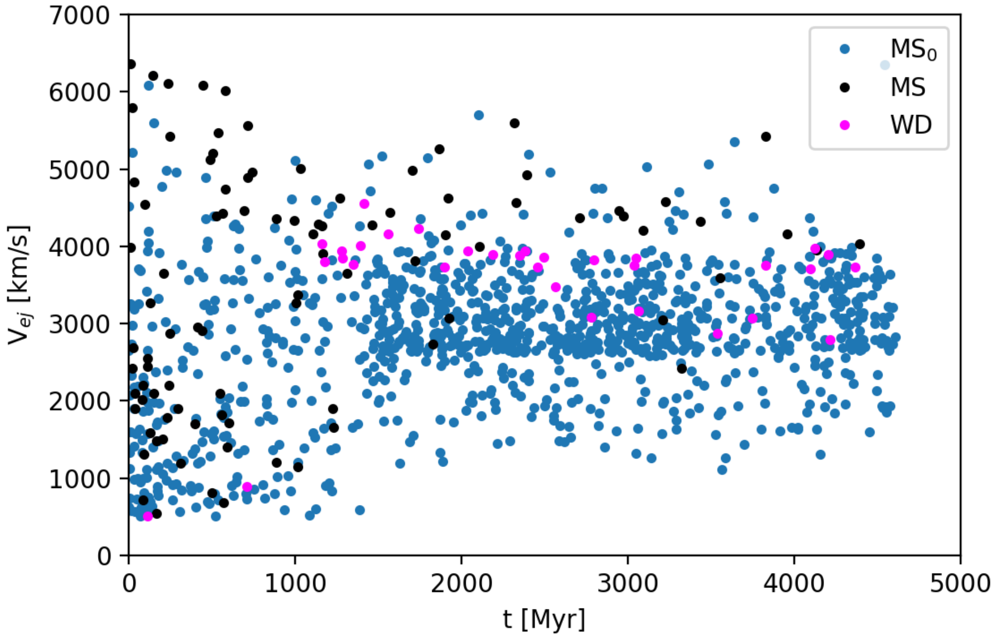

FIGURE 6.6: Ejected velocities of hypervelocity stars as function of time. Colour coding represent stellar types of the ejected particles according to the legend.

(Hills, 1988) and by 1 order of magnitude for the case of the empty loss-cone (Yu and Tremaine, 2003). We explain the discrepancy by the fact that the authors relied on uncertain value of binary fraction with semimajor axis in range $0.01-0.3$ AU. Our simulation shows that most binaries approach the SMBH with semimajor axis close to 0.01 AU. The distribution of disrupted binaries reflects their general distribution as we show in Fig. 5.10. Number of the observed B-type stars in the S-star cluster provides the HVS ejection rate of $2 \times 10^{-7} \mathrm{yr}^{-1}$ (Bromley et al., 2012).

Fig. 6.6 indicates the time–evolution of ejection velocities for the hypervelocity stars. The ejections are dominated by low-mass MS stars. The figure provides evolutionary constrains on the ejection rate and the ejected velocities. Thus, up to $\simeq 1.5$ Gyr the stars are ejected with the range of velocities from 500 to 6400 $\mathrm{km\,s^{-1}}$, but after 1.5 Gyr the mechanism leads to preferential ejection of HVS in the velocity range between 2700 and 4000 $\mathrm{km\,s^{-1}}$ with outliers down to 1500 and up to 5500 $\mathrm{km\,s^{-1}}$. This feature is dictated by the established value for semimajor axis of binaries close to 0.01 AU. The establishment lasts for $\simeq 1.5$ Gyr and is a consequence of dynamical interactions of binaries with single stars in the dense stellar environment. Physical origin of the 'special' value of $a = 0.01$ AU is the minimal separation of binaries given by sizes of stars: $a = 0.01$ AU $\simeq 2R_{\odot}$. Low-mass main sequence stars may overcome this distance, but this process is slow since the encounter cross-section in not large enough to allow for frequent close encounters.

Despite the low-mass MS stars, we also observe ejections of MS stars (with $m > 0.7M_{\odot}$) and white dwarfs. The MS stars are ejected throughout the evolution, but with prevalence during the first 1 Gyr. The remarkable feature of the MS ejections is that their ejected velocities after 1.5 Gyr may reach the values of more than 4000

TABLE 6.1: Types of the ejected stars and their bound companions at $t = 5\,\mathrm{Gyr}$.

Stellar type of the ejected HVS	MS0	MS	WD
Total number / Companion	1090	94	55
MS0	885	0	0
MS	180	85	25
RG	3	6	1
WD	21	3	27
NS	0	0	1
BH	1	0	0

Notes. Total number of ejected stellar types in 5 Gyr and their companions that are captured by the SMBH.

$\mathrm{km\,s^{-1}}$, again, explained by small separation approaching the limiting value dictated by their sizes. The WDs are being ejected after $\simeq$ 1.2 Gyr (for stellar evolutional reasons) with velocities above 3000 $\mathrm{km\,s^{-1}}$. This is explained by the fact that total masses of binaries with WDs are larger than that for low-mass MS stars.

Our model disfavours WD ejections with velocities less than 3000 $\mathrm{km\,s^{-1}}$ that makes their detection unlikely. Given that $1000\,\mathrm{km\,s^{-1}} \approx 1\mathrm{kpc}[Myr^{-1}]$, the ejected WDs are wandering in the intergalactic space.

In Tab. 6.1 we show the total numbers of ejected stars classified by their evolutionary types and their companions that remain bound to the SMBH: $\sim$ 88% of low-mass MS stars, $\sim$ 7.5% and $\sim$ 4.5% of MS and Wds respectively. Lower part of the table shows number of former companions of the ejected star: high mass MS stars are twice larger captured than ejected. Also, in the list of captured stars we see some giants, neutron star and black hole. We do not have enough particle number resolution to study ejection/capture rate for these objects, but their presence itself tells us about the possibility of binary encounter with the SMBH that leads to capture of BH or NS on a tight orbit. The former companions of HVS become bound to the SMBH with semimajor axis of the orbit around the SMBH equal to the binary disruption radius. Thus, Fig. 6.5 gives constrains on orbits of the captured companions. The fact that the captured stars obtain similar semimajor axis (which are relatively small by value) drives promising conditions for contact stellar collisions and mergers, but we need to run more sophisticated simulations to study these processes.

Spectral classification of the ejected stars (see Tab. 6.2) reveals dominance of M-dwarfs followed by K-type stars; F-type stars are ejected twice more frequently than A and G-type stars. The absence of O-type stars is explained by their short lifetimes and sizes. Low number of B stars is due to the selected IMF and particle number resolution. All properties of the ejected/captures stars are highly sensitive to the IMF and initial binary fraction. Numbers obtained from our simulation rely on Kroupa 2001 IMF and initial binary fraction of 5%. But IMF in the Galactic centre appears to be extremely top-heavy (Bartko et al., 2010).

TABLE 6.2: Spectral types of the ejected main sequence stars and their total number in 5 Gyr.

O	B	A	F	G	K	M
0	4	15	27	17	149	972

Notes. The spectral types are derived from the effective temperature provided by the binary stellar evolution package BSE.

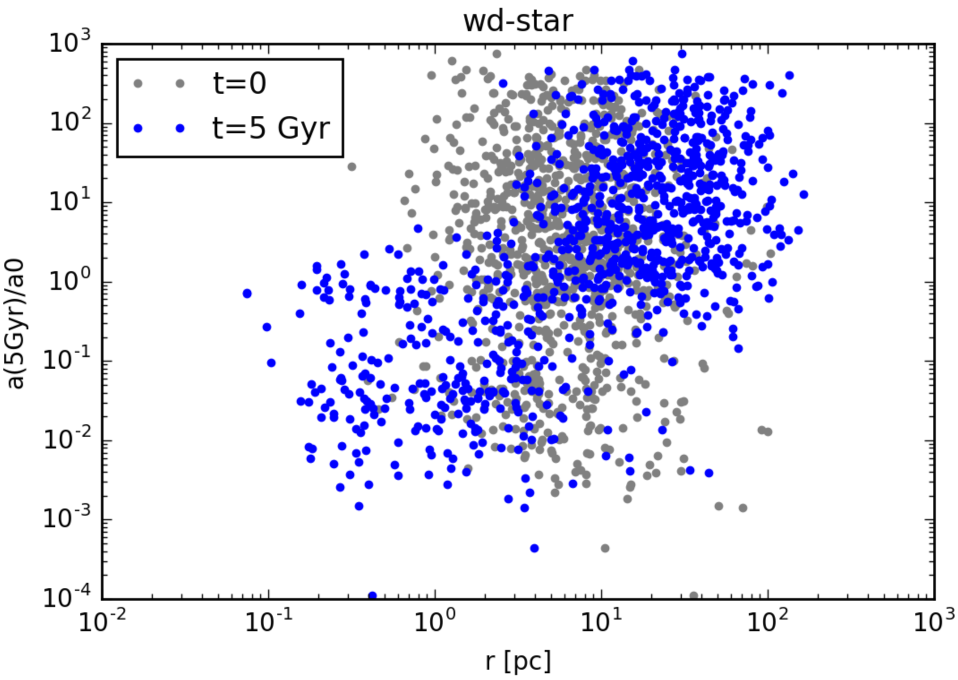

FIGURE 6.7: Semimajor axis ratio at 5 Gyr to the initial for white dwarf – normal star binaries vs centre of mass positions. Grey points show the initial distribution of these binaries.

6.4 Possible nature of the X-ray excess

White dwarf and main sequence star binary systems may be responsible for X-ray emission. The emission originates from mass transfer of a (usually) late-type main sequence star to a white dwarf. These binaries are called cataclysmic variables (CVs) and feature short periods of the order of hours (e.g. Hellier, 2001; Szkody and Gaensicke, 2012). In the simulation we do not follow the details of binary evolution on such timescales, but we can analyse the distribution of the potential CV candidates. By candidates we mean all 'hard' WD-MS binaries.

General outcome of the binary – single star interactions (assuming that binaries are initially 'hard') in a dense stellar environment is hardening of semimajor axis. Fig. 6.7 shows the ratio of semimajor axis of WD-MS binaries at 5 Gyr to the initial SMA as function of distance: binary systems that with reduced SMA segregate to the centre, while binaries with increased SMA tend to move in the direction opposite to the SMBH. These two groups of binary systems are seen on the Fig. 6.7 as two 'clouds' with clear transition radius at 2–3 pc. We connect this transition distance

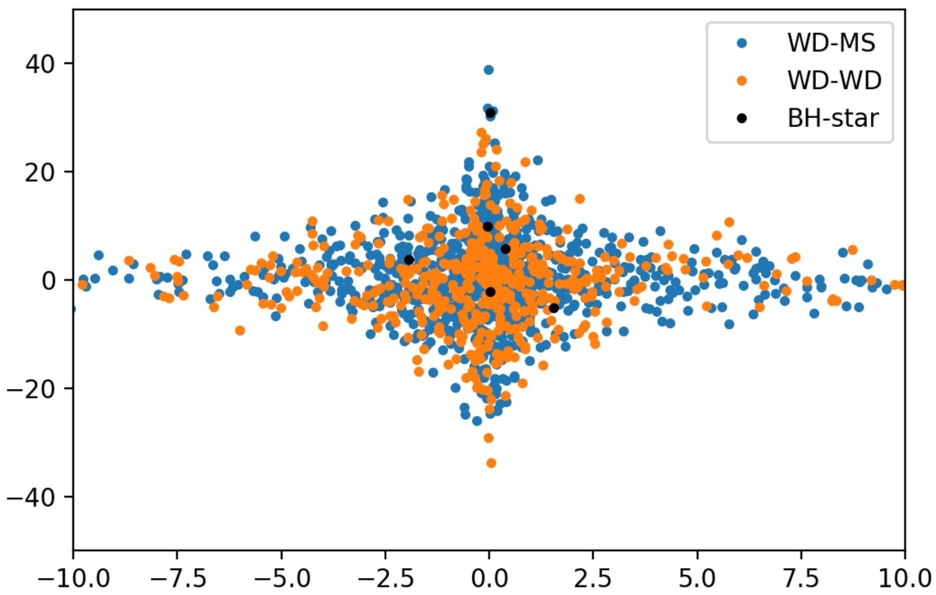

FIGURE 6.8: Position-velocity diagram for WD binaries.

with the influence radius of the SMBH. $r_{\rm inf}$ is inversely proportional to velocity dispersion, while the dispersion drives the boundary between 'hard' and 'soft' binaries is a stellar system (Heggie, 1975).

Fig. 6.8 reflects the position-velocity diagram for WD-MS, WD-WD and BH-star binaries. WD-MS binaries are quite abundant in the central 10 pc region and may be possible sources of the observed X-ray excess. Fig. 6.9 gives hints on possible CV numbers. It shows the relation between Roche-lobe radius of a normal star companion in MS-WD system versus distance to the SMBH. The Roche-lobe radius is given by (Eggleton, 1983) :

$$r_L = \frac{0.49q^{2/3}}{0.6q^{2/3} + \ln(1+q^{1/3})}, \tag{6.4}$$

where q is the mass ratio of the binary system; r_L is given in units of the binary separation. We do not discuss how many of these binaries may become CVs since we do not track all relevant physics in such binary system, but the their presence indicates that in principle the Galactic centre environment favours formation of CVs.

Another source of X-ray excess may come from X-ray binaries. The radiation is produces in similar way as for the case of CVs, but here the donor is a neutron star of a black hole (e.g. Tauris and van den Heuvel, 2006). Our simulation features 6 binaries with black holes (the number is not scaled to realistic NSC), 4 of the companions are MS stars, one WD and one BH. 5 of this systems are long-lived binaries, but one is short-lived wide dynamically formed BH-MS binary. Fig. 6.10 shows evolution and fate of all (long-lived) binaries with black holes. Three of these systems formed dynamically (lines start not from zero). One of primordial binaries (BH-MS0, upper curve on the lower panel) born 'soft', experienced a number of encounters and has been ionized in about 2.5 Gyr. Other examples include: initially relatively wide BH-MS binary was born at distance of ~ 30 pc, experienced a number of encounters that lead to dynamical hardening; initially hard BH-BH binary quickly reduced the

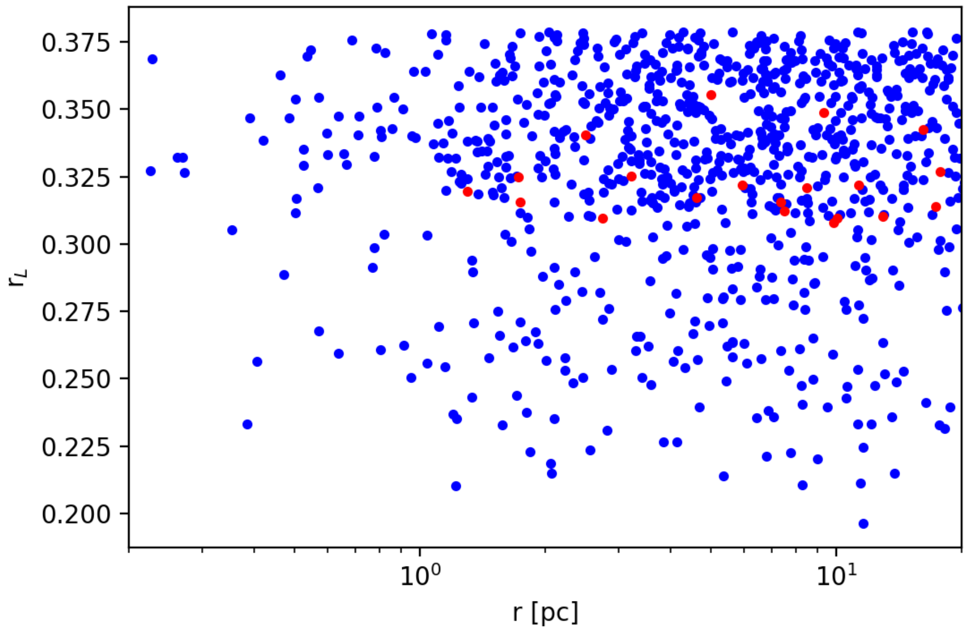

FIGURE 6.9: Roche lobe radius for WD-MS (in blue) and WD-RG (in red) binaries versus distance to the SMBH.

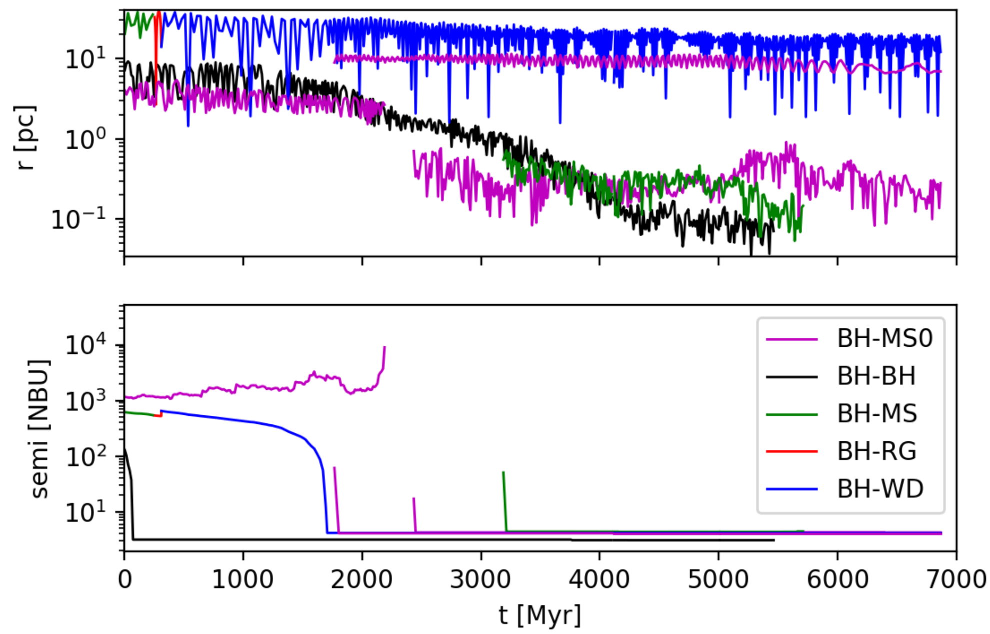

FIGURE 6.10: Upper panel. Evolution of distance to the SMBH for stellar black hole binaries. Lower panel. Evolution of semimajor axis of these binaries. Colour coding shows the black hole's companions according to the legend.

TABLE 6.3: Number of binary companions at $t = 5\,\text{Gyr}$ (NOT scaled to realistic values).

	Main sequence	Red giant	White dwarf	Neutron star	Black hole
Main sequence	23553	58	1033	0	4
Red giant	58	1	24	0	0
White dwarf	1033	24	488	0	1
Neutron star	0	0	0	0	0
Black hole	4	0	1	0	1

semimajor axis and segregated to inner 0.1 pc. At the end our simulation features 2 dynamically formed BH-MS binaries and one primordial BH-BH binary in the central parsec, one primordial BH-WD binary and one dynamically formed BH-MS0 at distance $r \sim 10$ pc. All the remaining BH binaries have the SMA values close to 0.01 AU. Thus, our simulation favours 'hard' black hole binaries, which may provide a plausible explanation for the X-ray excess origin.

Tab. 6.3 provides more detailed picture of binary stars in the Galactic centre by showing numbers of companions. In total, double MS pairs dominate the overall binary population ($\sim 93\%$), the second place take WD-MS binaries ($\sim 4\%$), on the third place are double WD systems ($\sim 2\%$). The remaining 1% constitute mostly binaries with red giants. Small fraction of binaries with black holes does not tell that they are very rare, it means that they may exist in principle, but, first of all we need to have enough particles to study them in more detail and second of all their final number is very sensitive to the IMF.

6.5 Summary

We analysed data from a realistic million-body simulation of the Galactic centre and showed that:

- initially isotropic and spherically symmetric stellar distribution of the NSC retains the anisotropy.

- concentration of RRLyrae variables at 8 pc (if observed) would indicate for the in-situ formation scenario of the NSC.

We analysed dynamics of binaries that encounter the SMBH leading to ejection of HVS. We obtained the HVS rate to be $\sim 2 \times 10^{-7}$ yr. For the first time, we described properties of the ejected stars including their spectral types.

We showed that the MW NSC provides a good environment for the formation of cataclysmic variables and X-ray binaries which may be responsible for the observed Galactic centre X-ray excess.

Part IV

CONCLUSION

Chapter 7

Summary and future directions

7.1 Summary

We presented the analysis of stellar dynamics in close vicinity of a supermassive black hole (few influence radii) by means of direct N-body simulations. In the first part (Ch. 5 and Ch. 6), we focused on the dynamics and evolution of a NSC of the Milky Way galaxy performing high resolution direct million-body simulation. We verified for the first time in a fully astrophysical simulation (with binaries, stellar evolution, compact remnants) that the density distribution of stellar mass black holes after 5 Gyr is fully consistent with the expected Bahcall-Wolf power law slope of -1.75. We obtained the rate of tidal disruption events to be 4 per million year and the number of objects emitting gravitational waves during the accretion onto the SMBH to be 230 per Gyr with 100 of them being possible extreme mass ratio inspirals. We computed the ejection rate of hypervelocity stars produced by Hills mechanism (Hills, 1988) to be 3.5×10^{-7} yr. The examined binary fraction dropped by less then a half from the initial value of 5% with the final value of 3% with 2.5% inside the inner parsec. We discussed the contribution of binaries with compact objects in presence of pulsars and Supernovae Ia rates. We showed that cataclysmic variables and X-ray binaries are likely candidates to explain the observed X-ray excess in the Galactic centre. One paper describing the results is published in the Monthly Notices of the Royal Astronomical Society (Panamarev et al., 2019). Another paper is to be published. The second part of the study (Ch. 4) was to investigate the effect of an accretion disc on stellar dynamics in an AGN. We showed that the interaction of the NSC with the gaseous disc leads to formation of a stellar disc in the central part of the NSC. The accretion of stars from the stellar disc onto the SMBH is balanced by the capture of stars from the NSC into the stellar disc, yielding a stationary density profile. We derived the migration time through the AD to be 3% of the half-mass relaxation time of the NSC. The mass and size of the stellar disc are 0.7% of the mass and 5% of the influence radius of the super-massive black hole. An AD lifetime shorter than the migration time would result in a less massive nuclear stellar disc. The detection of such a stellar disc could point to past activity of the hosting galactic nucleus. The article describing the results is published in the Monthly Notices of the Royal Astronomical Society (Panamarev et al., 2018).

7.2 Future work

High interest to the direct N-body simualtion of the Galactic centre (Bar-Or and Fouvry, 2018; Emami and Loeb, 2019; Yang et al., 2019; Barack et al., 2019) gives motivation to improve our models even further. One of the main simplifications of the Galactic centre simulation was the fixed (same for all stars) accretion radius. Thus, the next step is to implement tidal disruption according to realistic disruption radius for each star depending on its size. This step will also allow for dynamical formation of hypervelocity stars (since the binary disruption radius is large than that for single stars). Another important feature to improve is taking into account for the Galactic potential: neutron stars and some stellar black holes after getting high velocities at the formation time (due to asymmetry of the Supernova explosion) escaped from the system, but the Galactic potential would keep them bound to the centre. It is also important to account for alternative formation scenario of neutron stars and millisecond pulsars to give better quantities of their numbers and spatial distribution. Our more distant goal is to perform one-to-one simulation of the galactic nuclei.

The main limitations of our study of star–disc interactions are: absence of stellar mass spectrum (all stars have the same mass) and treatment of the accretion disc as a static density function that acts as a drag force. Implementation of single and binary stellar evolution would allow to study the effect of the gaseous disc on the rate of binary black hole mergers. There is a number of studies that addressed this issue using semi-analytic or numerical (Monte Carlo simulations) treatment (Yang et al., 2019; McKernan et al., 2017; Bartos et al., 2017; McKernan et al., 2019a; McKernan et al., 2019b). But we need large-scale direct N-body simulations to give the precise estimates. The improving sensitivity of LIGO and VIRGO detectors will result in more GW detections providing better statistics of black hole mergers to compare with simulation results.

Part V

APPENDIX

Appendix A

Towards modelling galactic centres with NBODY6++GPU

A.1 Testing performance and consistency of the code.

First, we test performance of the Nbody6++GPU with the central massive black hole by running test simulations using different GPU and CPU combination to find the most optimal configuration for the million-body run (Fig. A.1). Due to the fact that NBODY6++GPU calculates the total force acting on a star as a sum of regular and irregular components, it is not straightforward to scale the performance of the code. For this reason we start several numerical simulations to study the performance scaling with particle number and parameters of the supercomputer.

The computing cluster provided by Jülich supercomputing centre features 4 GPU devises per one computing node with total number of 75 computing nodes. Since we have a computing quota, we can not use as many nodes as possible. Fig. A.1 suggests the fastest configuration of using 1024K particles with 64 GPUs and 2 GPUs per one MPI process. It means that we need 2000 seconds to simulate the system for 1 N-body unit, thus the full simulation (up to 6000 units = 1 relaxation time) would take $\simeq$ 139 days. In case of using 16 GPUs it would take 250 days. Thus, increasing number of GPUs by a factor of 4, reduces the total computational time by a factor of $\simeq$ 1.8. Therefore, the optimal configuration is 1024K particles on 16 GPUs and 1 MPI process per 2 GPU devices.

Another important task before starting the large-scale simulation is to check the consistency of the code. We do it by comparison with analogous test simulations with Phi-Grape/GPU - the software that was used for studying star-disc interactions (Just et al., 2012; Kennedy et al., 2016). To reduce the timings and usage of the resources, we set the particle number to minimum quantity that is still appropriate. One of the direct comparable measures of the dynamics of the system as a whole is to measure the evolution of half-mass radii. In Fig. A.2 we compare half-mass radii as function of time for identical simulations with Nbody6++GPU and Phi-Grape/GPU and see the consistency.

Another feature implemented in Nbody6++GPU is the stellar accretion onto the SMBH. Since Nbody6++GPU treats close encounters using KS-regularization method (see Sec. 3.5) instead of introducing a softening parameter (like in Phi-Grape/GPU), we expect more accurate determination of orbital parameters of the captured stellar objects by SMBH. Fig. A.3 shows eccentricity distribution for 2 various models of the accretion disc in Phi-Grape (upper panel) and Nbody6++GPU (lower panel). The comparison yields that for the case of Nbody6++GPU the eccentricity distribution of captured particles have larger widths which is explained by more accurate treatment of close two-body encounters.

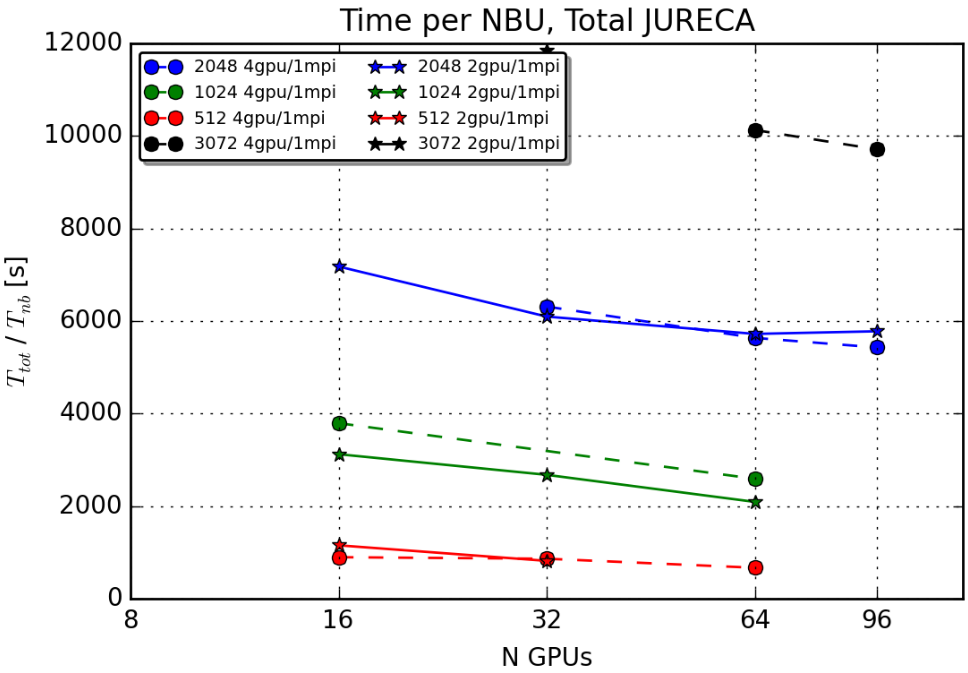

FIGURE A.1: Performance tests for large–N runs. X-axis corresponds to number of graphical processing units (GPUs), Y-axis shows value of real time in seconds needed to perform 1 time-unit in simulating system. Different colours represent particle number from 512K in red up to 3072K in blue. Filled circles denote the case of using 4 GPUs per one MPI process, filled stars show the case of using 2 GPUs per one MPI process.

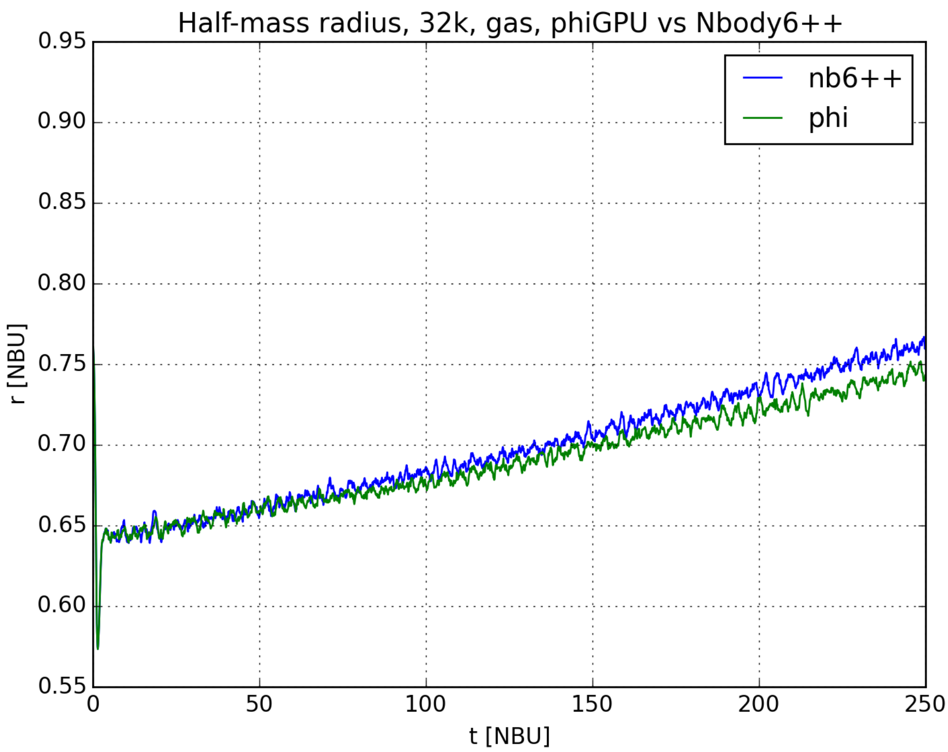

FIGURE A.2: The half-mass radius comparison. Nbody6++GPU and phiGPU.

In conclusion we can claim that Nbody6++GPU shows good performance and is properly extended for the case of galactic nuclei simulations.

(a)

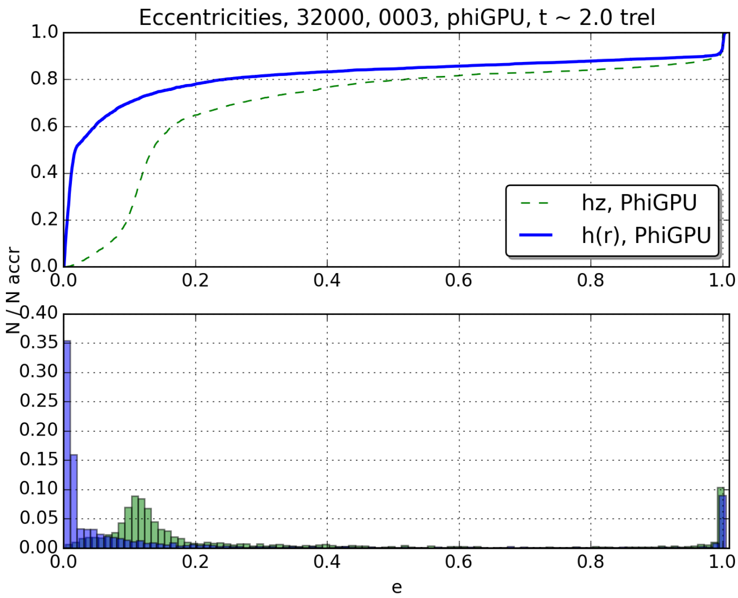

(b)

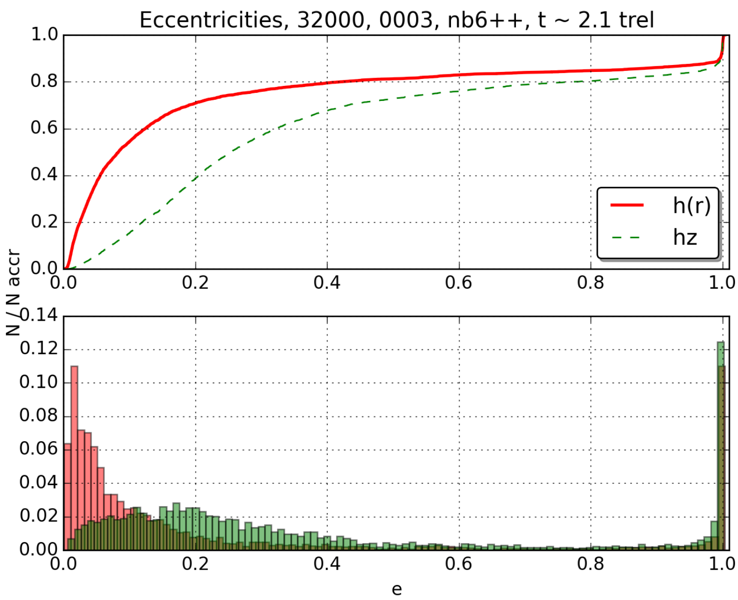

FIGURE A.3: Orbital eccentricities of accreted stars at the moment of accretion.

Bibliography

Aarseth, S. J. (1963). "Dynamical evolution of clusters of galaxies, I". In: *MNRAS* 126, p. 223. DOI: 10.1093/mnras/126.3.223.

— (1985). "Direct methods for N-body simulations." In: *Multiple time scales, p. 377 - 418*. Ed. by J. U. Brackbill and B. I. Cohen, pp. 377–418.

— (Oct. 2003). *Gravitational N-Body Simulations*, p. 430.

Aarseth, Sverre J., Christopher A. Tout, and Rosemary A. Mardling (2008). *The Cambridge N-Body Lectures*. Vol. 760. DOI: 10.1007/978-1-4020-8431-7.

Abbate, F. et al. (Jan. 2018). "Probing the formation history of the nuclear star cluster at the Galactic Centre with millisecond pulsars". In: *MNRAS* 473, pp. 927–936. DOI: 10.1093/mnras/stx2364. arXiv: 1708.01627.

Abbott, B. P. et al. (Feb. 2016). "Observation of Gravitational Waves from a Binary Black Hole Merger". In: *Phys. Rev. Lett* 116.6, 061102, p. 061102. DOI: 10.1103/PhysRevLett.116.061102. arXiv: 1602.03837 [gr-qc].

Abuter, R. et al. (July 2018). "Detection of the gravitational redshift in the orbit of the star S2 near the Galactic centre massive black hole". In: *A&A* 615, L15, p. L15. DOI: 10.1051/0004-6361/201833718.

Ackermann, M. et al. (2017). "The Fermi Galactic Center GeV Excess and Implications for Dark Matter". In: *The Astrophysical Journal* 840.1, 43, p. 43. DOI: 10.3847/1538-4357/aa6cab. arXiv: 1704.03910 [astro-ph.HE].

Ahmad, A. and L. Cohen (1973). "A numerical integration scheme for the N-body gravitational problem." In: *Journal of Computational Physics* 12, pp. 389–402. DOI: 10.1016/0021-9991(73)90160-5.

Alexander, T. (Nov. 2005). "Stellar processes near the massive black hole in the Galactic center [review article]". In: *Physics Reports* 419, pp. 65–142. DOI: 10.1016/j.physrep.2005.08.002. eprint: astro-ph/0508106.

Alexander, T. and C. Hopman (June 2009). "Strong Mass Segregation Around a Massive Black Hole". In: *ApJ* 697, pp. 1861–1869. DOI: 10.1088/0004-637X/697/2/1861. arXiv: 0808.3150.

Alexander, Tal (2017). "Stellar Dynamics and Stellar Phenomena Near A Massive Black Hole". In: *ARA&A*, pp. 1–47. ISSN: 1947-5454. DOI: 10.1146/)). arXiv: 1507.05135. URL: http://arxiv.org/abs/1507.05135.

Alexander, Tal and Clovis Hopman (June 2003). "Orbital In-spiral into a Massive Black Hole in a Galactic Center". In: *ApJ* 590, pp. L29–L32. DOI: 10.1086/376672. arXiv: astro-ph/0305062.

Althaus, L. G. and O. G. Benvenuto (Mar. 1997). "Evolution of Helium White Dwarfs of Low and Intermediate Masses". In: *ApJ* 477, pp. 313–334. DOI: 10.1086/303686.

Amaro-Seoane, P. and X. Chen (Jan. 2014). "The Fragmenting Past of the Disk at the Galactic Center: The Culprit for the Missing Red Giants". In: *ApJL* 781, L18, p. L18. DOI: 10.1088/2041-8205/781/1/L18. arXiv: 1310.0458.

Amaro-Seoane, P. and M. Preto (May 2011). "The impact of realistic models of mass segregation on the event rate of extreme-mass ratio inspirals and cusp re-growth".

In: *Classical and Quantum Gravity* 28.9, 094017, p. 094017. DOI: 10.1088/0264-9381/28/9/094017. arXiv: 1010.5781.

Amaro-Seoane, P. et al. (Sept. 2007). "TOPICAL REVIEW: Intermediate and extreme mass-ratio inspiralsastrophysics, science applications and detection using LISA". In: *CQGr* 24, R113–R169. DOI: 10.1088/0264-9381/24/17/R01. eprint: astro-ph/0703495.

Amaro-Seoane, P. et al. (May 2015). "Research Update on Extreme-Mass-Ratio Inspirals". In: *Journal of Physics Conference Series*. Vol. 610. Journal of Physics Conference Series, p. 012002. DOI: 10.1088/1742-6596/610/1/012002. arXiv: 1410.0958.

Amaro-Seoane, Pau, Carlos F. Sopuerta, and Marc Dewi Freitag (Mar. 2013). "The role of the supermassive black hole spin in the estimation of the EMRI event rate". In: *MNRAS* 429, pp. 3155–3165. DOI: 10.1093/mnras/sts572. arXiv: 1205.4713.

Antonini, F. and D. Merritt (Jan. 2013). "Relativity and the Evolution of the Galactic Center S-star orbits". In: *ApJL* 763, L10, p. L10. DOI: 10.1088/2041-8205/763/1/L10. arXiv: 1211.4594.

Antonini, F. et al. (May 2012). "Dissipationless Formation and Evolution of the Milky Way Nuclear Star Cluster". In: *ApJ* 750, 111, p. 111. DOI: 10.1088/0004-637X/750/2/111. arXiv: 1110.5937.

Antonini, Fabio (2013). "Origin and Growth of Nuclear Star Clusters around Massive Black Holes". In: *ApJ* 763.1, 62, p. 62. DOI: 10.1088/0004-637X/763/1/62. arXiv: 1207.6589 [astro-ph.GA].

Antonini, Fabio and Hagai B. Perets (Sept. 2012). "Secular Evolution of Compact Binaries near Massive Black Holes: Gravitational Wave Sources and Other Exotica". In: *ApJ* 757, 27, p. 27. DOI: 10.1088/0004-637X/757/1/27. arXiv: 1203.2938.

Antonucci, R. (1993). "Unified models for active galactic nuclei and quasars". In: *ARA&A* 31, pp. 473–521. DOI: 10.1146/annurev.aa.31.090193.002353.

Arca-Sedda, M. and R. Capuzzo-Dolcetta (Oct. 2017a). "The MEGaN project - I. Missing formation of massive nuclear clusters and tidal disruption events by star clusters-massive black hole interactions". In: *MNRAS* 471, pp. 478–490. DOI: 10.1093/mnras/stx1586.

Arca-Sedda, M., B. Kocsis, and T. Brandt (Sept. 2017). "Gamma-ray and X-ray emission from the Galactic centre: hints on the nuclear star cluster formation history". In: *ArXiv e-prints*. arXiv: 1709.03119.

Arca-Sedda, M. et al. (June 2015). "Henize 2-10: The Ongoing Formation of a Nuclear Star Cluster around a Massive Black Hole". In: *ApJ* 806, 220, p. 220. DOI: 10.1088/0004-637X/806/2/220. arXiv: 1501.04567.

Arca-Sedda, Manuel and Roberto Capuzzo-Dolcetta (Jan. 2017b). "Lack of nuclear clusters in dwarf spheroidal galaxies: implications for massive black holes formation and the cusp/core problem". In: *MNRAS* 464, pp. 3060–3070. DOI: 10.1093/mnras/stw2483.

Arca-Sedda, Manuel and Alessia Gualandris (July 2018). "Gravitational wave sources from inspiralling globular clusters in the Galactic Centre and similar environments". In: *MNRAS* 477, pp. 4423–4442. DOI: 10.1093/mnras/sty922.

Artymowicz, P., D. N. C. Lin, and E. J. Wampler (June 1993). "Star trapping and metallicity enrichment in quasars and active galactic nuclei". In: *ApJ* 409, pp. 592–603. DOI: 10.1086/172690.

Babak, S. et al. (May 2017). "Science with the space-based interferometer LISA. V. Extreme mass-ratio inspirals". In: *Phys. Rev. D* 95.10, 103012, p. 103012. DOI: 10.1103/PhysRevD.95.103012. arXiv: 1703.09722 [gr-qc].

Bahcall, J. N. and R. A. Wolf (Oct. 1976). "Star distribution around a massive black hole in a globular cluster". In: *ApJ* 209, pp. 214–232. DOI: 10.1086/154711.
Bahcall, J. N. and R. A. Wolf (1977). "The star distribution around a massive black hole in a globular cluster. II Unequal star masses". In: *ApJ* 216, pp. 883–907. ISSN: 0004-637X. DOI: 10.1086/155534. URL: http://adsabs.harvard.edu/abs/1977ApJ...216..883B.
Bar-Or, Ben and Jean-Baptiste Fouvry (2018). "Scalar Resonant Relaxation of Stars around a Massive Black Hole". In: *The Astrophysical Journal* 860.2, L23, p. L23. DOI: 10.3847/2041-8213/aac88e. arXiv: 1802.08890 [astro-ph.GA].
Barack, L. and C. Cutler (Apr. 2004). "LISA capture sources: Approximate waveforms, signal-to-noise ratios, and parameter estimation accuracy". In: *Phys. Rev. D* 69.8, 082005, p. 082005. DOI: 10.1103/PhysRevD.69.082005. eprint: gr-qc/0310125.
Barack, Leor et al. (2019). "Black holes, gravitational waves and fundamental physics: a roadmap". In: *Classical and Quantum Gravity* 36.14, 143001, p. 143001. DOI: 10.1088/1361-6382/ab0587. arXiv: 1806.05195 [gr-qc].
Bartko, H. et al. (Jan. 2010). "An Extremely Top-Heavy Initial Mass Function in the Galactic Center Stellar Disks". In: *ApJ* 708, pp. 834–840. DOI: 10.1088/0004-637X/708/1/834. arXiv: 0908.2177.
Bartos, I. et al. (Feb. 2017). "Rapid and Bright Stellar-mass Binary Black Hole Mergers in Active Galactic Nuclei". In: *ApJ* 835, 165, p. 165. DOI: 10.3847/1538-4357/835/2/165. arXiv: 1602.03831 [astro-ph.HE].
Baruteau, C., J. Cuadra, and D. N. C. Lin (Jan. 2011). "Binaries Migrating in a Gaseous Disk: Where are the Galactic Center Binaries?" In: *ApJ* 726, 28, p. 28. DOI: 10.1088/0004-637X/726/1/28. arXiv: 1011.0360.
Baumgardt, H., P. Amaro-Seoane, and R. Schödel (Jan. 2018). "The distribution of stars around the Milky Way's central black hole. III. Comparison with simulations". In: *A&A* 609, A28, A28. DOI: 10.1051/0004-6361/201730462. arXiv: 1701.03818.
Baumgardt, H., J. Makino, and T. Ebisuzaki (Oct. 2004a). "Massive Black Holes in Star Clusters. I. Equal-Mass Clusters". In: *ApJ* 613, pp. 1133–1142. DOI: 10.1086/423298. eprint: astro-ph/0406227.
— (Oct. 2004b). "Massive Black Holes in Star Clusters. II. Realistic Cluster Models". In: *ApJ* 613, pp. 1143–1156. DOI: 10.1086/423299. eprint: astro-ph/0406231.
Belczynski, K. et al. (July 2018). "The origin of the first neutron star - neutron star merger". In: *A&A* 615, A91, A91. DOI: 10.1051/0004-6361/201732428.
Belczynski, Krzysztof, Vassiliki Kalogera, and Tomasz Bulik (2002). "A Comprehensive Study of Binary Compact Objects as Gravitational Wave Sources: Evolutionary Channels, Rates, and Physical Properties". In: *ApJ* 527.2, pp. 407–431. ISSN: 0004-637X. DOI: 10.1086/340304. arXiv: 0111452 [astro-ph]. URL: http://arxiv.org/abs/astro-ph/0111452.
Bellazzini, Michele et al. (Mar. 2002). "Deep Hubble Space Telescope WFPC2 Photometry of NGC 288. I. Binary Systems and Blue Stragglers". In: *AJ* 123, pp. 1509–1527. DOI: 10.1086/339222. arXiv: astro-ph/0112343.
Bellovary, J. M. et al. (Mar. 2016). "Migration Traps in Disks around Supermassive Black Holes". In: *ApJL* 819, L17, p. L17. DOI: 10.3847/2041-8205/819/2/L17. arXiv: 1511.00005.
Beniamini, Paz, Kenta Hotokezaka, and Tsvi Piran (Sept. 2016). "Natal Kicks and Time Delays in Merging Neutron Star Binaries: Implications for r-process Nucleosynthesis in Ultra-faint Dwarfs and in the Milky Way". In: *ApJ* 829, L13, p. L13. DOI: 10.3847/2041-8205/829/1/L13.

Bentz, M. C. and S. Katz (Jan. 2015). "The AGN Black Hole Mass Database". In: *PASP* 127, p. 67. DOI: 10.1086/679601. arXiv: 1411.2596.

Binney, J. and S. Tremaine (2008a). *Galactic Dynamics: Second Edition*. Princeton University Press.

— (2008b). *Galactic Dynamics: Second Edition*. Princeton University Press.

Bogdanović, Tamara, Roseanne M. Cheng, and Pau Amaro-Seoane (June 2014). "Disruption of a Red Giant Star by a Supermassive Black Hole and the Case of PS1-10jh". In: *ApJ* 788, 99, p. 99. DOI: 10.1088/0004-637X/788/2/99. arXiv: 1307.6176.

Bordoloi, R. et al. (Jan. 2017). "Mapping the Nuclear Outflow of the Milky Way: Studying the Kinematics and Spatial Extent of the Northern Fermi Bubble". In: *ApJ* 834, 191, p. 191. DOI: 10.3847/1538-4357/834/2/191. arXiv: 1612.01578.

Bortolas, E., M. Mapelli, and M. Spera (Aug. 2017). "Supernova kicks and dynamics of compact remnants in the Galactic Centre". In: *MNRAS* 469, pp. 1510–1520. DOI: 10.1093/mnras/stx930. arXiv: 1704.05850.

Brandt, Timothy D. and Bence Kocsis (Oct. 2015). "Disrupted Globular Clusters Can Explain the Galactic Center Gamma-Ray Excess". In: *ApJ* 812. DOI: 10.1088/0004-637X/812/1/15.

Bromley, Benjamin C. et al. (2012). "Binary Disruption by Massive Black Holes: Hypervelocity Stars, S Stars, and Tidal Disruption Events". In: *ApJL* 749.2, L42, p. L42. DOI: 10.1088/2041-8205/749/2/L42. arXiv: 1203.6685 [astro-ph.GA].

Brown, W. R. (Aug. 2015). "Hypervelocity Stars". In: *ARA&A* 53, pp. 15–49. DOI: 10.1146/annurev-astro-082214-122230.

Buchholz, R. M., R. Schödel, and A. Eckart (May 2009). "Composition of the galactic center star cluster. Population analysis from adaptive optics narrow band spectral energy distributions". In: *A&A* 499, pp. 483–501. DOI: 10.1051/0004-6361/200811497. arXiv: 0903.2135.

Capuzzo-Dolcetta, R. (Oct. 1993). "The Evolution of the Globular Cluster System in a Triaxial Galaxy: Can a Galactic Nucleus Form by Globular Cluster Capture?" In: *ApJ* 415, p. 616. DOI: 10.1086/173189. eprint: astro-ph/9301006.

Capuzzo-Dolcetta, R., M. Spera, and D. Punzo (2013). "A fully parallel, high precision, N-body code running on hybrid computing platforms". In: *Journal of Computational Physics* 236, pp. 580–593. DOI: 10.1016/j.jcp.2012.11.013. arXiv: 1207.2367 [astro-ph.IM].

Castelvecchi, Davide (2017). "How to hunt for a black hole with a telescope the size of Earth". In: *Nature* 543, pp. 478–480. DOI: 10.1038/543478a.

Chandrasekhar, S. (1942). *Principles of stellar dynamics*.

Corrales, L. R. et al. (2017). "The Chandra Dust-scattering Halo of Galactic Center Transient Swift J174540.7-290015". In: *The Astrophysical Journal* 839.2, 76, p. 76. DOI: 10.3847/1538-4357/aa68dd. arXiv: 1703.07855 [astro-ph.HE].

Courant, R. and K. O. Friedrichs (1948). *Supersonic flow and shock waves*.

Dauphole, B. and J. Colin (Aug. 1995). "Globular clusters as a new constraint for the potential of our Galaxy." In: *A&A* 300, p. 117.

Daylan, Tansu et al. (June 2016). "The characterization of the gamma-ray signal from the central Milky Way: A case for annihilating dark matter". In: *Physics of the Dark Universe* 12, pp. 1–23. DOI: 10.1016/j.dark.2015.12.005.

Degenaar, N. et al. (2015). "The Swift X-ray monitoring campaign of the center of the Milky Way". In: *Journal of High Energy Astrophysics* 7, pp. 137–147. DOI: 10.1016/j.jheap.2015.03.005. arXiv: 1503.07524 [astro-ph.HE].

Eckart, Andreas et al. (2017). "The Milky Way's Supermassive Black Hole: How good a case is it? A Challenge for Astrophysics & Philosophy of Science". In: DOI:

10.1007/s10701-017-0079-2. arXiv: 1703.09118. URL: http://arxiv.org/abs/1703.09118http://dx.doi.org/10.1007/s10701-017-0079-2.

Eggleton, P. P. (1983). "Aproximations to the radii of Roche lobes." In: *ApJ* 268, pp. 368–369. DOI: 10.1086/160960.

Eisenhauer, F. et al. (Mar. 2011). "GRAVITY: Observing the Universe in Motion". In: *The Messenger* 143, pp. 16–24.

Emami, Razieh and Abraham Loeb (2019). "Segregation of Stellar-Mass Black Holes at the Galactic Center". In: *arXiv e-prints*, arXiv:1903.02578, arXiv:1903.02578. arXiv: 1903.02578 [astro-ph.HE].

Event Horizon Telescope Collaboration et al. (2019a). "First M87 Event Horizon Telescope Results. I. The Shadow of the Supermassive Black Hole". In: *The Astrophysical Journal* 875.1, L1, p. L1. DOI: 10.3847/2041-8213/ab0ec7. arXiv: 1906.11238 [astro-ph.GA].

Event Horizon Telescope Collaboration et al. (2019b). "First M87 Event Horizon Telescope Results. II. Array and Instrumentation". In: *The Astrophysical Journal* 875.1, L2, p. L2. DOI: 10.3847/2041-8213/ab0c96. arXiv: 1906.11239 [astro-ph.IM].

Feldmeier, A. et al. (2014). "Large scale kinematics and dynamical modelling of the Milky Way nuclear star cluster". In: *A&A* 570, A2, A2. DOI: 10.1051/0004-6361/201423777. arXiv: 1406.2849 [astro-ph.GA].

Fermi-LAT Collaboration (Apr. 2017). "Characterizing the population of pulsars in the Galactic bulge with the *Fermi* Large Area Telescope". In: *ArXiv e-prints*. arXiv: 1705.00009 [astro-ph.HE].

Ferrarese, L. et al. (June 2006). "A Fundamental Relation between Compact Stellar Nuclei, Supermassive Black Holes, and Their Host Galaxies". In: *ApJL* 644, pp. L21–L24. DOI: 10.1086/505388. eprint: astro-ph/0603840.

Fragione, G. and A. Loeb (Aug. 2017). "Constraining the Milky Way mass with hypervelocity stars". In: *New Astronomy* 55, pp. 32–38. DOI: 10.1016/j.newast.2017.03.002. arXiv: 1608.01517.

Frank, J. and M. J. Rees (Sept. 1976). "Effects of massive central black holes on dense stellar systems". In: *MNRAS* 176, pp. 633–647.

Freire, P. C. C. and T. M. Tauris (Feb. 2014). "Direct formation of millisecond pulsars from rotationally delayed accretion-induced collapse of massive white dwarfs". In: *MNRAS* 438, pp. L86–L90. DOI: 10.1093/mnrasl/slt164. arXiv: 1311.3478 [astro-ph.SR].

Freitag, M., P. Amaro-Seoane, and V. Kalogera (Sept. 2006). "Stellar Remnants in Galactic Nuclei: Mass Segregation". In: *ApJ* 649, pp. 91–117. DOI: 10.1086/506193. eprint: astro-ph/0603280.

Gallego-Cano, E. et al. (Jan. 2018). "The distribution of stars around the Milky Way's central black hole. I. Deep star counts". In: *A&A* 609, A26, A26. DOI: 10.1051/0004-6361/201730451. arXiv: 1701.03816.

Genzel, R., F. Eisenhauer, and S. Gillessen (Oct. 2010). "The Galactic Center massive black hole and nuclear star cluster". In: *Rev. Mod. Phys.* 82, pp. 3121–3195. DOI: 10.1103/RevModPhys.82.3121. arXiv: 1006.0064.

Ghez, A. M. et al. (Sept. 2000). "The accelerations of stars orbiting the Milky Way's central black hole". In: *Nature* 407, pp. 349–351. DOI: 10.1038/35030032. eprint: astro-ph/0009339.

Ghez, A. M. et al. (Feb. 2005). "Stellar Orbits around the Galactic Center Black Hole". In: *ApJ* 620, pp. 744–757. DOI: 10.1086/427175. eprint: astro-ph/0306130.

Gillessen, S. et al. (Feb. 2009). "Monitoring Stellar Orbits Around the Massive Black Hole in the Galactic Center". In: *ApJ* 692, pp. 1075–1109. DOI: 10.1088/0004-637X/692/2/1075. arXiv: 0810.4674.

Gillessen, S. et al. (Mar. 2017). "An Update on Monitoring Stellar Orbits in the Galactic Center". In: *ApJ* 837, 30, p. 30. DOI: 10.3847/1538-4357/aa5c41. arXiv: 1611.09144.

Gravity Collaboration et al. (2017). "First light for GRAVITY: Phase referencing optical interferometry for the Very Large Telescope Interferometer". In: *Astronomy and Astrophysics* 602, A94, A94. DOI: 10.1051/0004-6361/201730838. arXiv: 1705.02345 [astro-ph.IM].

Gravity Collaboration et al. (2019). "A geometric distance measurement to the Galactic center black hole with 0.3% uncertainty". In: *Astronomy and Astrophysics* 625, L10, p. L10. DOI: 10.1051/0004-6361/201935656.

Greenhill, L. J. et al. (1995). "Detection of a Subparsec Diameter Disk in the Nucleus of NGC 4258". In: *ApJ* 440, p. 619. DOI: 10.1086/175301.

Gültekin, K. et al. (June 2009). "The M-σ and M-L Relations in Galactic Bulges, and Determinations of Their Intrinsic Scatter". In: *ApJ* 698, pp. 198–221. DOI: 10.1088/0004-637X/698/1/198. arXiv: 0903.4897 [astro-ph.GA].

Haggard, D. et al. (Nov. 2010). "The Field X-ray AGN Fraction to z = 0.7 from the Chandra Multiwavelength Project and the Sloan Digital Sky Survey". In: *ApJ* 723, pp. 1447–1468. DOI: 10.1088/0004-637X/723/2/1447. arXiv: 1004.1638 [astro-ph.HE].

Hailey, Charles J. et al. (Apr. 2018). "A density cusp of quiescent X-ray binaries in the central parsec of the Galaxy". In: *Nature* 556, pp. 70–73. DOI: 10.1038/nature25029.

Harfst, S. et al. (July 2007). "Performance analysis of direct N-body algorithms on special-purpose supercomputers". In: *New Astronomy* 12, pp. 357–377. DOI: 10.1016/j.newast.2006.11.003. eprint: astro-ph/0608125.

Hayasaki, Kimitake et al. (2018). "Classification of Tidal Disruption Events Based on Stellar Orbital Properties". In: *ApJ* 855.2, 129, p. 129. DOI: 10.3847/1538-4357/aab0a5. arXiv: 1802.06798 [astro-ph.HE].

Heggie, D. C. (Dec. 1975). "Binary evolution in stellar dynamics." In: *MNRAS* 173, pp. 729–787. DOI: 10.1093/mnras/173.3.729.

Hellier, Coel (2001). *Cataclysmic Variable Stars*.

Hills, J. G. (Mar. 1975). "Possible power source of Seyfert galaxies and QSOs". In: *Nature* 254, pp. 295–298. DOI: 10.1038/254295a0.

— (Feb. 1988). "Hyper-velocity and tidal stars from binaries disrupted by a massive Galactic black hole". In: *Nature* 331, pp. 687–689. DOI: 10.1038/331687a0.

Hobbs, G. et al. (July 2005). "A statistical study of 233 pulsar proper motions". In: *MNRAS* 360, pp. 974–992. DOI: 10.1111/j.1365-2966.2005.09087.x. eprint: astro-ph/0504584.

Hopman, C. (Aug. 2009). "Binary Dynamics Near a Massive Black Hole". In: *ApJ* 700, pp. 1933–1951. DOI: 10.1088/0004-637X/700/2/1933. arXiv: 0906.0374 [astro-ph.CO].

Hopman, C. and T. Alexander (July 2006). "Resonant Relaxation near a Massive Black Hole: The Stellar Distribution and Gravitational Wave Sources". In: *ApJ* 645, pp. 1152–1163. DOI: 10.1086/504400. eprint: astro-ph/0601161.

Humphreys, E. M. L. et al. (2013). "Toward a New Geometric Distance to the Active Galaxy NGC 4258. III. Final Results and the Hubble Constant". In: *ApJ* 775, 13, p. 13. DOI: 10.1088/0004-637X/775/1/13. arXiv: 1307.6031 [astro-ph.CO].

Hurley, J. R. et al. (Mar. 2010). "Formation of binary millisecond pulsars by accretion-induced collapse of white dwarfs". In: *MNRAS* 402, pp. 1437–1448. DOI: 10.1111/j.1365-2966.2009.15988.x.

Hurley, Jarrod R., Onno R. Pols, and Christopher a. Tout (2000). “Comprehensive analytic formulae for stellar evolution as a function of mass and metallicity”. In: *MNRAS* 315.3, pp. 543–569. ISSN: 0035-8711. DOI: 10.1046/j.1365-8711.2000.03426.x. arXiv: 0001295 [astro-ph]. URL: http://arxiv.org/abs/astro-ph/0001295.

— (2002). “Evolution of binary stars and the effect of tides on binary populations”. In: *MNRAS* 329.4, pp. 897–928. DOI: 10.1007/s13398-014-0173-7.2.

Ivanova, N. et al. (Apr. 2005). “The evolution of binary fractions in globular clusters”. In: *MNRAS* 358, pp. 572–584. DOI: 10.1111/j.1365-2966.2005.08804.x. arXiv: astro-ph/0501131.

Just, A. et al. (Oct. 2012). “Enhanced Accretion Rates of Stars on Supermassive Black Holes by Star-Disk Interactions in Galactic Nuclei”. In: *ApJ* 758, 51, p. 51. DOI: 10.1088/0004-637X/758/1/51. arXiv: 1208.4954 [astro-ph.CO].

Kennedy, G. F. et al. (July 2016). “Star-disc interaction in galactic nuclei: orbits and rates of accreted stars”. In: *MNRAS* 460, pp. 240–255. DOI: 10.1093/mnras/stw908. arXiv: 1604.05309.

Khalisi, E., L. Wang, and R Spurzem (2014). *NBODY6++. Manual for the Computer Code*. Astronomisches Rechen-Institut, Heidelberg, Germany.

Kieffer, T. F. and T. Bogdanović (June 2016). “Can Star-Disk Collisions Explain the Missing Red Giants Problem in the Galactic Center?” In: *ApJ* 823, 155, p. 155. DOI: 10.3847/0004-637X/823/2/155. arXiv: 1602.03527.

King, A. (Oct. 2003). “Black Holes, Galaxy Formation, and the M_{BH}-σ Relation”. In: *ApJL* 596, pp. L27–L29. DOI: 10.1086/379143. eprint: astro-ph/0308342.

— (Dec. 2005). “The AGN-Starburst Connection, Galactic Superwinds, and M_{BH}-σ”. In: *ApJL* 635, pp. L121–L123. DOI: 10.1086/499430. eprint: astro-ph/0511034.

Komossa, S. (Sept. 2015). “Tidal disruption of stars by supermassive black holes: Status of observations”. In: *Journal of High Energy Astrophysics* 7, pp. 148–157. DOI: 10.1016/j.jheap.2015.04.006. arXiv: 1505.01093 [astro-ph.HE].

Kormendy, J. and R. Bender (Feb. 2009). “Correlations between Supermassive Black Holes, Velocity Dispersions, and Mass Deficits in Elliptical Galaxies with Cores”. In: *ApJL* 691, pp. L142–L146. DOI: 10.1088/0004-637X/691/2/L142. arXiv: 0901.3778 [astro-ph.GA].

Kormendy, J. and D. Richstone (1995). “Inward Bound—The Search For Supermassive Black Holes In Galactic Nuclei”. In: *ARA&A* 33, p. 581. DOI: 10.1146/annurev.aa.33.090195.003053.

Kouwenhoven, M. B. N. et al. (2007). “The primordial binary population. II.” In: *Astronomy and Astrophysics* 474.1, pp. 77–104. ISSN: 0004-6361. DOI: 10.1051/0004-6361:20077719. URL: http://adsabs.harvard.edu/abs/2007A{\&}A...474...77K.

Kroupa, Pavel (2001). “On the variation of the initial mass function”. In: *Mon Not R Astron Soc* 322.2, pp. 231–246. ISSN: 0035-8711. DOI: 10.1046/j.1365-8711.2001.04022.x. URL: http://adsabs.harvard.edu/abs/2001MNRAS.322..231K.

Kustaanheimo, P. and E. Stiefel (Dec. 1965). In: *für Reine Angewandte Mathematik* 218, p. 204.

Leigh, N. W. C. et al. (June 2014). “Stellar dynamics in gas: the role of gas damping”. In: *MNRAS* 441, pp. 919–932. DOI: 10.1093/mnras/stu622. arXiv: 1404.0379 [astro-ph.SR].

Li, S. et al. (Jan. 2017). “Boosted Tidal Disruption by Massive Black Hole Binaries During Galaxy Mergers from the View of N-Body Simulation”. In: *ApJ* 834, 195, p. 195. DOI: 10.3847/1538-4357/834/2/195. arXiv: 1509.00158.

Luo, J. et al. (Feb. 2016a). "TianQin: a space-borne gravitational wave detector". In: *Classical and Quantum Gravity* 33.3, 035010, p. 035010. DOI: 10.1088/0264-9381/33/3/035010. arXiv: 1512.02076 [astro-ph.IM].

Luo, Jun et al. (2016b). "TianQin: a space-borne gravitational wave detector". In: *Classical and Quantum Gravity* 33.3, 035010, p. 035010. DOI: 10.1088/0264-9381/33/3/035010. arXiv: 1512.02076 [astro-ph.IM].

MacLeod, M., J. Guillochon, and E. Ramirez-Ruiz (Oct. 2012). "The Tidal Disruption of Giant Stars and their Contribution to the Flaring Supermassive Black Hole Population". In: *ApJ* 757, 134, p. 134. DOI: 10.1088/0004-637X/757/2/134. arXiv: 1206.2922 [astro-ph.HE].

Magorrian, J. et al. (June 1998). "The Demography of Massive Dark Objects in Galaxy Centers". In: *AJ* 115, pp. 2285–2305. DOI: 10.1086/300353. eprint: astro-ph/9708072.

Manchester, R. N. et al. (July 1991). "Discovery of ten millisecond pulsars in the globular cluster 47 Tucanae". In: *Nature* 352, pp. 219–221. DOI: 10.1038/352219a0.

Maoz, Dan, Filippo Mannucci, and Gijs Nelemans (Aug. 2014). "Observational Clues to the Progenitors of Type Ia Supernovae". In: *Annual Review of Astronomy and Astrophysics* 52, pp. 107–170. DOI: 10.1146/annurev-astro-082812-141031. arXiv: 1312.0628.

Mapelli, M. and A. Gualandris (2016). "Star Formation and Dynamics in the Galactic Centre". In: *Lecture Notes in Physics, Berlin Springer Verlag*. Ed. by F. Haardt et al. Vol. 905. Lecture Notes in Physics, Berlin Springer Verlag, p. 205. DOI: 10.1007/978-3-319-19416-5_6. arXiv: 1505.05473.

McKernan, B. et al. (Oct. 2011). "On rapid migration and accretion within discs around supermassive black holes". In: *MNRAS* 417, pp. L103–L107. DOI: 10.1111/j.1745-3933.2011.01132.x. arXiv: 1108.1787.

McKernan, B. et al. (Feb. 2017). "On stellar-mass black hole mergers in AGN disks detectable with LIGO". In: *ArXiv e-prints*. arXiv: 1702.07818 [astro-ph.HE].

McKernan, B. et al. (2019a). "Hill sphere contraction at light-speed: Prompt electromagnetic emission from the merger of stellar mass black holes in an AGN accretion disk". In: *arXiv e-prints*, arXiv:1907.03746, arXiv:1907.03746. arXiv: 1907.03746 [astro-ph.HE].

McKernan, B. et al. (2019b). "Monte-Carlo simulations of black hole mergers in AGN disks: Low $\chi_{\rm eff}$ mergers and predictions for LIGO". In: *arXiv e-prints*, arXiv:1907.04356, arXiv:1907.04356. arXiv: 1907.04356 [astro-ph.HE].

McMillan, P. J. and W. Dehnen (June 2007). "Initial conditions for disc galaxies". In: *MNRAS* 378, pp. 541–550. DOI: 10.1111/j.1365-2966.2007.11753.x. eprint: astro-ph/0703534.

Merritt, David (2013). "Loss-cone dynamics". In: *Classical and Quantum Gravity* 30.24, 244005, p. 244005. DOI: 10.1088/0264-9381/30/24/244005. arXiv: 1307.3268 [astro-ph.GA].

Mikkola, S. and S. J. Aarseth (Nov. 1993). "An implementation of N-body chain regularization". In: *Celestial Mechanics and Dynamical Astronomy* 57, pp. 439–459. DOI: 10.1007/BF00695714.

Miller, C. J. et al. (Nov. 2003). "The Environment of Active Galactic Nuclei in the Sloan Digital Sky Survey". In: *ApJ* 597, pp. 142–156. DOI: 10.1086/378383. eprint: astro-ph/0307124.

Miralda-Escudé, J. and J. A. Kollmeier (Jan. 2005). "Star Captures by Quasar Accretion Disks: A Possible Explanation of the M-σ Relation". In: *ApJ* 619, pp. 30–40. DOI: 10.1086/426467.

Miyoshi, Makoto et al. (1995). "Evidence for a black hole from high rotation velocities in a sub-parsec region of NGC4258". In: *Nature* 373, pp. 127–129. DOI: 10.1038/373127a0.

Mori, Kaya et al. (Dec. 2015). "NuSTAR Hard X-Ray Survey of the Galactic Center Region I: Hard X-Ray Morphology and Spectroscopy of the Diffuse Emission". In: *ApJ* 814. DOI: 10.1088/0004-637X/814/2/94.

Muno, M. P. et al. (Nov. 2005a). "A Remarkable Low-Mass X-Ray Binary within 0.1 Parsecs of the Galactic Center". In: *ApJ* 633, pp. 228–239. DOI: 10.1086/444586. eprint: astro-ph/0503572.

Muno, M. P. et al. (Apr. 2005b). "An Overabundance of Transient X-Ray Binaries within 1 Parsec of the Galactic Center". In: *ApJL* 622, pp. L113–L116. DOI: 10.1086/429721. eprint: astro-ph/0412492.

Narayan, Ramesh and Jeffrey E. McClintock (2013). "Observational Evidence for Black Holes". In: *arXiv e-prints*, arXiv:1312.6698, arXiv:1312.6698. arXiv: 1312.6698 [astro-ph.HE].

Nayakshin, S., C. Power, and A. R. King (July 2012). "The Observed M-σ Relations Imply That Super-massive Black Holes Grow by Cold Chaotic Accretion". In: *ApJ* 753, 15, p. 15. DOI: 10.1088/0004-637X/753/1/15. arXiv: 1203.3450.

Netzer, H. (Aug. 2015). "Revisiting the Unified Model of Active Galactic Nuclei". In: *ARA&A* 53, pp. 365–408. DOI: 10.1146/annurev-astro-082214-122302. arXiv: 1505.00811.

Nitadori, K. and S. J. Aarseth (July 2012). "Accelerating NBODY6 with graphics processing units". In: *MNRAS* 424, pp. 545–552. DOI: 10.1111/j.1365-2966.2012.21227.x. arXiv: 1205.1222 [astro-ph.IM].

Nitadori, Keigo and Junichiro Makino (2008). "Sixth- and eighth-order Hermite integrator for N-body simulations". In: *New Astronomy* 13.7, pp. 498–507. DOI: 10.1016/j.newast.2008.01.010. arXiv: 0708.0738 [astro-ph].

Novak, G. S., J. P. Ostriker, and L. Ciotti (Dec. 2012). "Radiative transfer and radiative driving of outflows in active galactic nuclei and starbursts". In: *MNRAS* 427, pp. 2734–2756. DOI: 10.1111/j.1365-2966.2012.21844.x. arXiv: 1203.6062.

Novikov, I. D. and K. S. Thorne (1973). "Astrophysics of black holes." In: *Black Holes (Les Astres Occlus)*. Ed. by C. Dewitt and B. S. Dewitt, pp. 343–450.

Orlov, V. and A. Rubinov (2008). *Zadacha N tel v zvezdnoi dinamike (The N-body problem in stellar dynamics)*. Saint Petersburg State University.

Ostriker, E. C. (Mar. 1999). "Dynamical Friction in a Gaseous Medium". In: *ApJ* 513, pp. 252–258. DOI: 10.1086/306858. eprint: astro-ph/9810324.

Panamarev, Taras et al. (2018). "Star-disc interaction in galactic nuclei: formation of a central stellar disc". In: *MNRAS* 476.3, pp. 4224–4233. DOI: 10.1093/mnras/sty459. arXiv: 1802.03027 [astro-ph.GA].

Panamarev, Taras et al. (2019). "Direct N-body simulation of the Galactic centre". In: *MNRAS* 484.3, pp. 3279–3290. DOI: 10.1093/mnras/stz208. arXiv: 1805.02153 [astro-ph.GA].

Parsons, S. G. et al. (2011). "A Deeply Eclipsing Detached Double Helium White Dwarf Binary". In: *ApJL* 735.2, L30, p. L30. DOI: 10.1088/2041-8205/735/2/L30. arXiv: 1105.3946 [astro-ph.SR].

Paumard, T. et al. (June 2006). "The Two Young Star Disks in the Central Parsec of the Galaxy: Properties, Dynamics, and Formation". In: *ApJ* 643, pp. 1011–1035. DOI: 10.1086/503273. eprint: astro-ph/0601268.

Perets, H. B. et al. (Sept. 2009). "Dynamical Evolution of the Young Stars in the Galactic Center: N-body Simulations of the S-Stars". In: *ApJ* 702, pp. 884–889. DOI: 10.1088/0004-637X/702/2/884. arXiv: 0903.2912 [astro-ph.GA].

Perez, Kerstin et al. (Apr. 2015). "Extended hard-X-ray emission in the inner few parsecs of the Galaxy". In: *Nature* 520, pp. 646–649. DOI: 10.1038/nature14353.

Peters, P. C. (Nov. 1964). "Gravitational Radiation and the Motion of Two Point Masses". In: *Physical Review* 136, pp. 1224–1232. DOI: 10.1103/PhysRev.136.B1224.

Pfuhl, O. et al. (Feb. 2014). "Massive Binaries in the Vicinity of Sgr A*". In: *ApJ* 782, 101, p. 101. DOI: 10.1088/0004-637X/782/2/101. arXiv: 1307.7996.

Phinney, E. S. (1989). "Manifestations of a Massive Black Hole in the Galactic Center". In: *The Center of the Galaxy*. Ed. by M. Morris. Vol. 136. IAU Symposium, p. 543.

Plummer, H. C. (Mar. 1911). "On the problem of distribution in globular star clusters". In: *MNRAS* 71, pp. 460–470.

Preto, M. and P. Amaro-Seoane (Jan. 2010). "On Strong Mass Segregation Around a Massive Black Hole: Implications for Lower-Frequency Gravitational-Wave Astrophysics". In: *ApJL* 708, pp. L42–L46. DOI: 10.1088/2041-8205/708/1/L42. arXiv: 0910.3206.

Prodan, Snezana, Fabio Antonini, and Hagai B. Perets (Feb. 2015). "Secular Evolution of Binaries near Massive Black Holes: Formation of Compact Binaries, Merger/Collision Products and G2-like Objects". In: *ApJ* 799, 118, p. 118. DOI: 10.1088/0004-637X/799/2/118. arXiv: 1405.6029.

Psaltis, Dimitrios, Norbert Wex, and Michael Kramer (2016). "A QUANTITATIVE TEST OF THE NO-HAIR THEOREM WITH Sgr A* USING STARS, PULSARS, AND THE EVENT HORIZON TELESCOPE". In: *ApJ* 818.2, p. 121. ISSN: 1538-4357. DOI: 10.3847/0004-637X/818/2/121. URL: http://stacks.iop.org/0004-637X/818/i=2/a=121?key=crossref.ba6bf1d8ca1be44226a0799e87bb36f7.

Rauch, K. P. (Aug. 1995). "Dynamical evolution of star clusters around a rotating black hole with an accretion disc". In: *MNRAS* 275, pp. 628–640.

— (Apr. 1999). "Collisional Stellar Dynamics around Massive Black Holes in Active Galactic Nuclei". In: *ApJ* 514, pp. 725–745. DOI: 10.1086/306953.

Rees, M. J. (June 1988). "Tidal disruption of stars by black holes of 10 to the 6th-10 to the 8th solar masses in nearby galaxies". In: *Nature* 333, pp. 523–528. DOI: 10.1038/333523a0.

Salpeter, E. E. (Aug. 1964). "Accretion of Interstellar Matter by Massive Objects." In: *ApJ* 140, pp. 796–800. DOI: 10.1086/147973.

Schawinski, K. et al. (Aug. 2015). "Active galactic nuclei flicker: an observational estimate of the duration of black hole growth phases of 10^5 yr". In: *MNRAS* 451, pp. 2517–2523. DOI: 10.1093/mnras/stv1136. arXiv: 1505.06733.

Schirber, M., J. Miralda-Escudé, and P. McDonald (July 2004). "The Transverse Proximity Effect: A Probe to the Environment, Anisotropy, and Megayear Variability of QSOs". In: *ApJ* 610, pp. 105–116. DOI: 10.1086/421451. eprint: astro-ph/0307563.

Schmidt, M. (Mar. 1963). "3C 273 : A Star-Like Object with Large Red-Shift". In: *Nature* 197, p. 1040. DOI: 10.1038/1971040a0.

Schödel, R. et al. (Oct. 2002). "A star in a 15.2-year orbit around the supermassive black hole at the centre of the Milky Way". In: *Nature* 419, pp. 694–696. DOI: 10.1038/nature01121. eprint: astro-ph/0210426.

Schödel, R. et al. (Dec. 2014). "The nuclear cluster of the Milky Way: our primary testbed for the interaction of a dense star cluster with a massive black hole". In: *CQGr* 31.24, 244007, p. 244007. DOI: 10.1088/0264-9381/31/24/244007. arXiv: 1411.4504.

Schödel, R. et al. (Jan. 2018). “The distribution of stars around the Milky Way’s central black hole. II. Diffuse light from sub-giants and dwarfs”. In: *A&A* 609, A27, A27. DOI: 10.1051/0004-6361/201730452. arXiv: 1701.03817.

Segers, M. C. et al. (Oct. 2017). “Metals in the circumgalactic medium are out of ionization equilibrium due to fluctuating active galactic nuclei”. In: *MNRAS* 471, pp. 1026–1044. DOI: 10.1093/mnras/stx1633. arXiv: 1704.05470.

Shakura, N. I. and R. A. Sunyaev (1973). “Black holes in binary systems. Observational appearance.” In: *A&A* 24, pp. 337–355.

Sippel, A. C. and J. R. Hurley (Mar. 2013). “Multiple stellar-mass black holes in globular clusters: theoretical confirmation”. In: *MNRAS* 430, pp. L30–L34. DOI: 10.1093/mnrasl/sls044. arXiv: 1211.6608.

Spitzer, L. (1987). *Dynamical evolution of globular clusters*. Princeton University Press.

Spurzem, R. (Sept. 1999). “Direct N-body Simulations”. In: *Journal of Computational and Applied Mathematics* 109, pp. 407–432. eprint: astro-ph/9906154.

Spurzem, R. et al. (2008). “Parallelization, Special Hardware and Post-Newtonian Dynamics in Direct N - Body Simulations”. In: *The Cambridge N-Body Lectures*. Ed. by S. J. Aarseth, C. A. Tout, and R. A. Mardling. Vol. 760. Lecture Notes in Physics, Berlin Springer Verlag, p. 377. DOI: 10.1007/978-1-4020-8431-7_15.

Stephan, A. P. et al. (Aug. 2016). “Merging binaries in the Galactic Center: the eccentric Kozai-Lidov mechanism with stellar evolution”. In: *MNRAS* 460, pp. 3494–3504. DOI: 10.1093/mnras/stw1220. arXiv: 1603.02709 [astro-ph.SR].

Stone, N. C. and B. D. Metzger (Jan. 2016). “Rates of stellar tidal disruption as probes of the supermassive black hole mass function”. In: *MNRAS* 455, pp. 859–883. DOI: 10.1093/mnras/stv2281. arXiv: 1410.7772 [astro-ph.HE].

Stone, N. C., B. D. Metzger, and Z. Haiman (Jan. 2017). “Assisted inspirals of stellar mass black holes embedded in AGN discs: solving the ‘final au problem’”. In: *MNRAS* 464, pp. 946–954. DOI: 10.1093/mnras/stw2260. arXiv: 1602.04226.

Syphers, D. and J. M. Shull (Mar. 2014). “Hubble Space Telescope/Cosmic Origins Spectrograph Observations of the Quasar Q0302-003: Probing the He II Reionization Epoch and QSO Proximity Effects”. In: *ApJ* 784, 42, p. 42. DOI: 10.1088/0004-637X/784/1/42.

Szkody, P. and B. T. Gaensicke (2012). “Cataclysmic Variables”. In: *Journal of the American Association of Variable Star Observers (JAAVSO)* 40.1, p. 563.

Taani, A. et al. (July 2012). “Investigation of some physical properties of accretion induced collapse in producing millisecond pulsars”. In: *Ap&SS* 340, pp. 147–153. DOI: 10.1007/s10509-012-1023-8. arXiv: 1201.3779 [astro-ph.HE].

Tauris, T. M. and E. P. J. van den Heuvel (2006). “Formation and evolution of compact stellar X-ray sources”. In: *In: Compact stellar X-ray sources. Edited by Walter Lewin & Michiel van der Klis. Cambridge Astrophysics Series, No. 39. Cambridge, UK: Cambridge University Press, ISBN 978-0-521-82659-4, ISBN 0-521-82659-4, DOI: 10.2277/0521826594, 2006, p. 623 - 665*. Vol. 39, pp. 623–665.

Tauris, T. M. et al. (Oct. 2013). “Evolution towards and beyond accretion-induced collapse of massive white dwarfs and formation of millisecond pulsars”. In: *A&A* 558, A39, A39. DOI: 10.1051/0004-6361/201321662. arXiv: 1308.4887 [astro-ph.SR].

Thorne, K. S. (1987). “Gravitational radiation.” In: *Three Hundred Years of Gravitation*. Ed. by S. W. Hawking and W. Israel, pp. 330–458.

Thun, D. et al. (May 2016). “Dynamical friction for supersonic motion in a homogeneous gaseous medium”. In: *A&A* 589, A10, A10. DOI: 10.1051/0004-6361/201527629. arXiv: 1601.07799.

Tremaine, S. D. (Jan. 1976). “The formation of the nuclei of galaxies. II - The local group”. In: *ApJ* 203, pp. 345–351. DOI: 10.1086/154085.

Trenti, M. et al. (Jan. 2007). "Star clusters with primordial binaries - III. Dynamical interaction between binaries and an intermediate-mass black hole". In: *MNRAS* 374, pp. 857–866. DOI: 10.1111/j.1365-2966.2006.11189.x. eprint: astro-ph/0610342.

Tsatsi, A. et al. (Jan. 2017). "On the rotation of nuclear star clusters formed by cluster inspirals". In: *MNRAS* 464, pp. 3720–3727. DOI: 10.1093/mnras/stw2593. arXiv: 1610.01162.

Urry, C. M. and P. Padovani (Sept. 1995). "Unified Schemes for Radio-Loud Active Galactic Nuclei". In: *PASP* 107, p. 803. DOI: 10.1086/133630. eprint: astro-ph/9506063.

Valenti, E. et al. (Mar. 2016). "Stellar density profile and mass of the Milky Way bulge from VVV data". In: *A&A* 587, L6, p. L6. DOI: 10.1051/0004-6361/201527500. arXiv: 1510.07425.

Vasiliev, E. (Oct. 2017). "A New Fokker-Planck Approach for the Relaxation-driven Evolution of Galactic Nuclei". In: *ApJ* 848, 10, p. 10. DOI: 10.3847/1538-4357/aa8cc8. arXiv: 1709.04467.

Vilkoviskij, E. Y. and B. Czerny (June 2002). "The role of the central stellar cluster in active galactic nuclei. I. Semi-analytical model". In: *A&A* 387, pp. 804–817. DOI: 10.1051/0004-6361:20020255. eprint: astro-ph/0203226.

von Hoerner, S. (1960). "Die numerische Integration des n-Körper-Problemes für Sternhaufen. I". In: *Zeitschrift fur Astrophysik* 50, pp. 184–214.

— (1963). "Die numerische Integration des n-Körper-Problems für Sternhaufen, II." In: *Zeitschrift fur Astrophysik* 57, pp. 47–82.

Wang, J. and D. Merritt (Jan. 2004). "Revised Rates of Stellar Disruption in Galactic Nuclei". In: *ApJ* 600, pp. 149–161. DOI: 10.1086/379767. eprint: astro-ph/0305493.

Wang, L. et al. (July 2015). "NBODY6++GPU: ready for the gravitational million-body problem". In: *MNRAS* 450, pp. 4070–4080. DOI: 10.1093/mnras/stv817. arXiv: 1504.03687 [astro-ph.IM].

Wang, L. et al. (May 2016). "The DRAGON simulations: globular cluster evolution with a million stars". In: *MNRAS* 458, pp. 1450–1465. DOI: 10.1093/mnras/stw274. arXiv: 1602.00759 [astro-ph.SR].

Yang, Y. et al. (2019). "AGN Disks Harden the Mass Distribution of Stellar-mass Binary Black Hole Mergers". In: *The Astrophysical Journal* 876.2, 122, p. 122. DOI: 10.3847/1538-4357/ab16e3. arXiv: 1903.01405 [astro-ph.HE].

Yu, Qingjuan and Scott Tremaine (2003). "Ejection of Hypervelocity Stars by the (Binary) Black Hole in the Galactic Center". In: *ApJ* 599.2, pp. 1129–1138. DOI: 10.1086/379546. arXiv: astro-ph/0309084 [astro-ph].

Zel'dovich, Ya. B. (1964). "The Fate of a Star and the Evolution of Gravitational Energy Upon Accretion". In: *Soviet Physics Doklady* 9, p. 195.

Zhong, S., P. Berczik, and R. Spurzem (Sept. 2014). "Super Massive Black Hole in Galactic Nuclei with Tidal Disruption of Stars". In: *ApJ* 792, 137, p. 137. DOI: 10.1088/0004-637X/792/2/137. arXiv: 1407.3537.

— (Sept. 2015). "Supermassive Black Holes in Galactic Nuclei with Tidal Disruption of Stars. II. Axisymmetric Nuclei". In: *ApJ* 811, 22, p. 22. DOI: 10.1088/0004-637X/811/1/22. arXiv: 1508.02838.

Zhu, Zhenlin, Zhiyuan Li, and Mark R. Morris (Apr. 2018). "An Ultradeep Chandra Catalog of X-Ray Point Sources in the Galactic Center Star Cluster". In: *The Astrophysical Journal Supplement Series* 235. DOI: 10.3847/1538-4365/aab14f.